

The 3-D imaging of drill core for fracture mapping

by

Laura Olson

A thesis submitted to the Faculty of Graduate and Postdoctoral
Affairs in partial fulfillment of the requirements for the degree of

Master of Science

in

Earth Sciences

Carleton University

Ottawa, Ontario

© 2013, Laura Olson

Abstract

The Rock Quality Designation (RQD) is a widely used indicator of rock mass strength. This proof of concept research is a step toward the semi-automatic computation of the RQD and is based on 3-D imaging procedures and algorithms to detect fractures in drill core.

The images were acquired with a 3-D laser digitizer. Each image file is a point cloud of spatially referenced measurements in Cartesian space. Variations in the z coordinate were used to detect fractures in profile. Natural fractures were distinguished from mechanical breaks by measuring the angle and quantifying the roughness of the fracture trace. The algorithm measured intact lengths of core for the RQD calculation. Established image processing tools were tested on 3-D data. 3-D core models were made.

This 3-D approach measures changes in the core surface, not highlights and shadows as with 2-D methods. Limitations arise when there is no detectable change in z.

Acknowledgements

I would like to offer my sincerest thanks to my co-supervisors Claire Samson and Steve McKinnon. Thank you both so much for your guidance, feedback and support – especially the opportunity to present my research at American Rock Mechanics Association Symposium in San Francisco. Claire, though you have many graduate students, you always made me feel like I was the only one. I really appreciated the chance to do 3-D imaging research; I learned something completely new and leading-edge. Steve, thank you for your insight on fractures, RQD and the mining industry; I really enjoyed stepping outside my area of expertise and learning about the relationship between geology and engineering.

Thank you to Denis Thibodeau at Vale in Sudbury for sending the cores to Carleton. Having the core samples at-hand, in the lab, was an important factor in the success of the project. I would like to offer a special thank you to fellow graduate student Alex Boivin for helping me with the fundamentals of programming with MATLAB. With those fundamental skills, and after a great deal of struggle, I learned to write short, elegant code and highly automated algorithms.

Table of Contents

Title Page *p. i*

Abstract *p. ii*

Acknowledgements *p. iii*

Table of Contents *p. iv-vii*

List of Tables *p. viii-ix*

List of Illustrations *p. x-xv*

List of Appendices *p. xvi*

1. Introduction *p. 1-4*

2. Background Information *p. 5-31*

2.1 The Rock Quality Designation – Definition *p. 5*

2.2 The Rock Quality Designation – Design and Evolution *p. 5-9*

2.3 The Rock Quality Designation – Best Practices *p. 9-21*

2.4 The Rock Quality Designation – Underground Mining and Core
Logging *p. 21-22*

2.5 Two-Dimensional (2-D) Imaging *p. 22-27*

2.6 Three-Dimensional (3-D) Imaging *p. 27-30*

2.7 Summary of Recommendations for 3-D Imaging *p. 30*

2.8 Summary *p. 31*

3. Methods *p. 32-108*

3.1 Overview *p. 32-33*

3.2 Instrumentation *p. 33-36*

3.3 Digitizer Configuration *p. 37-42*

3.4 Image Acquisition *p. 43-47*

3.5 Image Properties *p. 48-57*

3.6 Image Processing and 3-D Modeling Software *p. 58*

3.7 Discontinuity Detection *p. 59-70*

3.8 Discontinuity Detection - Profile Methods *p. 74-83*

3.9 Fracture Location and the RQD *p. 84-86*

3.10 Distance-Based Images *p. 87-91*

3.11 Fracture Characterization *p. 92-103*

3.12 3-D Core Models *p. 104-108*

4. Evaluation and Results *p. 109-148*

4.1 Overview *p. 109*

4.2 Profile Methods *p. 109-122*

4.3 The RQD *p. 123-126*

4.4 Fracture Characterization *p. 126-135*

4.5 Distance-Based Images *p. 136-138*

4.6 3-D Core Models *p. 139-148*

5. Final Products *p. 149-171*

5.1 Overview *p. 149-150*

5.2 The Flowchart Legend *p. 151-152*

5.3 Single Core Image Acquisition Algorithm *p. 153-156*

5.4 Profile Acquisition Algorithm *p. 157-158*

5.5 Fracture Detection Algorithm *p. 159-161*

5.6 The RQD Algorithm *p. 162-164*

5.7 Distance-Based Image Algorithm *p. 165-166*

5.8 Fracture Trace Algorithm *p. 167-168*

5.9 Fracture Characterization Algorithm *p. 169-171*

6. Discussion, Recommendation for Future Work, Concluding Remarks

p. 172-182

6.1 Overview *p. 172*

6.2 The Digitizer *p. 172-173*

6.3 The 3-D data *p. 173-174*

6.4 Fracture Detection *p. 174-175*

6.5 The RQD *p. 175-176*

6.6 Fracture Characterization *p. 176*

6.7 Distance-Based Images *p. 176-177*

6.8 The 3-D Core Models *p. 177-178*

6.9 Level of Automation *p. 178*

6.10 Recommendations for Future Work *p. 179-181*

6.8 Concluding Remarks *p.182*

7. References *p. 183-191*

8. Appendices *p. 192-203*

List of Tables

2. Background Information

2.1 The RQD and Rock Mass Quality *p. 6*

2.2 The Rock Mass Rating (RMR) and Rock Quality *p. 10*

2.3 Weathering Grades of Rock *p. 15*

2.4 Natural and Mechanical Breakage Surface Characteristics *p.17*

3. Methods

3.1 Digitizer Specifications *p. 36*

3.2 Scan Setting Test Results *p. 46*

3.3 Coordinate Data Example *p. 55*

3.4 Scan Setting Test Results with Point Cloud Concentrations *p. 57*

3.5 Fracture Edge Detection Example *p. 85*

3.6 Matrix of Distance Measurements Example *p. 88*

3.7 Matrix of Distance Measurements Converted to Intensity Example
p. 90

3.8 Matrix of Distance Measurements Converted to Binary Example *p. 96*

4. Evaluation and Results

- 4.1 Profile Method and Threshold Detection Test Results *p. 114*
- 4.2 Profile Method and Threshold Detection Basic Statistics *p. 115*
- 4.3 Revised Detrend Method Detection Test Results and Basic Statistics
p. 119
- 4.4 The RQD Test Results *p. 124*
- 4.5 Fracture Characterization Scoring System *p. 127*
- 4.6 Fracture Trace Geometry Detection Test Results *p. 129*
- 4.7 Linear Trace Fracture Detection Test Results *p. 134*
- 4.8 3-D Core Models: Volume, Mass, Density Comparison *p. 148*

List of Illustrations

1. Introduction

1.1 Digital Photograph of a Core Box *p. 2*

2. Background Information

2.1 The RQD Measurement Technique *p. 11*

2.2 Comparison of Core Measurement Techniques *p.13*

2.3 Comparison of Break Surface Types *p. 18*

3. Methods

3.1 Digitizer Components *p. 34*

3.2 Digitizer Measuring Principle *p. 35*

3.3 Digitizer Configuration with Core Box *p. 38*

3.4 Core Boxes Imaged in Sections *p. 39*

3.5 Digitizer Configuration with Turntable *p. 41*

3.6 Turntable Scan Method *p. 42*

3.7 Polygon Editing Tool Scan Options Menu *p. 44*

3.8 Comparison of 3-D Images with Different Scan Settings *p. 47*

3.9 Point Cloud *p. 49*

- 3.10 Coordinate System *p. 51*
- 3.11 Data Acquisition Concept *p. 52*
- 3.12 Data Acquisition Example *p. 53*
- 3.13 Change in z Coordinate Concept *p. 60*
- 3.14 Change in z Coordinate Example *p. 61*
- 3.15 Open and Tight Fracture Detection *p. 63*
- 3.16 Core of Interest Selection Example *p. 64*
- 3.17 Core of Interest Model: Two Views *p. 66*
- 3.18 Threshold Concept *p. 67*
- 3.19 Threshold Applied to Core *p. 68*
- 3.20 Threshold Applied to Profile *p. 70*
- 3.21 Profile Reference System *p. 71*
- 3.22 Profile Example *p. 73*
- 3.23 Profile and Profile Model Example *p. 75*
- 3.24 Difference between the Profile and Profile Model *p. 76*
- 3.25 Difference between the Profile and Profile Model Squared *p. 78*
- 3.26 Absolute Value of the First Derivative Example *p. 80*

- 3.27 First Derivative Profile *p. 82*
- 3.28 Detrend Profile *p. 83*
- 3.29 Intensity-Based Digital Photograph and Distance Based Image *p. 91*
- 3.30 Breakage Surface and Fracture Trace Geometry *p. 93*
- 3.31 Parallel Profile Example *p. 94*
- 3.32 Fracture Trace Detection Method *p. 97*
- 3.33 Line or Curve Decision Method *p. 98*
- 3.34 Natural and Mechanical Fracture Trace Example *p. 99*
- 3.35 Sine Wave and Fracture Trace Example *p. 101*
- 3.36 Linear Fracture Trace Roughness Method: Best Fit Residuals *p. 102*
- 3.37 Linear Fracture Trace Roughness Method: Rose Diagrams *p. 103*
- 3.38 3-D Core Model Common Feature Identification *p. 105*
- 3.39 3-D Core Model Assembly *p. 106*
- 3.40 3-D Core Model Editing *p. 107*

4. Evaluation and Results

- 4.1 Fractures Observed and Detected: Detrend-Variance *p. 110*
- 4.2 Fractures Detect Minus Observed: Detrend-Variance *p. 112*

- 4.3 Percentage of Fractures Detected: Detrend-Variance *p. 113*
- 4.4 Fractures Observed and Detected: Revised Detrend *p. 120*
- 4.5 Fractures Detect Minus Observed: Revised Detrend *p. 121*
- 4.6 Percentage of Fractures Detected: Revised Detrend *p. 122*
- 4.7 Difference between Observed and Calculated RQD *p. 125*
- 4.8 Smooth Fracture Trace fit to Sine Wave *p. 130*
- 4.9 Rough Fracture Trace fit to Sine Wave *p. 131*
- 4.10 Fracture Trace and Sine Wave *p. 132*
- 4.11 Ambiguous Natural Fracture and Mechanical Break *p. 135*
- 4.12 Comparison 1: Intensity-Based Digital Photograph and Distance-Based Image *p. 137*
- 4.13 Comparison 2: Intensity-Based Digital Photograph and Distance-Based Image *p. 138*
- 4.14 Core 1: Granite *p. 140*
- 4.15 Core 2: Gneiss *p. 141*
- 4.16 Core 3: Gabbro *p. 142*
- 4.17 Core Model 1 *p. 143*

4.18 Core Model 2 *p. 144*

4.29 Core Model 3 *p. 145*

4.20 Rendering Quality Comparison *p. 146*

5. Final Products

5.1 Summary of Image Processing Tasks *p. 150*

5.2 Flowchart Legend *p. 152*

5.3 Single Core Acquisition Algorithm Flowchart *p. 154*

5.4 File Selection GUI and Selection Instructions Message *p. 155*

5.5 Core Selection GUI *p. 156*

5.6 Profile Acquisition Algorithm Flowchart *p. 158*

5.7 Fracture Detection Algorithm Flowchart *p. 160*

5.8 Core Profile with Number of Fractures Message *p. 161*

5.9 The RQD Algorithms Flowchart *p. 163*

5.10 The RQD Percentage and Description Messages *p. 164*

5.11 Distance-Based Image Algorithm Flowchart *p. 166*

5.12 Fracture Trace Algorithm Flowchart *p. 168*

5.13 Fracture Characterization Algorithm Flowchart *p. 170*

5.14 Fracture Trace with Fracture Type Messages *p. 171*

8. List of Appendices

Appendix I: 3-D Core Plot MATLAB Code *p. 191*

Appendix II: Single Core Plot MATLAB code *p. 192*

Appendix III: Core Profile Line MATLAB Code *p. 193*

Appendix IV: Fracture Detector MATLAB Code *p. 194 – 195*

Appendix V: RQD MATLAB Code *p. 196*

Appendix VI: Distance-Based Image MATAB Code *p. 197*

Appendix VII: Fracture Trace MATLAB Code *p. 198*

Appendix VIII: Fracture Characterization MATLAB Code *p. 199 – 201*

1. Introduction

As underground mines reach greater depth, where stresses are high, the stability of excavations becomes a critical component of the design process. The strength of the rock mass is strongly affected by the presence of fractures. The safe and economic design of mines therefore requires accurate and systematic measurement of fractures during every phase of operation – from exploration to planning to production. At each stage, engineers make extensive use of fracture data from drill cores. Shown in Figure 1.1 is an example of a core box with cores.

One of the key parameters used in the strength assessment process is the rock quality designation (RQD) – the percentage of unbroken core fragments longer than 10 cm over the total length of a core run. The RQD is measured at most Canadian mines and is a component of the widely used Rock Mass Rating (RMR) system and the Rock Quality Tunneling Index (Q-system).

Mine professionals face the challenge of distinguishing natural fractures that are the result of geological processes from mechanical breaks in the core caused during drilling. Often this difference is subtle and the origin of the fracture may be ambiguous. They may also have to cope with time constraints – typically logging hundreds of meters of core each week. Given these conditions, the type and quantity of fractures in core is often estimated by quick visual inspection. The extreme challenges posed by deep mining underscore the need for reliable data and conscientious data management; the margin for error is infinitesimal and the potential consequences severe (Hadjigeorgiou 2012).



Figure 1.1: Digital photograph of two rows of core in a core box. The core box is approximately 1.5 m long. The core diameter is 36.5 mm.

An innovative, systematic approach is needed improve current core logging methods. The introduction of three-dimensional (3-D) imaging procedures and software can provide fast and accurate identification of fractures in core, reliably distinguish natural fractures from mechanical breaks, compute the RQD and improve the performance of established image processing tools.

The development of semi-automatic 3-D imaging procedures and algorithms to study rock mass characteristics is an emerging field of study – at the interface of computer vision, mining engineering and geology. This is proof of concept research will answer the question: Can 3-D imaging be used to determine the RQD? The primary objectives of this research are to develop image processing procedures and algorithms to:

- Count and locate fractures in core;
- Measure intact core lengths;
- Distinguish between natural fractures and mechanical breaks;
- Calculate the RQD.

The secondary objectives of this research project are to:

- Compare the performance of established image processing tools on intensity-based digital photographs and distance-based images.
- Create three comprehensive 3-D core models which can be rotated and observed from any viewpoint. Calculate the volume of the given core model, measure the mass of the core sample and determine its density.

The reliability of the algorithms was tested against manual measurements. In addition, the advantages and limitations of the digitizer, 3-D data, fracture detection algorithms and methods, distance-based images and 3-D core models were identified and discussed.

After this introductory chapter is a review of relevant background information about the RQD and its design, evolution, measurement procedure, significance to Canadian mining and its merits and shortcomings. Also included in chapter 2 is an outline of some of the two-dimensional (2-D) and 3-D imaging research conducted over the past few decades – in particular, research focused on imaging geological materials. Chapter 3 explains the operation and configuration of the 3-D laser digitizer, image acquisition and processing, various fracture analysis methods, and the assembly of the 3-D core models. In chapter 4, the reliability of the fracture detection and characterization methods, RQD algorithms, distance-based images and 3-D core models is assessed and quantified (when possible). A summary of the algorithm design – inputs, actions, decision points, outputs, etc. – is presented in chapter 5 as a series of flowcharts. Chapter 6 is a discussion of the results and significant findings of each aspect of the research project. Recommendations for future work are also suggested. After chapter 6 are the references and appendices I to VIII. The appendices contain the final versions of the MATLAB code developed for this research.

2. Background Information

2.1 The Rock Quality Designation – Definition

The Rock Quality Designation (RQD) is the percentage of unbroken core fragments longer than 10 cm over the total length of a core run (Deere et al. 1967):

$$RQD(\%) = \frac{\sum L_{core > 10\ cm}}{L_{total\ core\ run}} \times 100\% \quad (2.1)$$

A low percentage indicates poor rock mass quality and a high percentage indicates good rock mass quality. The relation between RQD and rock mass quality is summarized in Table 2.1.

2.2 The Rock Quality Designation - Design and Evolution

Empirical systems for tunnel design and rock mass characterization have been evolving since the late nineteenth century (e.g. Ritter 1879). By the mid-twentieth century schemes such as “rock load” (Terzaghi 1946) and “stand-up time” (Lauffer 1958) had been proposed. Before the RQD was introduced in 1967, the percentage of core recovery – the sum of the core lengths recovered divided by the core run – was typically used as to assess rock quality (Deere and Deere 1989). This approach worked well until drilling techniques improved and

Table 2.1: The RQD and the associated rock mass quality (Deere et al. 1967).

RQD (%)	Rock mass quality
0 – 25	Very poor
25 – 50	Poor
50 – 75	Fair
75 – 90	Good
90 – 100	Excellent

core recovery routinely became close to 100%. Deere et al. (1967) recognized that a “modified core recovery” could provide a more meaningful indication of the state of the rock mass.

Deere et al. (1967) used an early version of the RQD in 1964 to illustrate the difference between the strength of the rock mass at two potential construction sites. With the support of the US Air Force and US Department of Transportation, research on the RQD continued at the University of Illinois over the following few years. In that time, the RQD was further field tested during the construction of shafts and tunnels (Deere and Deere 1989).

The work of Deere et al. on the RQD was first published in 1967. This publication introduced geologists and engineers to a fast and easy to use site evaluation tool to predict tunneling conditions at the early stages of the design process (Deere and Deere 1989). In 1968, Stagg and Zienkiewicz published a book on rock mechanics which included the RQD. This book presented the RQD to a wider international readership. Today essentially every Canadian mine uses the RQD (Milne et al. 1998).

Its near universal use highlights the importance of the RQD. Moreover, the role of the RQD has expanded and is a key component of the two other commonly applied rock mass classifications used at Canadian mines (Milne et al. 1998) - the Norwegian Geotechnical Institute’s Rock Quality Tunneling Index or

Q system (Barton et al. 1974) and the Rock Mass Rating or RMR (Bieniawski 1973, 1974, 1976, 1979, 1988). For example, the Q equation is defined as:

$$Q = \left(\frac{RQD}{J_n} \right) \left(\frac{J_r}{J_a} \right) \left(\frac{J_w}{SRF} \right) \quad (2.2)$$

Where:

- J_n is the number of joint sets
- J_r is the roughness of the weakest joint
- J_a is the degree of alteration or filling along the weakest joint
- J_w is the degree of water inflow
- SRF is the stress reduction factor

These are numerical parameters which correspond to qualitative descriptions of rock mass conditions and as such do not have units. The quotient RQD/J_n indicates the relative block size, the inter-block shear strength is represented by J_r/J_a and J_w/SRF denotes the active stress (Barton et al. 1974).

The RMR system considers six parameters to classify a rock mass:

- Uniaxial compressive strength of rock material
- RQD
- Spacing of discontinuities
- Condition of discontinuities

- Ground water conditions
- Orientation of discontinuities

The value of each of these parameters corresponds to an empirically derived number without units. These numbers are summed to determine the RMR and the associated rock quality, as shown in Table 2.2 (Bieniawski 1988).

Though the inclusion of the RQD in these rock mass classification systems indicates its usefulness in estimating rock mass strength, it also highlights the limitations of the RQD as a stand-alone parameter. Deere and Deere (1989) point out that the RQD does not directly account for joint characteristics such as filling, roughness, orientation or state of stress. It does not include highly weathered, soft or sheared sections of core – even if the length of those sections is greater than the 10 cm threshold (see equation 2.1). The effects of these latter parameters are, however, included in both the Q and RMR systems.

2.3 The Rock Quality Designation – Best Practices

Illustrated in Figure 2.1 is an example of the RQD measurement procedure.

Table 2.2: The Rock Mass Rating (RMR) and the associated rock quality. The numerical value of the RMR is derived from empirical parameters. Modified from Bieniawski 1988.

RMR	Rock Quality
0 – 20	Very poor
21 – 40	Poor
41 – 60	Fair
61 – 80	Good
81 – 100	Very Good

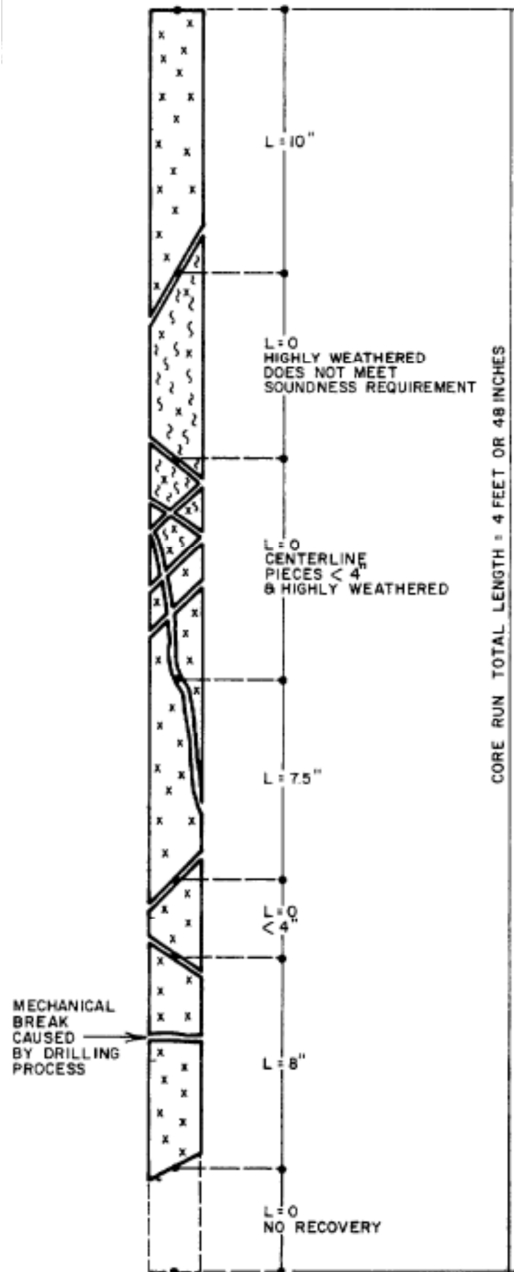


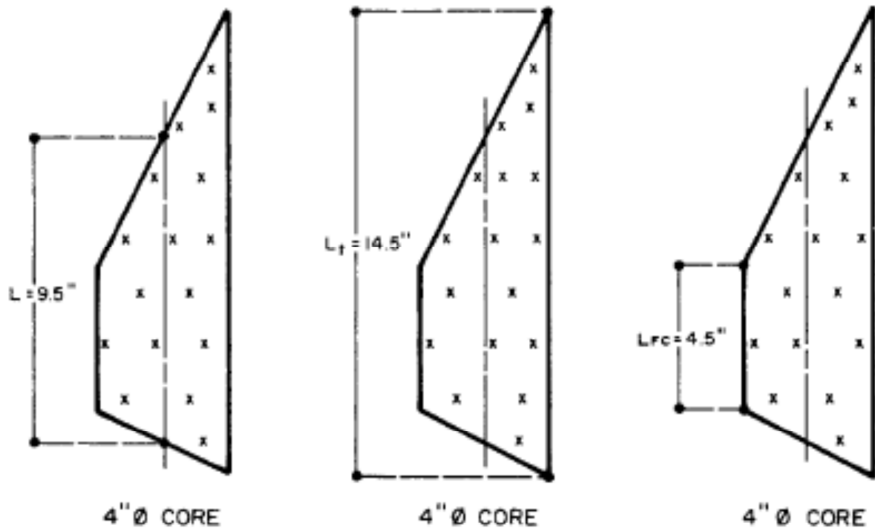
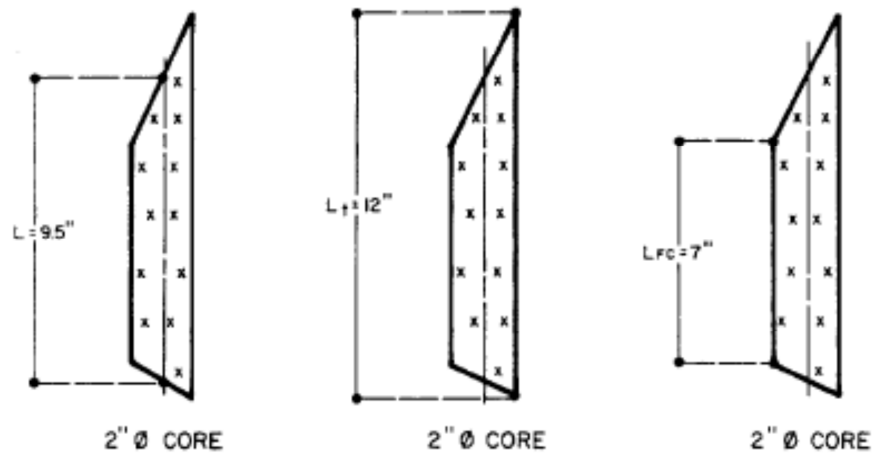
Figure 2.1: Measurement of the RQD. The lengths of core should be measured along the centerline (1 inch = 2.54 cm). Natural fractures should be distinguished from mechanical breaks and highly weathered sections should be excluded. The RQD of this core is 53% which corresponds to fair rock quality. Modified from Deere and Deere (1989).

Some questions come to mind when examining the RQD equation

(Equation 2.1) and measurement procedure (Figure 2.1). First, why are only

lengths of core greater than 10 cm included? Some authors (e.g. Pantelidis 2009) point out that 10 cm is an arbitrary threshold. Deere and Deere (1989), however, selected 10 cm because it represents a reasonable lower limit for a rock mass of fair quality with three or four close to moderately spaced joint sets. Nevertheless, Pantelidis (2009) presents an example of the limitations and potential problems associated with a core length threshold: a rock mass with a joint spacing of 11 cm will have an RQD of 100%, whereas a rock mass with a joint spacing of 9 cm will have an RQD of 0%.

The second question is why measure core lengths along the centerline? As shown in Figure 2.2, the centerline provides a standardized reference which is independent of the diameter of the core – cores of varying diameter can be compared. Measurements which are taken tip to tip or along the fully circular section yield inconsistent results for different core diameters (Deere and Deere 1989).



- | | | |
|---|---|---|
| <p style="text-align: center; margin: 0;">CENTERLINE</p> <p style="margin: 0;">A. CORRECT METHOD FOR CORE LENGTH MEASUREMENT
- LENGTH OF CORE INDEPENDENT OF CORE DIA.</p> | <p style="text-align: center; margin: 0;">TIP TO TIP</p> <p style="margin: 0;">B. INCORRECT METHOD FOR CORE LENGTH MEASUREMENT
- LENGTH DEPENDENT ON CORE DIA.</p> | <p style="text-align: center; margin: 0;">FULLY CIRCULAR</p> <p style="margin: 0;">C. INCORRECT METHOD FOR CORE LENGTH MEASUREMENT
- LENGTH DEPENDENT ON CORE DIA.</p> |
|---|---|---|

Figure 2.2: Comparison of measurement techniques on different core diameters (Deere and Deere 1989). Core diameters in SI units (1 inch = 2.54 cm): two inch diameter core is 5.08 cm; four inch diameter core is 10.16 cm.

The third question is why are highly weathered sections greater than 10 cm not included? Weathering adversely impacts the strength of the rock mass, thus the RQD measures only “hard and sound” core (Deere and Deere 1988). As such, highly weathered rock has an RQD of zero regardless of the length of the intact core sections (Bieniawski 1974).

Descriptions like “highly weathered” and “soft” are open to a certain degree of interpretation. Therefore, a standard definition of highly weathered is important; in one example Bieniawski (1974) writes that weathering extends throughout the rock mass and the rock is partly friable and can be excavated with a pick. The minerals, except quartz, are dull, discoloured and stained. More formally, there are six weathering grades (Dearman 1976, Santi 2006). A description of these grades is presented in Table 2.3.

Table 2.3: The weathering grades of rock (modified from Santi 2006).

Weathering grade	Description	Weathered material
I – Fresh	<ul style="list-style-type: none"> • 100 percent rock • No discolouration, decomposition or other change 	<ul style="list-style-type: none"> • Unchanged from original state
II – Slightly weathered	<ul style="list-style-type: none"> • 100 percent rock • Discontinuity surfaces or rock material may be discoloured 	<ul style="list-style-type: none"> • Slight discolouration • Slight weakening
III – Moderately weathered	<ul style="list-style-type: none"> • Up to 50 percent soil from decomposition of the rock mass 	<ul style="list-style-type: none"> • Penetrative discolouration • Considerable weakening • Large piece cannot be broken by hand
IV – Highly weathered	<ul style="list-style-type: none"> • 50 – 100 percent soil from decomposition of the rock mass 	<ul style="list-style-type: none"> • Large pieces can be broken by hand • Does not readily slake (resistance to wetting and drying) when dry sample immersed in water
V – Completely weathered	<ul style="list-style-type: none"> • The rock is changed to soil such that the original rock texture is preserved 	<ul style="list-style-type: none"> • Considerably weakened • Slakes • Original texture apparent
VI – Residual soil	<ul style="list-style-type: none"> • The rock is completely changed to a soil such that the original rock texture is destroyed 	<ul style="list-style-type: none"> • Soil derived from in situ weathering • None of the original texture or fabric is retained

Deere and Deere (1988) suggest the first two grades – fresh and slightly weathered – be included in the RQD. Moderately weathered (grade III) may also be included, however, they suggest placing an asterisk on the RQD (e.g. RQD = 60%*) to indicate that the rock is not sound. Grades IV, V and VI – highly weathered, completely weathered and residual soil – should be excluded from the RQD.

Mechanical breaks should also be excluded from the RQD because they do not represent the in situ state of the rock mass. Unlike natural fractures, which are the result of geological processes, mechanical breaks result from drilling and poor handling of core. The fourth question is how do mine professionals identify mechanical breaks? The answer is not simple; in many instances even trained and experienced geologists find it arduous. Although it is a well-known, long-standing issue, which many authors agree needs to be addressed (Deere and Deere 1988, Milne et al. 1998, Jakubec and Esterhuizen 2007, Pantelidis 2009), it is difficult to find exactly which properties distinguish these discontinuities from each other in the literature. Resources that do exist list properties which are often very subtle.

According to Deere (1967, 1988, 1989), the lead researcher on the RQD, natural fractures and mechanical breaks have the following properties, summarized in Table 2.4 and illustrated in Figure 2.3.

Table 2.4: Comparison between the breakage surfaces of natural fractures and mechanical breaks (modified from Deere and Deere 1989).

Discontinuity type:	Natural fracture	Mechanical break
Breakage surface	Smooth	Rough
	Weathered	Fresh
	Soft coating of talc, gypsum, chlorite, mica, calcite	Brittle



Figure 2.3: Comparison between the breakage surfaces of a natural fracture (left) and a mechanical break (right). The natural fracture has a weathered, smooth breakage surface, whereas the mechanical break has a fresh, rough surface. The diameter of the core is 47.6 mm. Gabbro with potassium feldspar and quartz veins.

Illustrated in Figure 2.3 are discontinuities consistent with all the natural fracture and mechanical break criteria presented in Table 2.4. These are end-members. For rock with planes of weakness caused by foliation, cleavage or bedding, the breakage surface may be smooth – even for mechanical breaks. Thus, if the breakage surface is also unaltered, the origin of the fracture is unclear. In this, and in other ambiguous cases, Deere and Deere (1988) suggest questionable discontinuities be considered natural. Conversely, well-defined mechanical breaks should be fitted together, the core length measured as though it were intact.

Another commonly applied criterion to distinguish natural fractures from mechanical breaks is the angle of the fracture plane with respect to the core axis. Discontinuities at angles approaching 90° to the core axis are more likely mechanical in origin, whereas lower angle fractures are typically joints or faults. The relationship between the fracture angle and the cause of the breakage is empirical; known from hands-on experience.

Finally, there are some considerations when measuring and calculating the RQD which may not be immediately apparent. The RQD is sensitive to the core diameter, core run and drilling and core logging practices (Deere and Deere 1989).

The first version of the RQD was designed with 54.7 mm diameter core (NX-size) (Deere et al. 1967). Since then it has been found that cores with a diameter equal to or greater than 47.6 mm (NQ-size), such as the HQ- and PQ-

size (63.5 mm and 85 mm, respectively), are also acceptable (Deere and Deere 1989). Core recovery tends to be poorer and breakage more frequent with smaller core sizes. For example the BQ- and BZ-size are not recommended for the RQD; the BQ-size has a diameter of 36.5 mm and the BX-size has a diameter of 42 mm (Deere and Deere 1989).

Heuze (1971) proposed the RQD could be modified for smaller core diameters by shortening the requisite length of the intact core pieces. The intact core pieces included in the RQD would be double the core diameter. For example, intact core lengths greater than 7.3 cm would be included for 36.5 mm BQ-size core. Deere and Deere (1989), however, reject this suggestion in favour of maintaining a standardized approach and for ease of comparison between core logs. They support the established 10 cm standard for small diameter core so long as measurements are taken along the centerline and drilling techniques are sound.

The RQD is a percentage ratio and as such it varies with the value in the denominator – the length of the core run. Deere and Deere (1989) provide the following example: A 30 cm highly fractured zone within massive rock yields an RQD of 90% for a 3 m run, 80% for a 1.5 m run and 40% for a 0.5 m run. Shorter runs artificially lower the RQD, whereas very long runs may overestimate it. For reliable results, Deere and Deere (1989) recommend that the run should ideally not exceed 1.5 m. A core run of 3 m is considered the absolute maximum. Standard core runs are typically 3 m or less.

It is crucial that a *qualified* mine professional, such as a geologist or geotechnical engineer log the core (Deere and Deere 1988). Furthermore, the core should be logged as soon as possible to minimize the number of mechanical breaks that may occur during transport and handling, and to prevent stress-relief breakage.

In summary, to obtain the most reliable results for the RQD, the intact lengths of core must be measured along the centerline, the diameter of the core and the core run must be taken into account, the weathering grade must be assessed, mechanical breaks must be distinguished from natural fractures, and the core must be logged promptly and diligently by competent personnel.

2.4 The Rock Quality Designation – Underground Mining and Core Logging

The RQD is not always measured by a qualified professional or employed as is recommended or intended. Deere and Deere (1988) write that the RQD should be used as a “red flag” to indicate poor engineering conditions. It is not a “stand-alone” design parameter; though it is often used that way - without a thorough account of the local geology. This practice is dangerous because the RQD can underestimate the amount of support required. It is also costly if the need for rock bolts, screens, shotcrete, etc. is overestimated. For example, the danger posed by highly fractured rock may be mitigated if the joints are interlocked and under sufficient stress (Deere and Deere 1989).

Diligent data collection is also a problem. Although there have been substantial improvements to virtually every technological aspect of mine design and operation, Hadjigeorgiou (2012) points out that the quality and quantity of geomechanical data available is still low. The first data typically available are drill core logs. Based on drill core data alone, however, erroneous rock mass assessments are common and may be off by 50% (Hadjigeorgiou 2012).

Data collection is supposed to minimize uncertainty; so why are core logs so unreliable? According to Hadjigeorgiou (2012), and from the author's own experience with core logging, geomechanical data are not always diligently recorded. Typically, geologists have to cope with time constraints – they may have to log hundreds of meters of core each week. Priority is given to observing the economic mineral(s), associated rock types and structures.

Hadjigeorgiou (2012) writes that at one mine, 10 to 15 core boxes are placed on the ground and the geologist “eyeballs” the RQD by quick visual inspection. The engineering department was not aware that sub-standard data collection methods were being used.

2.5 Two-Dimensional (2-D) Imaging

To improve the quality and quantity of data available for mine planning and design, 2-D and 3-D imaging of the rock mass and drill core has been explored. The advantages of using image analysis over manual rock mass discontinuity mapping methods include (Hadjigeorgiou et al 2003):

- Mapping time and effort is reduced;
- A permanent geomechanical database could be developed;
- The quantity and quality of data is increased;
- Exposure to hazardous working conditions is limited.

The first three points are particularly relevant to core logging and the RQD. As mentioned in the previous sections, the diligent recording of the RQD may not be a priority at certain mine sites. In most cases, mine professionals have limited time to process core and thus image analysis could improve efficiency. Storing core requires a significant amount of space. Furthermore, core containing ore is typically split for assay, rendering future RQD measurement impossible. Core considered waste material is often discarded, also preventing future inspection or logging. Images of core avoid these issues. It is inexpensive to store image data and it can be accessed as many times as needed in the future.

Over the past few decades, edge detectors such as Sobel (Gonzalez and Woods 2008) and Canny (1986), and line detectors (Hu et al. 1992, Reid and Harrison 1997, Steger 1998, Reid and Harrison 2000, Gonzalez and Woods 2008) have been developed and successfully applied to 2-D images (digital or scanned conventional photographs) to identify a variety of linear features, including arteries in medical scans (Steger 1998), roads in aerial photographs (Hu et al. 1992, Steger 1998), joint traces on rock faces (Hadjigeorgiou et al. 2003, Reid and Harrison 1997, Reid and Harrison 2000, Lemy and Hadjigeorgiou

2003, Deb et al. 2008) and fractures in drill core (Hardy et al. 1997, Lemy et al. 2001).

A digital image can be considered a matrix with cells (i.e. pixels) comprised of intensity values. Because it is a matrix, a digital image can be processed mathematically; an automated algorithm can be developed to detect the discontinuities, characterize them and compute the RQD (Deb et al. 2008).

Discontinuity traces are detected by abrupt changes in pixel intensity values – light pixels correspond to high intensity readings, whereas the low intensity values represent dark pixels. Fractures in core appear as dark lines or curves cross-cutting the lighter intact surface.

Detection of discontinuities is a multi-stage process. The approaches range from developing relatively simple, day-to-day tools (Deb et al. 2008, Lemy et al. 2001) to site specific analysis involving complex mathematics (Reid and Harrison 2000, Ferrero and Umili 2011). In most cases, however, researchers typically apply a few pre-processing steps to their images to enhance contrast so that difference between the discontinuities and the intact surface is more pronounced. Next, line or edge detectors are applied and/or complex statistical analysis is run (Ferrero and Umili 2011). Several threshold stages may also be used (Hadjigeorgiou et al. 2003, Lemy et al. 2001). Disconnected lines corresponding to discontinuities are then joined with clustering algorithms or Hough transforms and analysis (Deb et al. 2008). The erroneous responses are discarded.

There are essentially two types of edge detectors – gradient and Laplacian (Deb et al. 2008). The most popular edge detectors – Sobel and Canny – are gradient type detectors based on the first derivative of the image intensity values versus distance (Hadjigeorgiou et al. 2003). The Laplacian methods find the zeros of the second derivative. In the literature surveyed, the thresholds used tended to be a fixed value; in some cases a new threshold had to be determined for each image processed (Hadjigeorgiou et al. 2003). A dynamic threshold, such as the standard deviation, is less vulnerable to changes in image properties and is preferable to a fixed number.

After the application of edge detection, Hough transforms are used to isolate features of a particular shape (e.g. a line) within an edge-detected image. This method is tolerant of gaps in feature boundaries and is not strongly affected by image noise (Deb et al. 2008). The major disadvantage is that the shape of interest must be predetermined. It may be difficult to detect a variety of shapes within the same image (e.g. lines and curves).

Of particular relevance to this research is a paper by Lemy et al. (2001) on detecting fractures in drill core and computing the RQD from 2-D images. The methodology of their research is summarized below:

- Image acquisition: Four core boxes photographed in a single image using a 35 mm camera. The camera was mounted on tripod and angled at 90° to target. The camera-to-target distance was 1.6 m. The photograph was scanned at a resolution of 200 dots per inch.

- Image enhancement: Histogram equalization is used to enhance contrast between fractures and intact core. Pixels representing the intact core surface are selected. The other pixel values are recalculated relative to intact core values to increase the range of grey levels.
- Line detection: Steger line detection algorithm (Steger 1998). This algorithm uses the first derivative and a zero crossing detector (finds where the zeros change to non-zeros and vice versa). The output is a binary image with discontinuities in black and intact core in white.
- Break reconstruction: Where line detection algorithms yield discontinuous line segments, neighboring line segments are linked together. The clustering algorithm is based on the smallest distance between segments and the similarity of the angle between segments.
- Elimination of “spurious” breaks: Line segments with a length less than 80% of the core diameter were discarded.
- RQD: A scan line is superimposed along the core axis. The locations of the breaks intercepted by the scan line are recorded, used to measure the intact core lengths and calculate the RQD.
- Natural fractures were not distinguished from mechanical breaks.

The fundamental assumption of these 2-D methods is that pixel intensity corresponds to surface elevation (Reid and Harrison 2000). This assumption may not be valid in every case. Intensity variations are a function of light and shadow;

they are not a true property of the rock mass or drill core. As such, this approach is highly dependent on ambient lighting conditions. Improper lighting can cause shadows and glare that degrade the performance of an image-processing algorithm (Deb et al. 2008). Dark colored core may lack sufficient contrast with fractures, which makes the detection of these discontinuities problematic. Fractures are not the only features identified by edge or line detection algorithms; intensity changes may also be due to rock texture, mineral veins or sedimentary beds (Hadjigeorgiou et al. 2003).

2.6 Three-Dimensional (3-D) Imaging

The problems associated with rock texture and lighting conditions are essentially eliminated with 3-D imaging and models (Umili et al. 2013). In recent years, 3-D laser imaging has been applied to map rock mass discontinuities (Ferrero et al. 2009, Struzzenegger and Stead 2009, Gigli and Casagli 2011, Mah et al. 2011, Longoni et al. 2012, Boivin et al. 2013, Fekete and Diederichs 2013, Mah et al. 2013, Umili et al. 2013). These studies have primarily focused on joint orientation and surface roughness of medium to large rock masses, such as mine tunnels and road cuts. As such, this previous research cannot be directly applied to small targets such as drill core.

Aside from this research (Dixon et al. 2011a, Dixon et al. 2011b, Olson et al. 2013a, Olson et al. 2013b), the use of 3-D imaging to detect fractures in drill core and calculate the RQD does not appear to be published in the literature as

of yet. Ross et al. (2011), however, have developed a “mobile laboratory” to log core at the drill site or core storage area. The laboratory uses sensors to detect the density and magnetic susceptibility of the core, infrared spectrometry to characterize the mineralogy, and X-ray fluorescence (XRF) to detect certain elements. Though the laboratory is also equipped with a digital camera, the authors did not state whether the images were used for fracture detection or computation of the RQD. There was no mention of 3-D imaging equipment.

Most 3-D imaging research to date has been conducted with point clouds. A point cloud is a set of unstructured xyz Cartesian co-ordinates. The x and y co-ordinates represent the spatial (i.e. geographic) location of the points and the z co-ordinates the distance from the digitizer to the target. Image acquisition equipment includes light detection and ranging (Lidar) (Gigli and Casagli 2011, Fekete and Diederichs 2013) and triangulation-based laser digitizers (Mah et al. 2011, Boivin et al. 2013, Mah et al. 2013).

The literature on 3-D imaging consulted for this research project use a variety of innovative techniques to detect discontinuities. In general, however, they involve a similar work flow which is outlined in the following sequence:

- First, due to large file size (a point cloud may contain millions of xyz entries), a feature or area of interest is often selected in order to decrease processing time.
- Next, the raw point cloud may be interpolated and draped with a surface such as a mesh, polygons or triangular irregular network (TIN). Typically

best fit planes are then computed from the interpolated surfaces or clusters of points. To locate discontinuities, such as joints, the area of interest is surveyed in sections with a search rectangle, cube or circle. Various algorithms are then used to detect discontinuities, including thresholds and changes in orientation, slope, and curvature of the interpolated surface.

- Finally, the number of joint sets and their orientation is usually presented with stereonet.

The use of 3-D imaging to detect discontinuities in rock masses is a relatively new research direction and the level of automation varies. Ferrero et al. (2009) point out that to be a truly viable alternative to manual measurements and mapping, both in terms of productivity as well as accuracy, the software must be at least semi-automated. Ferrero et al. (2009) and Gigli and Casigli (2011) outline two levels of automation:

- Manual: the operator interacts with a 2-D or 3-D visual representation of the target rock mass, such as a point cloud or interpolated surface through a graphical user interface (GUI). This interaction could involve highlighting an area of interest for further analysis (e.g. dip angle), fitting a plane or measuring distances by selecting points, etc.
- Semi-automatic to automatic: the operator may still start with a GUI from which part of the rock mass is selected. Once an area of interest is selected, the algorithm will extract the discontinuities and compute the

desired parameters automatically, without further intervention from the program operator.

Both sets of authors prefer the software to be semi-automatic. Otherwise, the models are essentially a digital version of what a geologist would do with a compass and other measuring devices in the field, mine or core facility. Moreover, a manual approach is not systematic, subjectivity has not been minimized or removed, and the time savings are not significant. Reliability still depends on the skill and experience of the operator. A fully automatic system may not be practical at this stage either, as all authors report significant errors and inaccurate results. Ferrero et al. (2009) write that at present it is best to preserve a degree of interaction; it is the best compromise between the advantages offered by 3-D imaging methods while still achieving significant time savings compared to on-site surveys.

2.7 Summary of Recommendations for 3-D Imaging

For 3-D data and imaging of core to be a viable alternative to manual core logging, the RQD measurements should be taken along the centerline, threshold should be dynamic, natural fractures should be distinguished from mechanical breaks, rock texture and contrast issues should be minimized, and the program should be as automated as possible in order to minimize subjectivity and increase efficiency and time-savings.

2.8 Summary

The RQD is a widely used parameter which serves as a “red flag” indicating poor engineering conditions. Furthermore, it is an important component of rock mass classifications, such as the Q and RMR systems, used at essentially every Canadian mine site. However, poor data collection practices, time-constraints, the need for data preservation and the difficulty in distinguishing natural fractures from mechanical breaks all call for a more systematic approach to core logging, fracture detection and the RQD. Progress on these issues has been made over the past few decades with the development of 2-D imaging procedures and algorithms. A significant limitation of this approach is that it relies on changes in intensity. Therefore, rock texture, lighting and contrast issues reduce the reliability of the detection algorithms. Distance-based 3-D imaging measures a true property of the core - fractures are identified by changes in the continuity of core surface – not highlights and shadows.

3. Methods

3.1 Overview

As discussed in chapter 2, an innovative, systematic approach is needed to improve current core logging methods. In this chapter, the distance-based 3-D imaging procedures and algorithms developed for this research project are explained in detail. These algorithms detect fractures in core, distinguish natural fractures from mechanical breaks and compute the RQD. The methods used to compare the performance of established image processing tools and develop the 3-D core models are also described.

The 3-D images were obtained with a non-contact laser digitizer. Each image file is a point cloud of spatially referenced measurements in Cartesian space – x is parallel to the long axis of the core and y parallel to the short axis of the core. The z coordinate is the distance from the digitizer to the core.

The value of z is used to detect changes in the continuity of the core surface in profile. These changes are identified by squaring the difference in z-values between the core profile and a profile model, identifying changes in slope with the first derivative and using the mean as a threshold.

To distinguish natural fractures from mechanical breaks, the edge of the fracture visible within the core box (the fracture trace) is used. The lengths of intact core between fractures are measured in order to calculate the RQD. Using several established image processing tools distance-based images are

compared to intensity-based digital photographs. Core models are constructed from numerous images of the core taken from multiple viewpoints.

3.2 Instrumentation

The 3-D point cloud data were obtained with a Konica Minolta VIVID 9i non-contact laser digitizer. The digitizer is shown in Figure 3.1.

This digitizer uses the light-stripe method to acquire data (Konica Minolta hardware manual). A laser beam is emitted through a cylindrical lens onto a galvano mirror. The motion of the mirror causes the light stripe to pass over the target from top to bottom. The light is reflected from the target, focused by the receiving lens, and received by the charge-coupled device (CCD) detector. The light information received by the CCD is converted to Cartesian coordinates by triangulation. This process generates the 3-D point cloud data. A colour digital image is also obtained at the same time with a red green blue (RGB) filter or band pass (BP) filter (Konica Minolta hardware manual). Figure 3.2 is an illustration of the digitizer measuring principle. Table 3.1 is a summary of select VIVID 9i specifications.

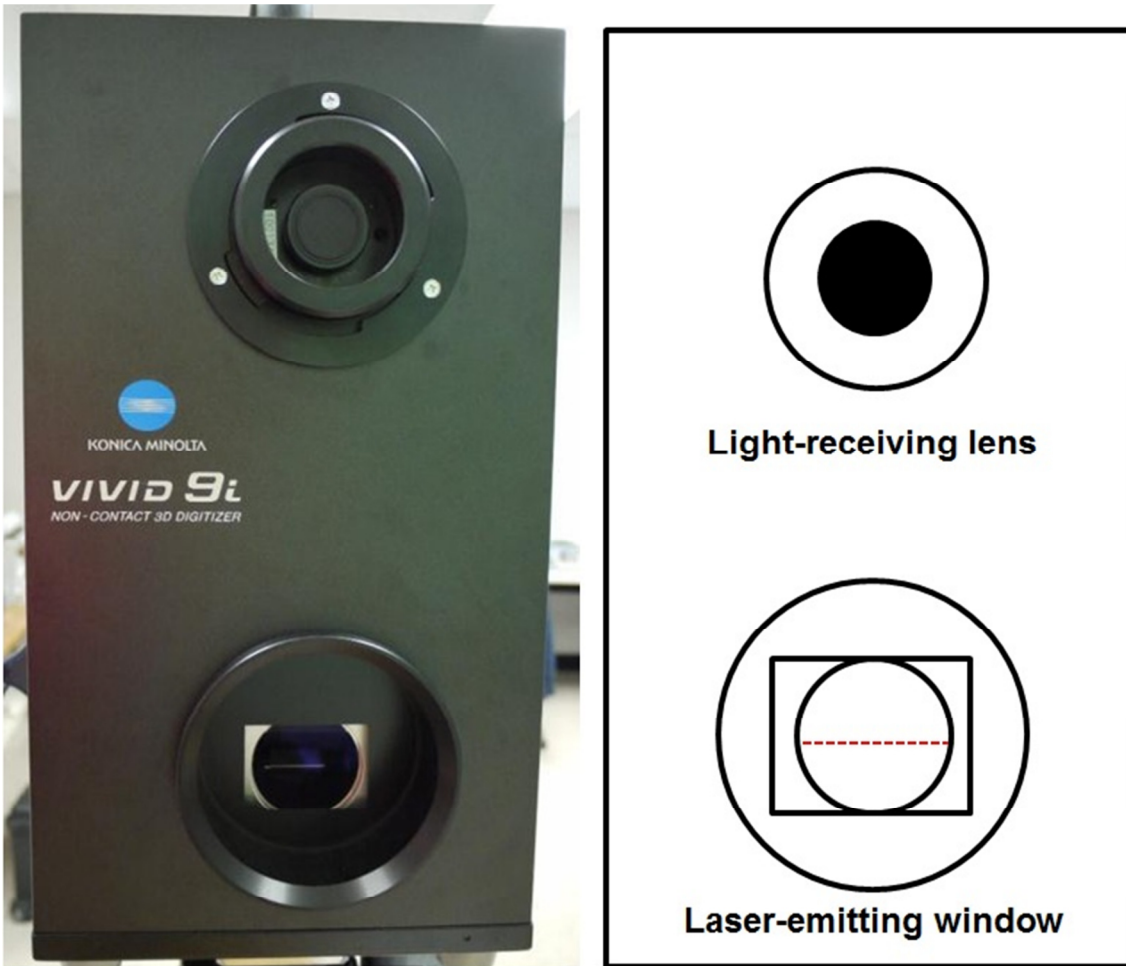


Figure 3.1: Konica Minolta VIVID 9i non-contact laser digitizer. The digitizer enclosure is 221.0 mm wide, 473.5 mm tall and 300.3 mm deep (Konica Minolta hardware manual). The laser beam is emitted to scan the core. A CCD sensor behind the light-receiving lens converts intensity peaks into Cartesian coordinates using triangulation.

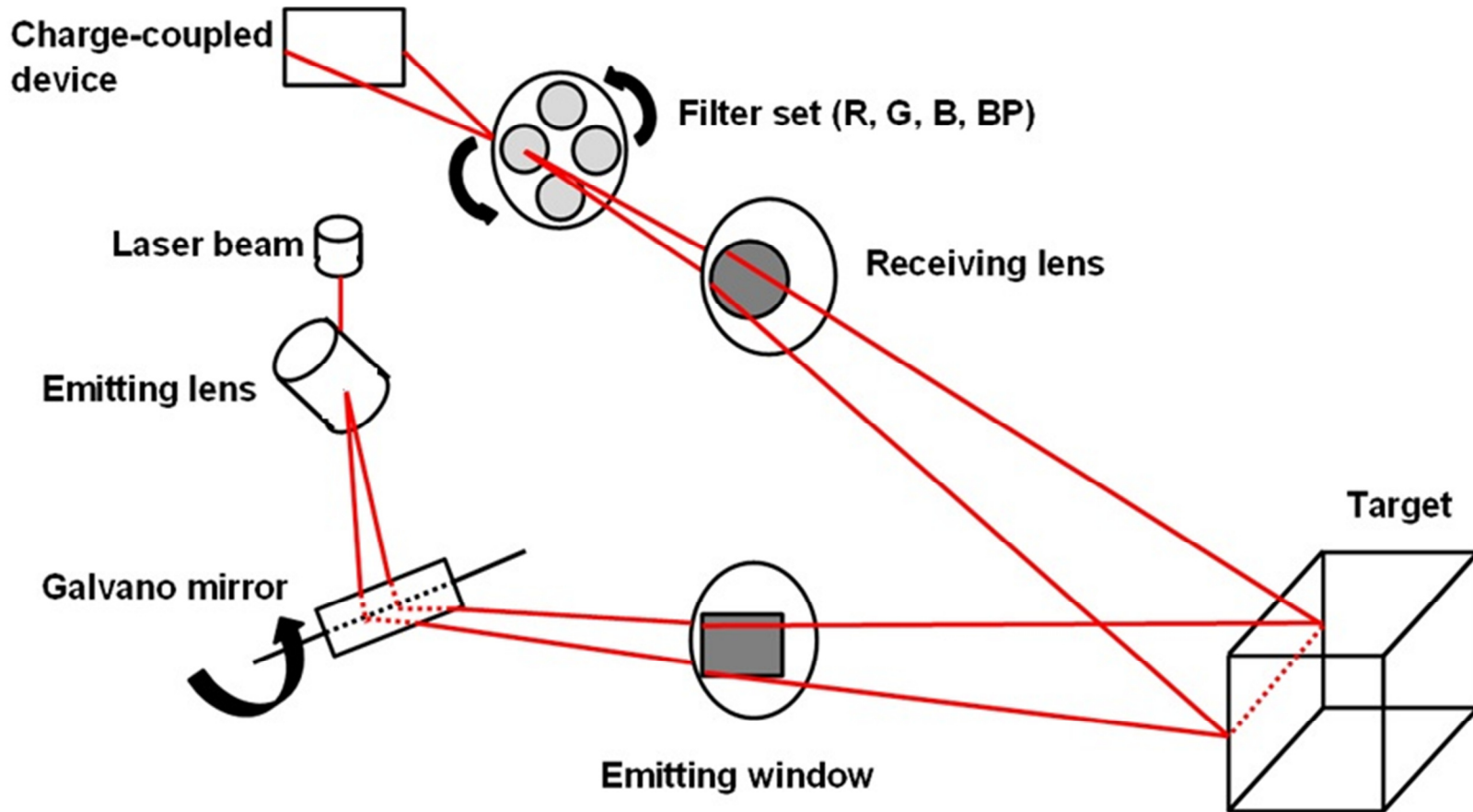


Figure 3.2: Vivid 9i laser digitizer measuring principle (modified from the Konica Minolta hardware manual).

Table 3.1: Summary of VIVID 9i specifications (Konica Minolta hardware manual).

VIVID 9i non-contact 3D laser digitizer specifications	
Interchangeable light-receiving lens	TELE: focal distance $f = 25$ mm WIDE: focal distance $f = 8$ mm
	TELE: field of view angle $\approx 35^\circ$ (0.9 m) WIDE: field of view angle $\approx 14^\circ$ (0.6 m)
Scan range	0.5 to 2.5 m
X direction input range	TELE: 93 to 463 mm WIDE: 299 to 1495 mm
Y direction input range	TELE: 69 to 347 mm WIDE: 224 to 1121 mm
Z direction input range	TELE: 26 to 680 mm WIDE: 66 to 1750 mm
Accuracy XYZ (distance 0.6 m/1.0 m)	TELE: ± 0.05 mm/ ± 0.10 mm WIDE: ± 0.20 mm/ ± 0.40 mm
Precision Z (distance 0.6 m/1.0 m)	TELE: ± 0.008 mm/ ± 0.024 mm WIDE: ± 0.032 mm/ ± 0.096 mm
Input time per scan	2.5 s (four scans per image = 10 s)
Transfer time to host computer	Approximately 1.5 s
Number of output voxels (3D data)	high quality filter on: 640×460
Number of output pixels (RGB data)	640×460
3D data output format	ASCII points
RGB data output format	RGB 24-bit raster
Source wavelength	690 nm
Laser power	Maximum 30 mW
Laser class	Class 2 IEC (International Electrotechnical Commission) Class 1 CFR (Code of Federal Regulators)

3.3 Digitizer Configuration

Two digitizer configurations are used. For fracture detection and the computation of the RQD, the core is scanned in the core box. This will be referred to as the core box configuration. The core is scanned in the box to mimic real-world core logging conditions. As illustrated in Figure 3.3, the digitizer is mounted on a tripod, angled at 90° from vertical. The target core box is placed on the floor, parallel to the front of the enclosure of the digitizer. Parallel orientation is needed so that the emitted laser is projected onto the target at normal incidence, thereby minimizing perspective effects.

The accuracy is ± 0.40 mm using the wide lens at a distance of 0.9 m. The wide-lens allows the greatest digitizer-to-target distance – more of the target can be captured in one image. Even so, the entire length of the core box does not fit in a single image, as described in Figure 3.4. With a field of view angle of roughly 35° and a digitizer-to-target distance of approximately 0.9 m, the size of the image area is about 450 mm × 600 mm. Thus, a 1.5 m core box must to be scanned in three sections; each section at least 0.5 m in length.

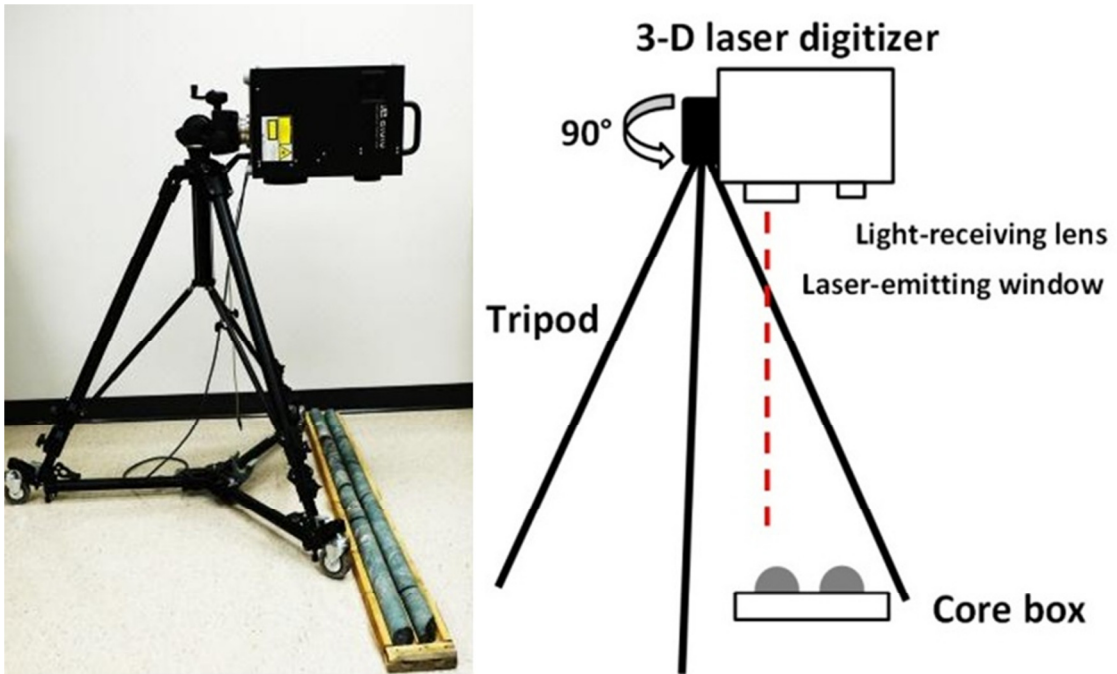


Figure 3.3: Core box configuration. Tripod mounted-digitizer angled at 90° . The front of the enclosure, with the laser-emitting window and light-receiving lens, is parallel to the target core box. Distance from digitizer to core box is approximately 0.9 m.



Figure 3.4: Core boxes imaged in three sections. Two of the four core boxes used for this research. The top box contains 2 rows of core with a diameter of 47.6 mm. The bottom box contains 4 rows of core with diameter of 36.5 mm. The core boxes are approximately 1.5 m long and were imaged in 0.5 m sections.

With the second configuration, for fracture characterization (i.e. natural versus mechanical) and the 3-D core models, the core is placed on a turntable and scanned. This will be referred to as the turntable configuration. The accuracy is ± 0.05 mm using the tele-lens at a distance of 0.6 m. As shown in Figure 3.5, the tripod-mounted digitizer is angled so that the emitted laser beam is approximately normal to the target core axis. The field of view angle is roughly 14° , digitizer-to-target distance is approximately 0.6 m and the size of the image area is about 70 mm \times 125 mm.

The tele-lens is used for individual core segments as it is best for close-range scans, small targets or detailed work requiring high data density. High data density is essential for capturing the subtle changes in the fracture trace which are used to characterize fractures. The turntable was not rotated for fracture characterization. As illustrated in Figure 3.6, to generate the 3-D models of core, a number of scans are taken as the turntable rotates 360° . This scan-and-rotate process is repeated for two additional orthogonal orientations in order to capture the entire core surface in 3-D.

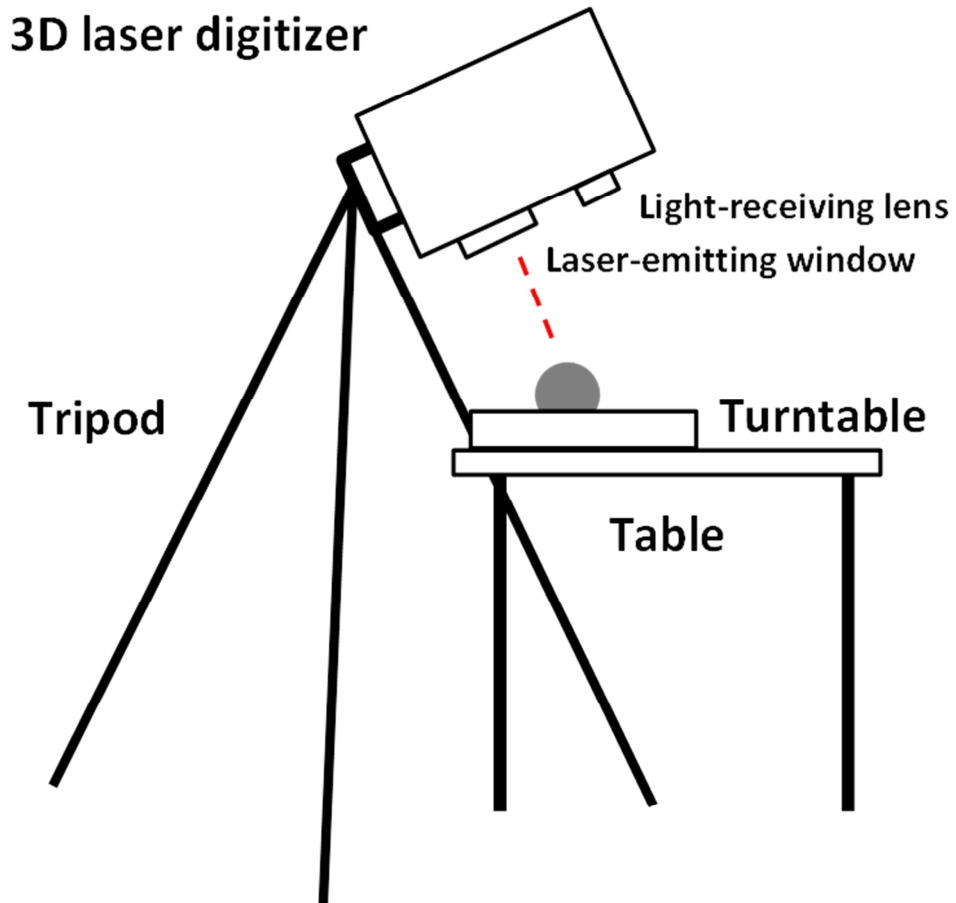


Figure 3.5: Turntable configuration. Tripod-mounted digitizer angled approximately normal to core axis. Distance from digitizer to core is approximately 0.6 m.

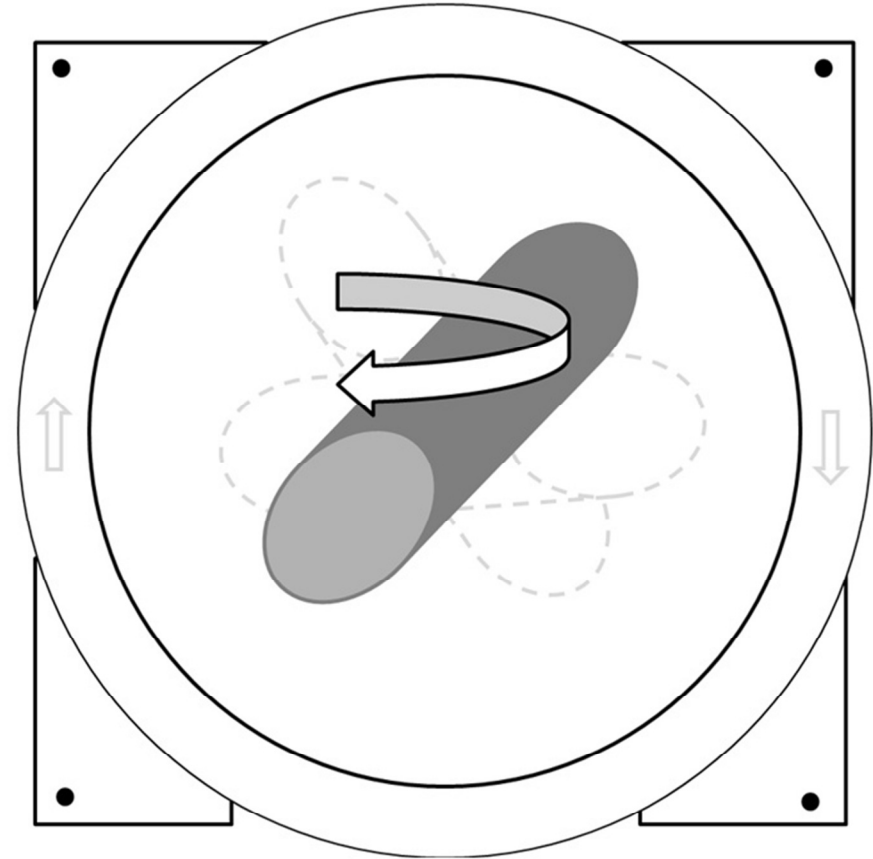
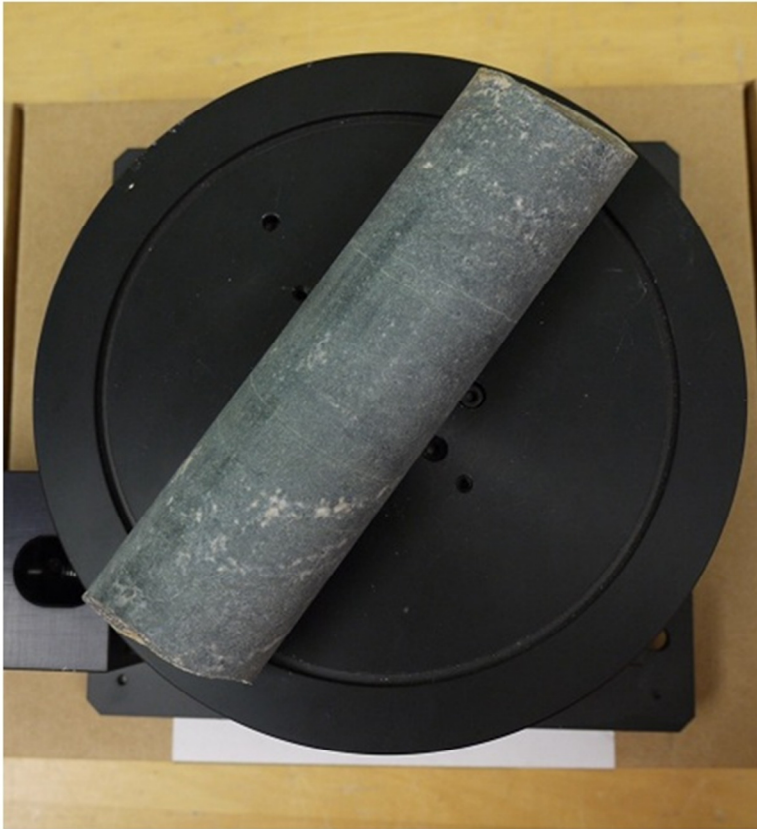


Figure 3.6: The turntable used for close-range work (top view). Scans are taken in user-specified steps (e.g. every 20°) as the turntable rotates 360° . This scan-and-rotate process is repeated for two additional orthogonal orientations in order to capture the entire core surface in 3-D. The turntable diameter is 20.0 cm. The core diameter is 47.6 mm.

3.4 Image Acquisition

The digitizer is connected to a computer with a Windows XP operating system. The image data are acquired with specialized Konica Minolta software called Polygon Editing Tool (PET). Shown in Figure 3.7 (top) is the scan method selection window. “One Scan” is used for the core box configuration and “Step Scan” is used for the turntable configuration.

Also shown in Figure 3.7 (bottom left and right) are the scan options for “One Scan” and “Step Scan”, respectively. Most of the options are the same for both scan modes. “Step Scan” has the additional option “rotation step” which indicates the degree or “step” the turntable rotates between scans. For example, if scans are taken at each 20° rotation, in all three orthogonal directions, there will be a library of 54 images with which to construct a 3-D model.

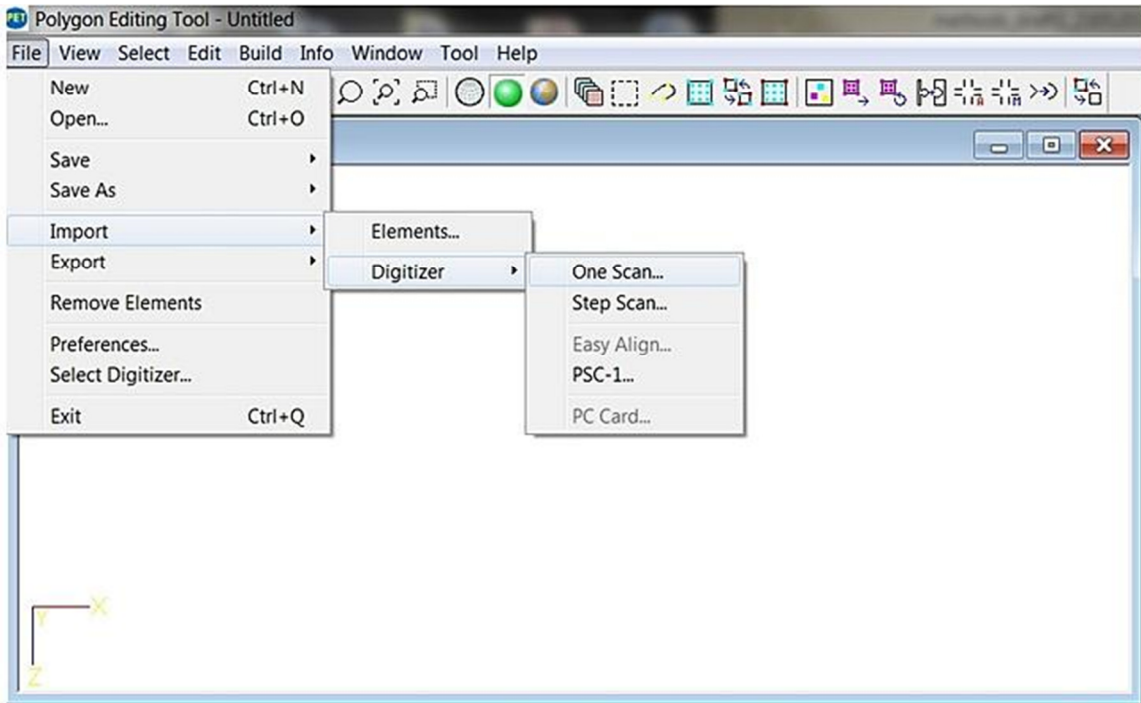


Figure 3.7: PET scan selection (top). “One scan” is used for the core box configuration and “step scan” is used for the turntable configuration. Most of the scan options are the same for “one scan” (bottom left) and “step scan” (bottom right). With “step scan”, however, the rotation step must be selected.

For this project, four scans of the core are taken and then averaged to form a single image; only 1 image is used for the core box configuration and fracture characterization work, whereas 54 images are acquired for each core model. Scan time is 2.5 s/scan, or 10 s for a single image comprised of four scans. Transfer time to host computer is approximately 1.5 s. Therefore the total image acquisition time is about 11.5 s per image. To maximize the quantity of data available, all points are acquired - the reduction rate is 1/1 (i.e. no reduction). The “high quality” (retains only the high certainty points) and “noise” filters are used to remove unreliable data. Various scan settings were tested and the results are summarized in Table 3.2. From Table 3.2 it is clear that the reduction rate controls the quantity of data points. Increasing the number of scans and applying filters improves the quality of the data, as shown in Figure 3.8.

Shown in Figure 3.8 is an RGB color digital photograph of the core box and the raw data from the digitizer, meshed using Delaunay triangulation. The distances measured from the digitizer to the target area are shown in different colours. Cooler colours represent objects farther from the digitizer, such as the floor; warmer colours are associated with the core box and core, which are closer. The fractures are orange, yellow, green and light blue.

Table 3.2: Summary of the scan settings and lenses tested, and the number of data points obtained. The quantity of data increases by decreasing the reduction rate. The quality of data improves by increasing the number of scans and applying the noise and high quality filters. Each of these settings was tested on a core box. The settings highlighted in the bottom row yielded the best results and were used for this research.

Number of scans	Reduction rate	Filter(s)	Number of data points	
			Tele	Wide
1	1/16	None	16,871	16,503
1	1/9	None	30,162	29,445
1	1/4	None	67,633	66,122
1	1/1	None	271,009	264,778
2	1/1	None	271,209	266,079
3	1/1	None	275,787	285,274
4	1/1	None	275,686	292,269
4	1/1	Noise (N.)	278,854	293,988
4	1/1	High quality (H.Q.)	267,774	274,959
4	1/1	N. & H.Q.	270,471	276,240

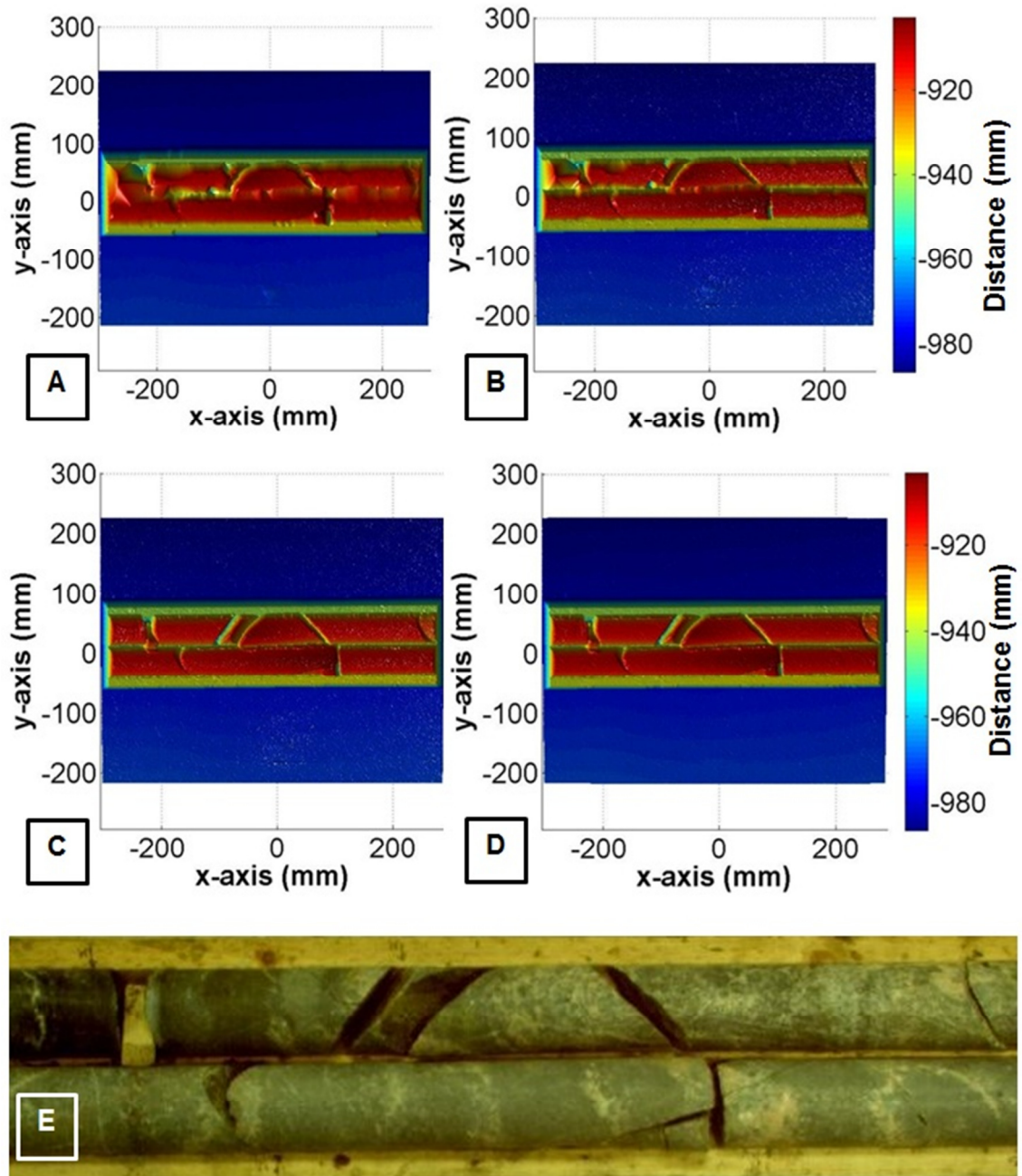


Figure 3.8: Scan of the same cores with different settings. The colour bar represents the digitizer-to-target distance. (A) Number of scans is 1, reduction rate is 1/16. Edges of core and fractures are not rendered well. (B) Number of scans is 1, reduction rate is 1/1. Lower reduction rate increases quantity of data and improves rendering. (C) Number of scans is 4, reduction rate is 1/1. Larger number of scans results in sharper rendering. Noise is visible as scattered white points. (D) Same settings as C with the addition of the noise and high quality filters. Noise is removed. (E) Digital photograph of the cores in the core box.

3.5 Image Properties

Image resolution is 640x460 2-D pixels (a digital photograph) or 3-D voxels. A voxel is a volumetric image element composed of xyz Cartesian coordinates. A collection of voxels forms a point cloud, as shown in Figure 3.9. The digital photographs are in JPEG format and are comprised of RGB data. The 3-D data are in ASCII file format. A typical 3-D file contains three column vectors with over 200,000 triplets of xyz spatial coordinates.

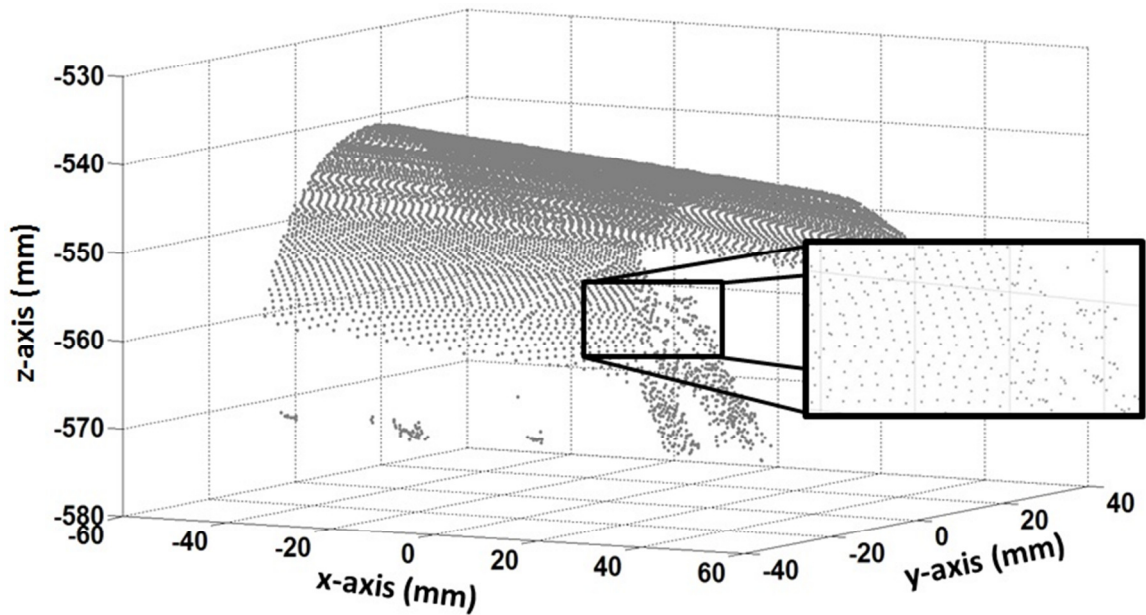


Figure 3.9: A point cloud of a core segment imaged on the turntable using the tele-lens. For visualization purposes, only 10% of the points are plotted. If all of the data were plotted the cloud would be too dense to see the individual points well. However, 100% of the points are used for the algorithms and for data processing purposes. The point cloud concentration of this image is approximately 11 point/mm².

Shown in Figure 3.10 (top), is the coordinate system with respect to the digitizer. Also shown in Figure 3.10 (bottom) is an illustration of the coordinate system with respect to the core. It is important to note that the z-values are always negative; this can be confusing because, as the distance from the digitizer to the target increases, the *value* of z decreases. For example, if the digitizer records z measurements of -890 mm and -940 mm, the distance from the digitizer to the target will have increased by 50 mm, however the value will have decreased because z is a larger negative number. Where possible, the absolute value of z will be used to describe changes in z.

To obtain the xyz point cloud data, the digitizer projects a line parallel to the x-axis, at a constant value of y. The xyz coordinates are acquired line-by-line along x, from top-to-bottom, starting at the maximum y-value and ending at the minimum y-value. In the ASCII file, the data are organized line-by-line. The values in the x column repeat with each new line. The values in the y column are constant for each line along x; the value of y decreases line-by-line. The value of z is the distance from the digitizer to the target area at each xy coordinate. Figure 3.11 is a simplified example of how the data are scanned. Illustrated in Figure 3.12, are the xyz data from a real scan plotted individually.

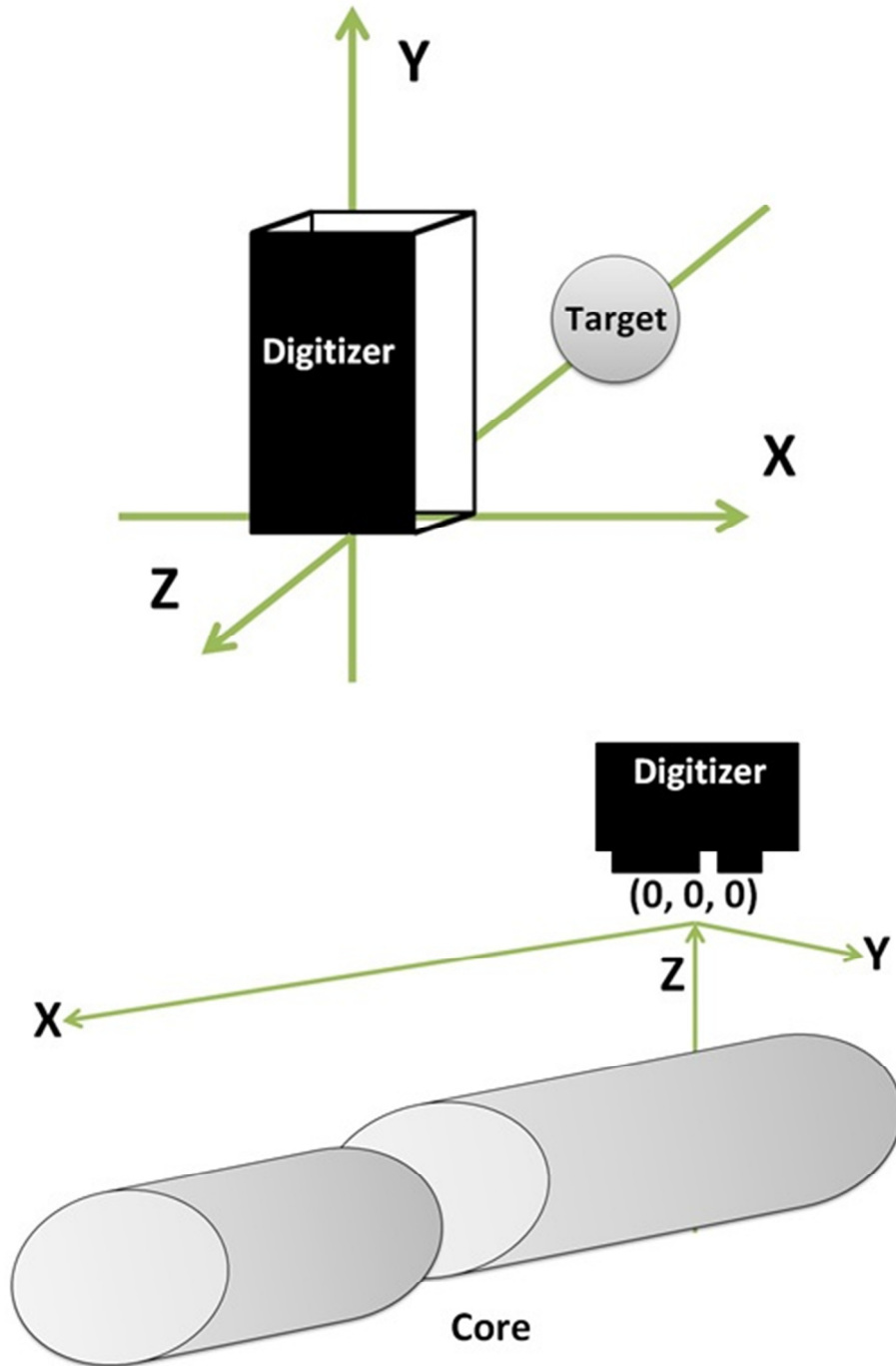


Figure 3.10: The xyz coordinate system with respect to the digitizer (top). The xyz coordinate system with respect to the core (bottom). The origin of this right-hand coordinate system is at the eye point of the digitizer. The arrows indicate the direction in which the value of xyz is increasing. The value of z is always negative. As the distance from the digitizer increases, the value of z decreases.

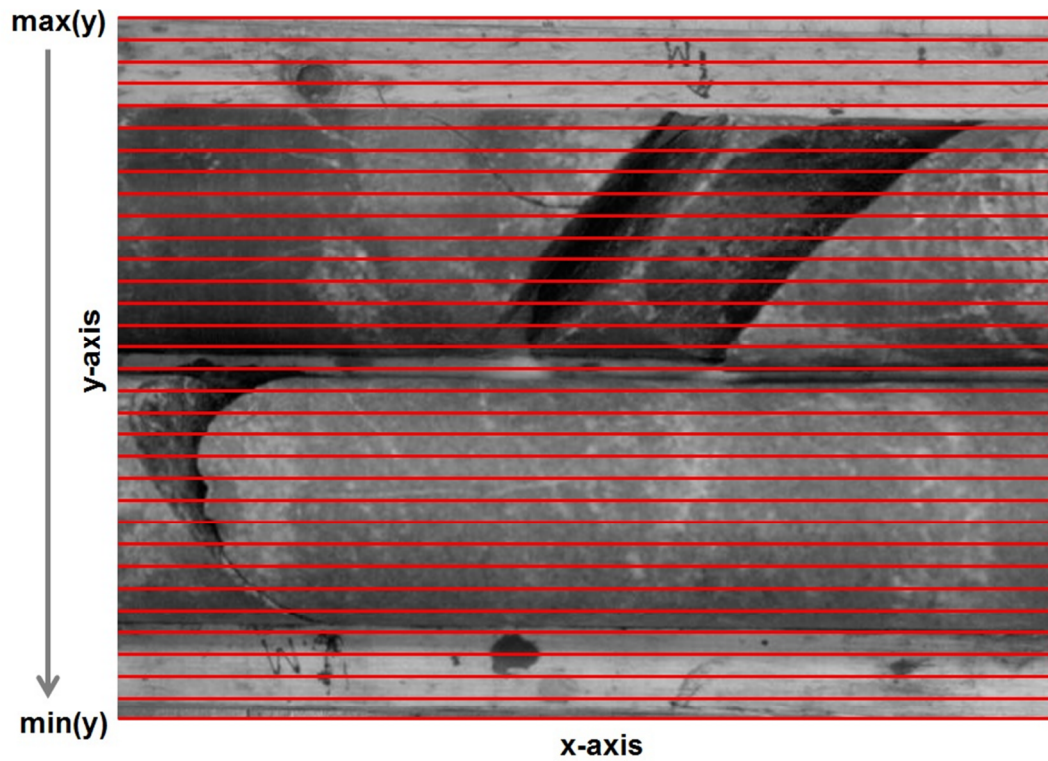


Figure 3.11: Simplified illustration of image data acquisition. The digitizer acquires the first line of xyz data along x, at the maximum value of y. It continues to acquire the data line-by-line, from the maximum value of y to the minimum value of y.

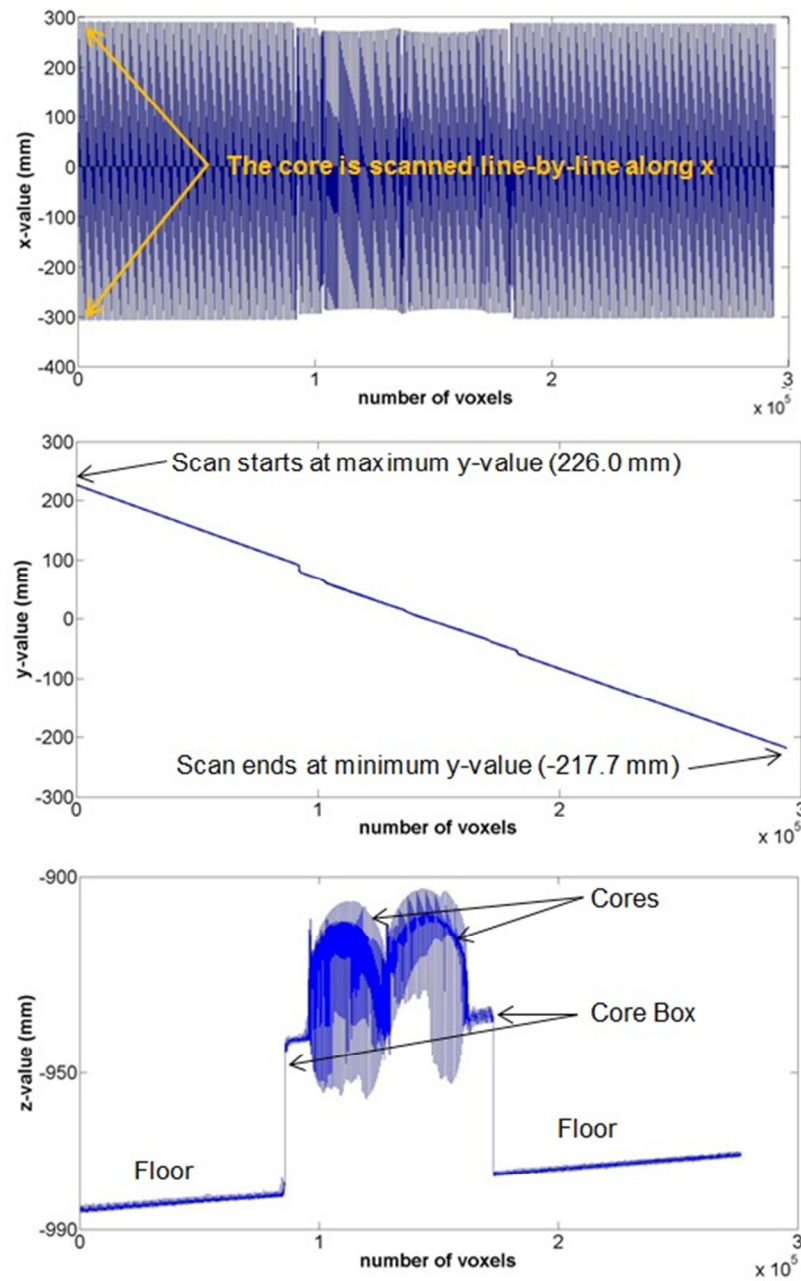


Figure 3.12: The number of voxels (293,988) plotted against the value of x (top), y (middle) and z (bottom). The value of x (top) ranges from -305.4 mm to 289.8 mm. The xyz data are scanned line-by-line along x. The value of y (middle) ranges from -217.7 mm to 226.0 mm. The xyz data are acquired from the maximum value of y to the minimum value of y. The value of z (bottom) is the distance from the digitizer to the floor, core box and cores.

Shown in Table 3.3 is a portion of the ASCII file of the same data presented in Figure 3.12. This file has 293,988 rows and 3 columns. From these data the point cloud concentration – the number of points per unit area – can be determined.

The point cloud concentration is calculated in the following steps:

- x spans -305.4 mm to 289.8 mm
- y spans 226.0 mm to -217.7 mm
- The range of x is 595.2 mm
- The range of y is 443.7 mm
- The scan area is the range_x × range_y
 - Scan area = 595.2 mm × 443.7 mm
 - Scan area = 264,090.2 mm²
- The point cloud concentration is number of points/scan area
 - Point cloud concentration = 293,988 point/264,090.2 mm²
 - Point cloud concentration = 1.1 point/mm².

Given a fixed image resolution, the larger the scan area is, the lower the point cloud concentration will be. A large scan area was desirable for the RQD so as much of the core box as possible could fit in a single image. The size of the features detected by the digitizer is restrained by the point cloud concentration. For the core box configuration, the point cloud concentration is ~1 point/mm²; sub-millimeter features cannot be reliably discerned. It is important to note, however, that the points are not evenly distributed within the cloud. Therefore a fracture with a gap of less than 1 mm may be detected if data points are clustered at that location.

Table 3.3: Coordinate data from an ASCII file. This file has 293,988 rows and 3 columns, corresponding to 293,988 voxels. The value of z decreases abruptly at row 157,001, which indicates a change in the core surface – a fracture.

Row number	x (mm)	y (mm)	z (mm)
1	-305.3830	225.9610	-985.6630
...
156,993	91.8590	-16.1360	-903.7140
156,994	92.7130	-16.1360	-903.6920
156,995	93.5980	-16.1410	-903.9830
156,996	94.4550	-16.1410	-903.9840
156,997	95.3070	-16.1400	-903.9460
156,998	96.1640	-16.1410	-903.9470
156,999	97.3020	-16.1870	-906.6110
157,000	98.3290	-16.2150	-908.1940
157,001	106.8050	-16.8750	-945.6830
157,002	107.4610	-16.8380	-943.5480
157,003	107.7190	-16.7390	-937.9360
157,004	107.9260	-16.6340	-931.9730
157,005	108.4490	-16.5790	-928.8440
157,006	108.9090	-16.5160	-925.2260
157,007	108.8440	-16.3740	-917.1760
157,008	108.9820	-16.2650	-910.9730
157,009	109.8090	-16.2600	-910.6730
...
293,988	289.8840	-217.7150	-970.0510

The turntable configuration scans of core have a point cloud concentration of 11 point/mm². A higher concentration is needed to capture the subtle details of the discontinuity trace, and in turn, to determine whether the origin of a given fracture is natural or mechanical. In addition, a high point cloud concentration provides sufficient detail to facilitate the construction 3-D core models – at least one common feature must be identified between images to connect the sections of the model together. Table 3.4 summarizes the results of point cloud concentration tests using a variety of image acquisition settings and the two digitizer lenses described in the previous sections. These tests were performed to determine the most suitable image acquisition settings and point cloud concentrations for the core box and turntable configurations.

Table 3.4: Test results of the digitizer scan settings and point cloud concentrations. The highlighted point cloud concentrations of approximately 1 point/mm² and 11 point/mm² are used for the core box and turntable configurations, respectively.

Number of scans	Reduction rate	Filter(s)	File size: full scan (xyz triplets)		Point cloud concentration (z point/mm ²)	
			Tele	Wide	Tele	Wide
1	1/16	None	16,871	16,503	0.7	0.06
1	1/9	None	30,162	29,445	1.2	0.1
1	1/4	None	67,633	66,122	2.6	0.3
1	1/1	None	271,009	264,778	10.6	1.0
2	1/1	None	271,209	266,079	10.6	1.0
3	1/1	None	275,787	285,274	10.7	1.1
4	1/1	None	275,686	292,269	10.7	1.1
4	1/1	Noise (N.)	278,854	293,988	10.9	1.1
4	1/1	High quality (H.Q.)	267,774	274,959	11.3	1.1
4	1/1	N. & H.Q.	270,471	276,240	11.4	1.1

3.6 Image Processing and 3-D Modeling Software

All image data for fracture analysis - ASCII files with x, y and z column vectors, point clouds and digital photographs - are processed within the MATLAB (matrix laboratory) numerical computing environment and with the MATLAB image processing toolbox. All code developed for this project was generated within MATLAB. MATLAB is used because it is specifically designed to perform operations on data in vector and matrix form. The image processing toolbox contains a wide range of boundary and object detection functions which can be applied to grey-scale images (MATLAB, 2012).

The 3-D models are constructed with PolyWorks 3-D visualization software. PolyWorks is designed to perform point cloud engineering in order to virtually assemble digitized product components. It is used primarily by the automotive, aerospace and consumer goods industries. PolyWorks, however, has also been used to construct 3-D models of geological materials such as meteorites (e.g. Smith et al. 2006, McCausland et al. 2011) (PolyWorks, 2011).

3.7 Discontinuity Detection

Overview:

Discontinuities are detected using an xz profile parallel to the long axis of the core. This approach is used in order to mimic the centerline method recommended by Deere and Deere (1989). In addition, applying a threshold to the curved surface of the core – rather than a linear profile – produces erroneous results; the fractures *and the edges of the core* are below the threshold.

Four profile methods were developed – the detrend method, the difference method, the difference squared method, and the discrete local first derivative method. For each method, the user selects a single core from the total scan. The algorithm locates the centerline, extracts the xz data, compares the data to a model or takes the first derivative, then applies a threshold in order to detect the fractures. Each profile method is tested with the several different thresholds – one standard deviation, two standard deviations, the variance and the root mean square error (RMSE). For the “detrend” method, the mean is also used as a threshold.

The xy coordinates are used to spatially reference fractures in core; x is parallel to the long axis of the core and y is perpendicular (i.e. parallel the short axis of the core). As shown in Figure 3.10 (bottom), the z coordinate is the distance from the digitizer to the core. The value of z is used to identify changes in the continuity of the core surface. As illustrated in Figures 3.13 and 3.14, where the core is fractured, z has a higher absolute value.

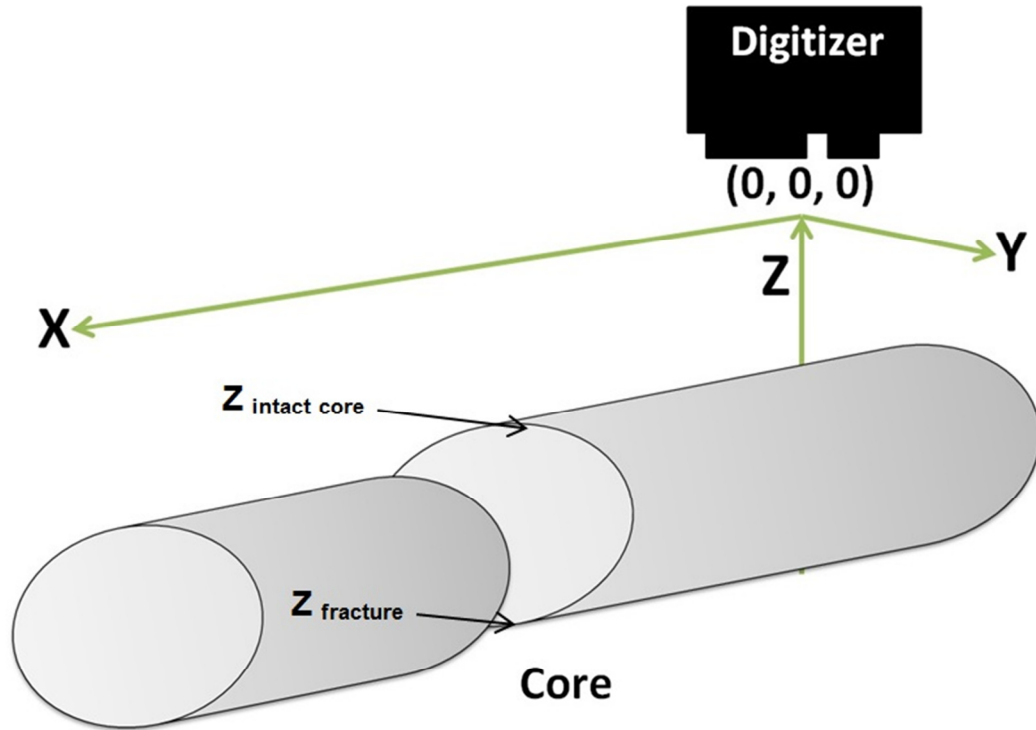


Figure 3.13: The intact core surface is closer to the digitizer than the fracture. At fracture locations the absolute value of z increases.

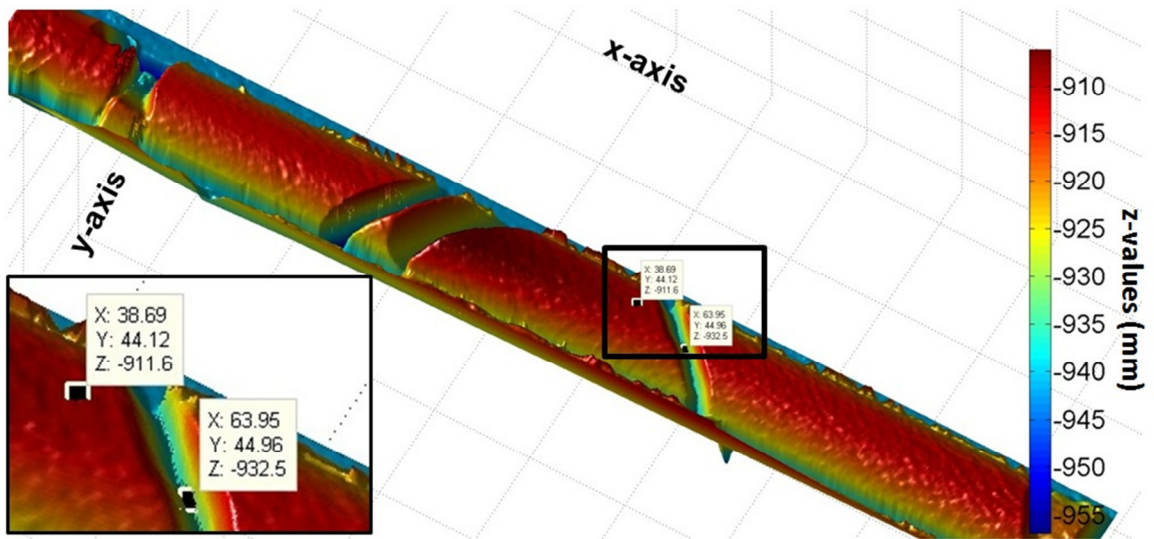


Figure 3.14: A change in z of 20.9 mm between the intact core surface (-911.6 mm) and the fracture (-932.5 mm). The colour of the fractures depends on the depth to which the digitizer was able to scan. This scan depth is primarily a function of the amount of space between discontinuities.

As shown in Figure 3.14, the colour of the fractures depends on the depth to which the digitizer was able to scan – a function of the amount of space between discontinuities. Thus, fractures will be defined as open (segments of core with a gap greater than 1 mm) or tight (segments of core with a gap of approximately 1 mm or less). Tight fractures are represented by fewer data points and the change in z-values is less marked. As a result, tight fractures are more difficult to detect in general, as illustrated in Figure 3.15.

A large amount of the scan data, such as the floor and the core box are not required for fracture detection. When the program is run, a graphical user interface (GUI) appears. As illustrated in Figure 3.16, through the GUI, the user selects four corners around the core of interest with the mouse to form a box. The core data within this box are retained for further processing. The data outside the box are discarded.

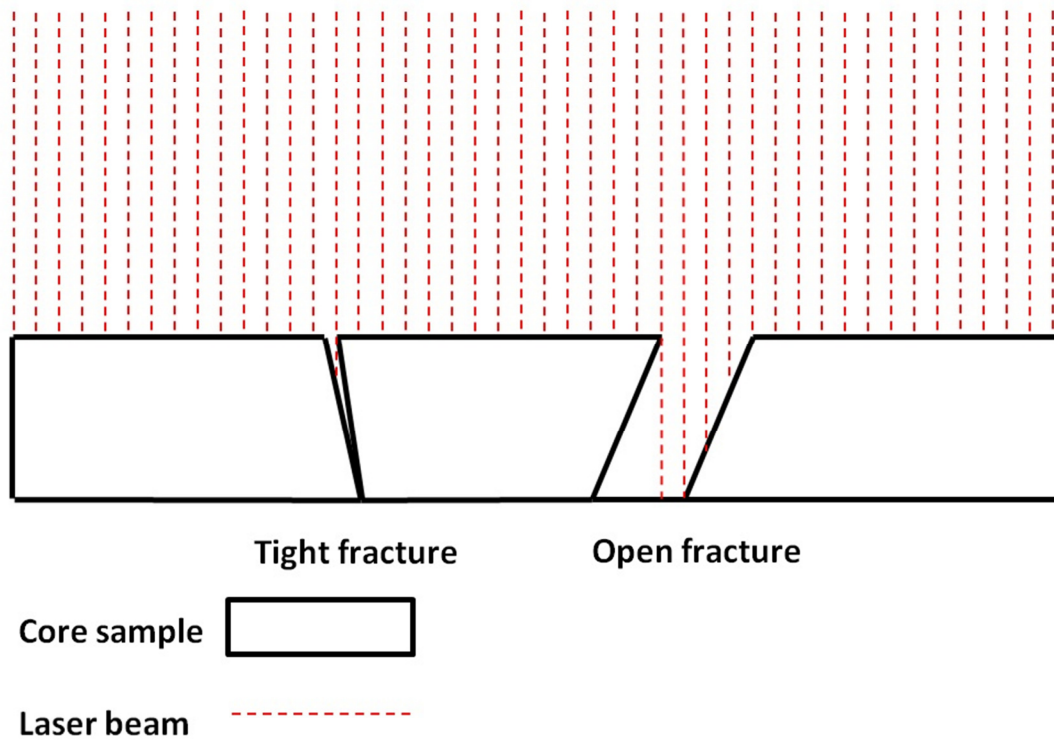


Figure 3.15: Tight fractures are represented by fewer data points and the change in z-values is less marked. In this example, there is only one data point to represent the tight fracture on the left, whereas four data points are captured for the open fracture on the right, two of which span the diameter of the core (i.e. the maximum fracture depth).

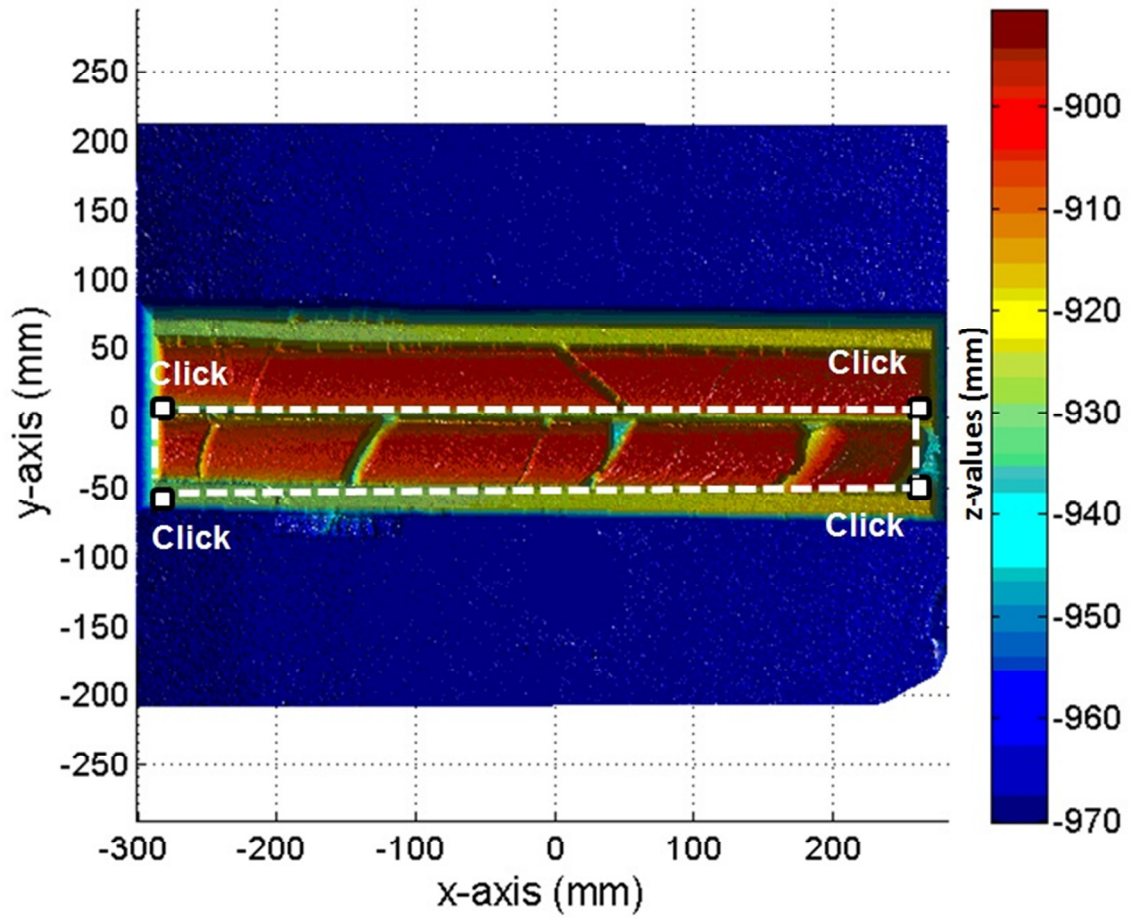


Figure 3.16: The user selects the area of interest through a GUI by clicking four corners around the core. The data within the box are retained for further processing and the rest are discarded.

Illustrated in Figure 3.17, is the single core selected for analysis in Figure 3.16. File size is reduced from the total scan size of 270,214 xyz entries to 35,240 xyz entries for the single core. Processing time is significantly decreased and features not easily observed from the total scan are elucidated. For example, there is a small angle between the core and the digitizer; near the maximum x-values ($x \approx 225$ mm), the core ranges from light blue to red, while close to the minimum values of x ($x \approx -300$ mm), the core ranges from dark blue to orange. This perspective effect occurred because the core is approximately 1 cm closer to the digitizer at the maximum x-values. In addition, the relationship between fracture gap and the range of z-values within fractures is more evident. The fracture near the center of the core ($x \approx -25$ mm) is red to orange which indicates it has a small range of z-values and is tight. The other four fractures are more open and have a wider range of colours and z-values.

Threshold Properties:

The change in z-values is the basis for fracture detection. Points with a large range of z-values are considered fractures and points with a small range of z-values are considered intact core. A threshold, below which all points are considered fractures, can be used to identify discontinuities, as shown in Figure 3.18. However, because the core is cylindrical, z-values at the edges of the intact core would be below the threshold. The edges of the core would be counted as fractures, as illustrated in Figure 3.19. Conversely, a tight fracture may not be detected if its lowest z-value (highest absolute z-value) is above the threshold.

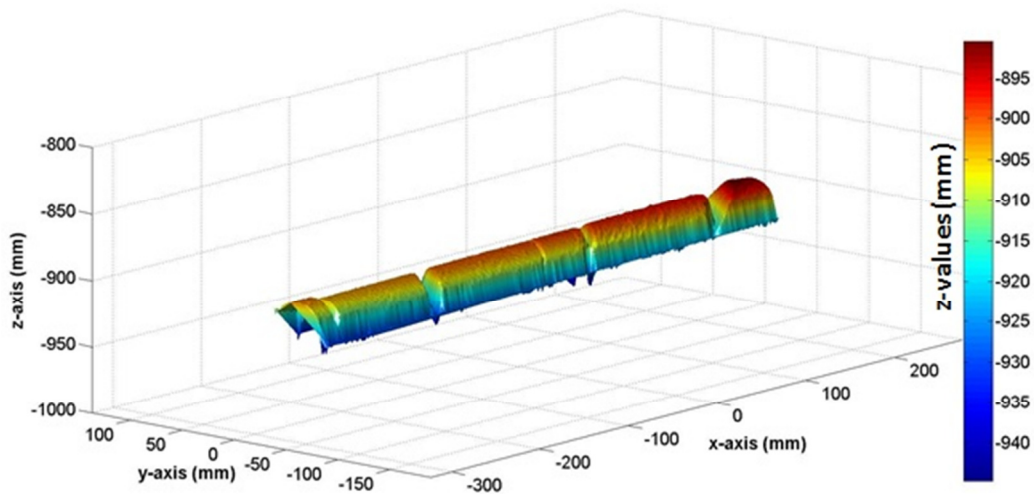
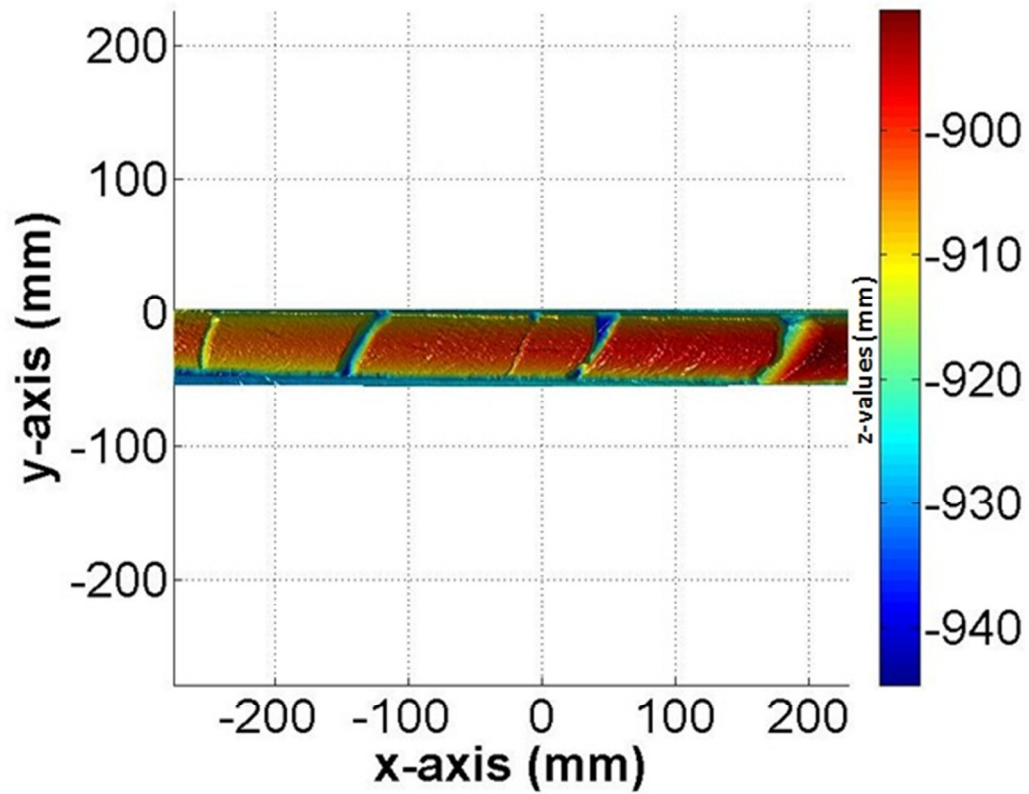


Figure 3.17: The single core selected for further processing plotted in xy space (top) and xyz space (bottom). At the maximum values of x, the core surface is light blue to red, whereas it is dark blue to orange at the minimum values of x. This perspective effect is caused by a small angle between the digitizer and the core.

-903	-902	-911	-945	-905
-905	-908	-910	-947	-900
-906	-912	-940	-938	-901
-903	-909	-937	-907	-911
-901	-930	-904	-902	-901

(A)

-903	-902	-911	-945	-905
-905	-908	-910	-947	-900
-906	-912	-940	-938	-901
-903	-909	-937	-907	-911
-901	-930	-904	-902	-901

(B)

			■	
			■	
		■	■	
		■		
	■			

(C)

Figure 3.18: Example of the threshold concept. For this example, the threshold is less than or equal to -920. Image (A) is the raw data. The highlighted data in (B) are below the threshold. On image (C) the feature of interest is identified. In this case, the data are converted to binary black and white. Modified from Hadjigeorgiou et al. (2003).

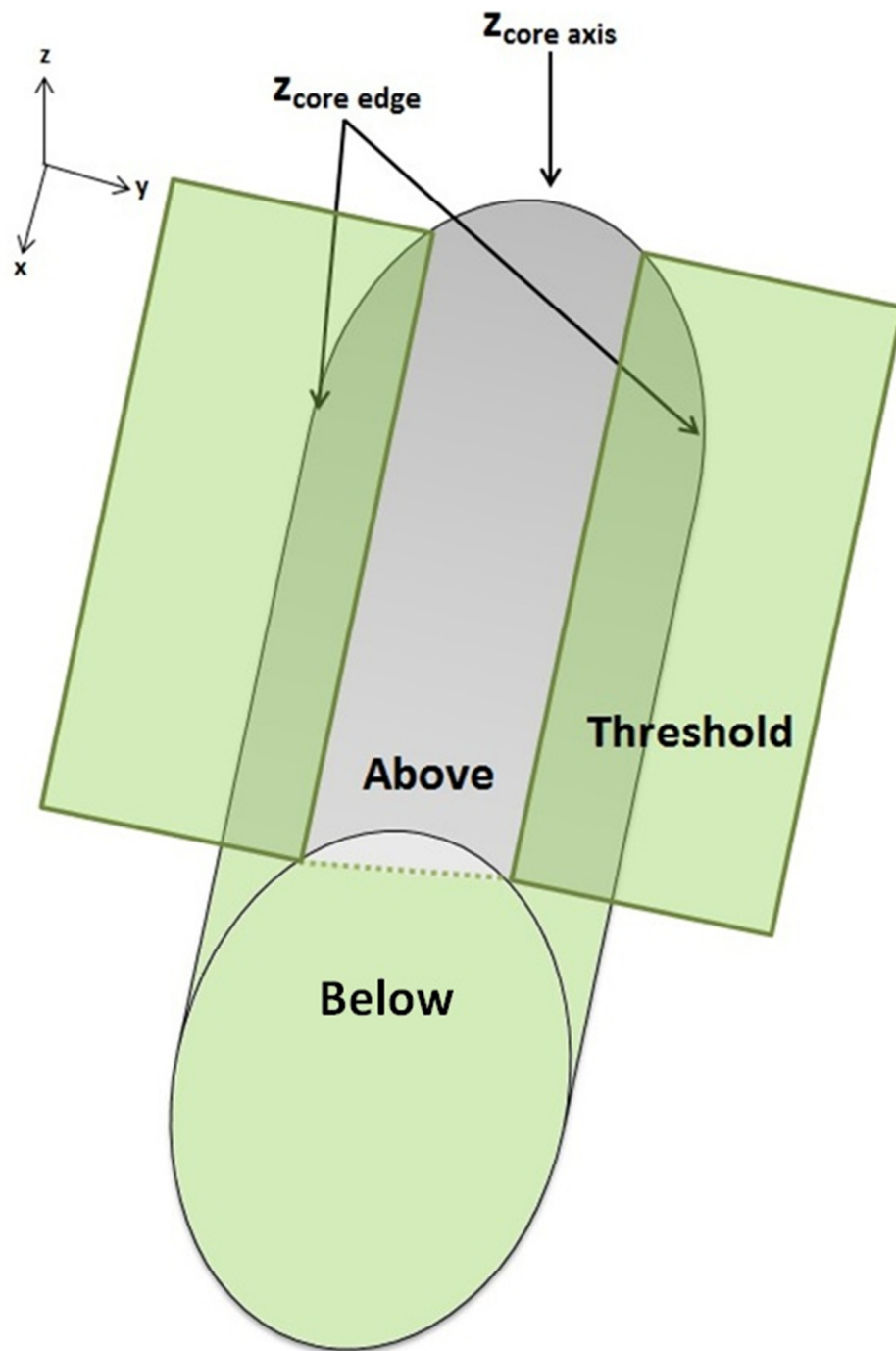


Figure 3.19: A threshold applied to z-values. The edges of the core are below the threshold and would be counted as fractures.

As illustrated in Figure 3.20, one solution to the threshold problem is to take a profile of z-values along the length of the x-axis at the median value of y. The algorithm uses the minimum and maximum values of x to find the length of x. Half a mm is added to each side of the median y-value to form a long, thin rectangle. Rectangles with a width of less than 1 mm did not capture enough z-points. At y equal to 1 mm, the point cloud concentration was approximately 1.2 z-point/mm² (595 z-points divided by 503.9 mm²), which is consistent with data density of the complete scan. All z-values that lie within this rectangle are extracted from the single core scan to form the profile.

Profile Reference System:

The profiles are taken from 4 different boxes of core; referred to as core box 1 through 4. Because the entire box cannot fit in a single image, the core box is divided into 3 sections – A, B and C. Core boxes 1 and 3 contain 2 rows of core, and core boxes 2 and 4 contain 4 rows of core. In total there are 12 rows of core. These rows of core were imaged in 3 sections. Therefore, 36 profiles were used for this research. Illustrated in Figure 3.21 are the core box sections and rows.

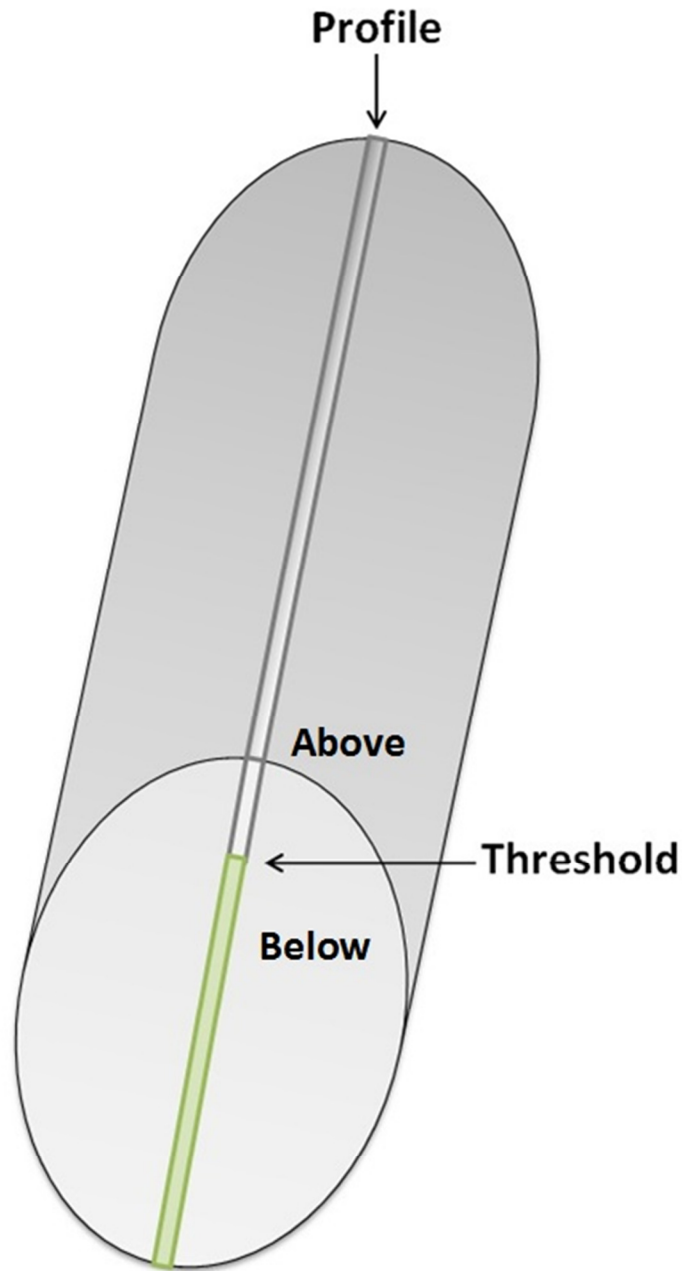


Figure 3.20: The profile of xz -values is taken along the length of the x -axis at the median value of y .

Core Box 1

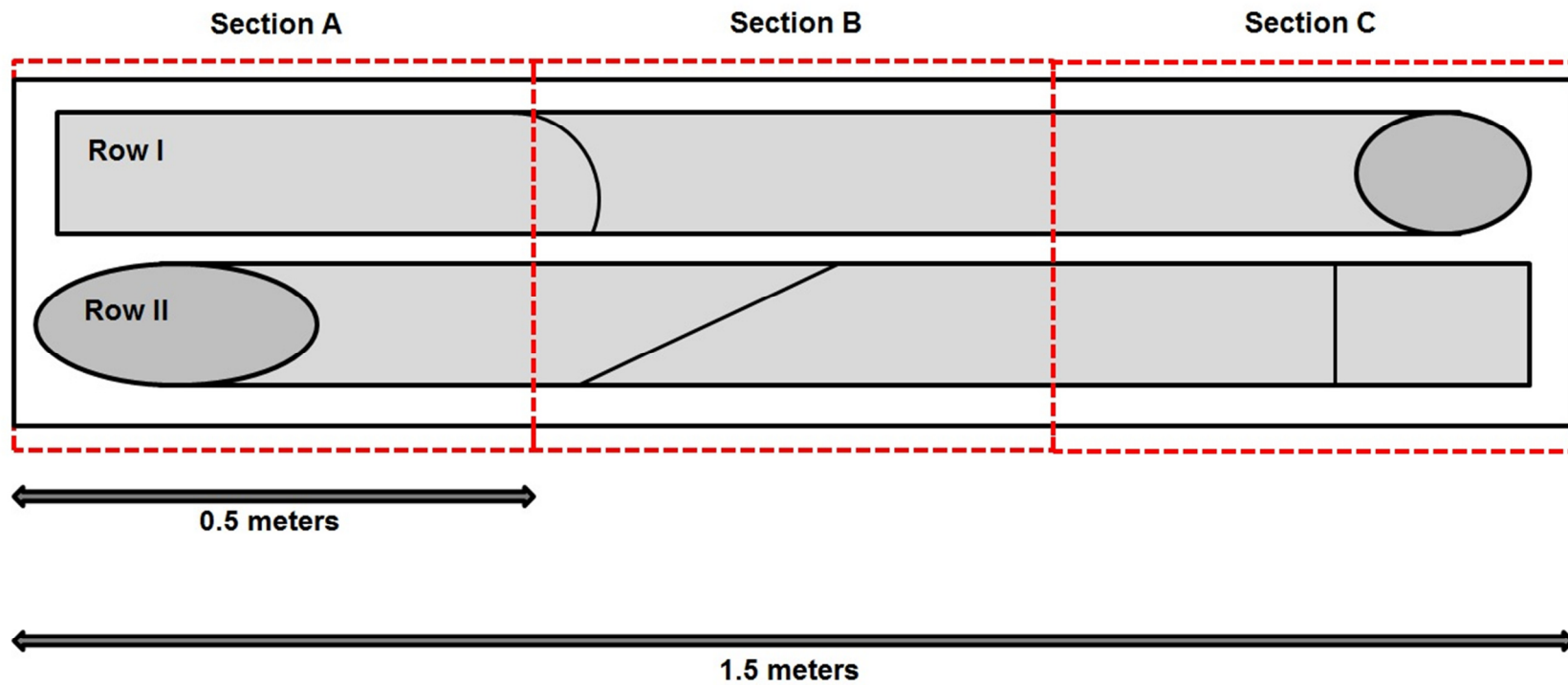


Figure 3.21: Profile reference system. The core box did not fit in a single image. Each core box is 1.5 m long and was imaged in 0.5 m sections. There were overlaps between adjacent sections of approximately 5 cm - 10 cm. For example, Section B Row 1 may overlap with Section A Row 1 or Section C Row 1.

Profile Properties:

As illustrated in Figure 3.22 (top), the profile data are plotted in the xz plane. From this profile several key features are revealed. Most importantly, there are five clusters of points approximately perpendicular to the main trend – these are the fractures. At the extreme ends of the profile there are points above the trend. These are due to small rock fragments or other debris lodged under lengths of core. This debris was left in place because, in a real-world context, it is unlikely that it would be removed. The tight fracture near the center ($x = -15.9$ mm) has three (possibly four) corresponding z-points; the range of z-values is small compared to that of the other four discontinuities. Finally, the perspective effect discussed previously created the sloped trend in the data.

As illustrated in Figure 3.22 (bottom), this linear trend can be removed with a MATLAB function called “detrend”. This function computes the least-squares fit of a straight line to the data and subtracts the resulting function. Essentially the data are re-plotted to fit a horizontal best fit line. Thus the mean becomes a very small number close to zero.

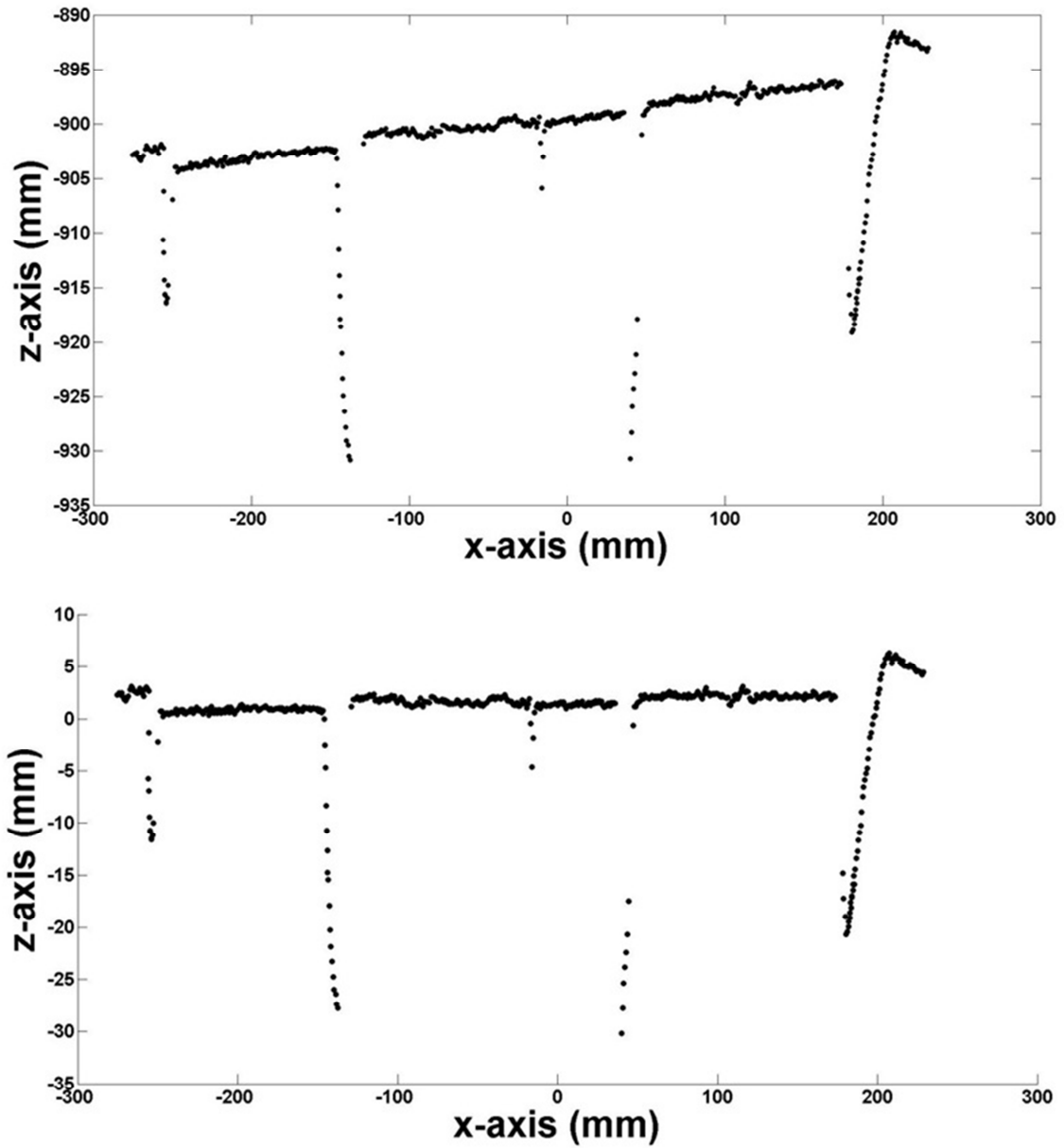


Figure 3.22: A profile along the core at the median value of y before (top) and after (bottom) subtracting the best-fit linear trend to remove the perspective effect. The mean is reset to a number close to zero.

3.8 Discontinuity Detection – Profile Methods

Preliminary Method 1: The Difference:

Though it is easy to visually identify discontinuities from the profile shown in Figure 3.22, the objective is to automate the detection of fractures. Toward this end, a profile model was created, with which the profile taken from the real core is compared, as shown in Figure 3.23. The profile model represents an intact, unbroken version of the real core along the centerline. The profile model algorithm finds the value of z at the endpoints of x – the first and last xz pairs. The value of z between the endpoints is interpolated at equal intervals of 1 mm.

As illustrated in Figure 3.24, the z -values of the real core profile are subtracted from the z -values of the model profile (see equation 3.1). Where the real core is intact, the difference is very small. The difference is much greater at fracture locations.

$$Difference = z_{profile\ model} - z_{core\ profile} \quad (3.1)$$

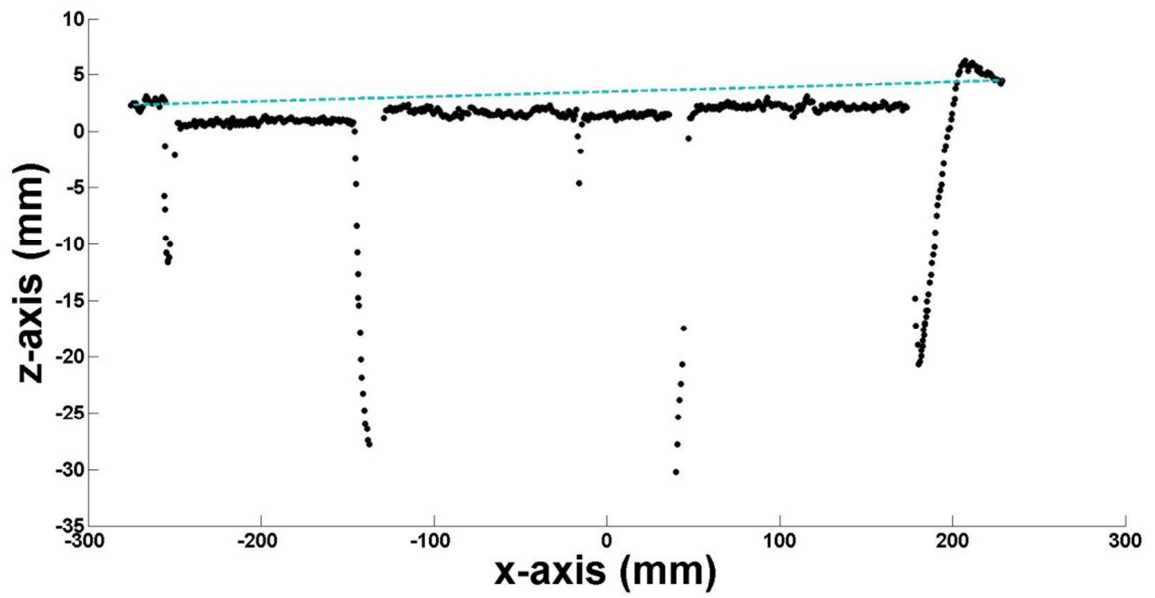


Figure 3.23: The blue dashed line is the profile model, which represents the intact core surface. The model is generated by interpolating between the value of z at the initial and final x -values. In this case, 593 points are interpolated between 2.3 mm (z -value at $x=-254.7$ mm) and 4.5 mm (z -value at $x=228.8$ mm).

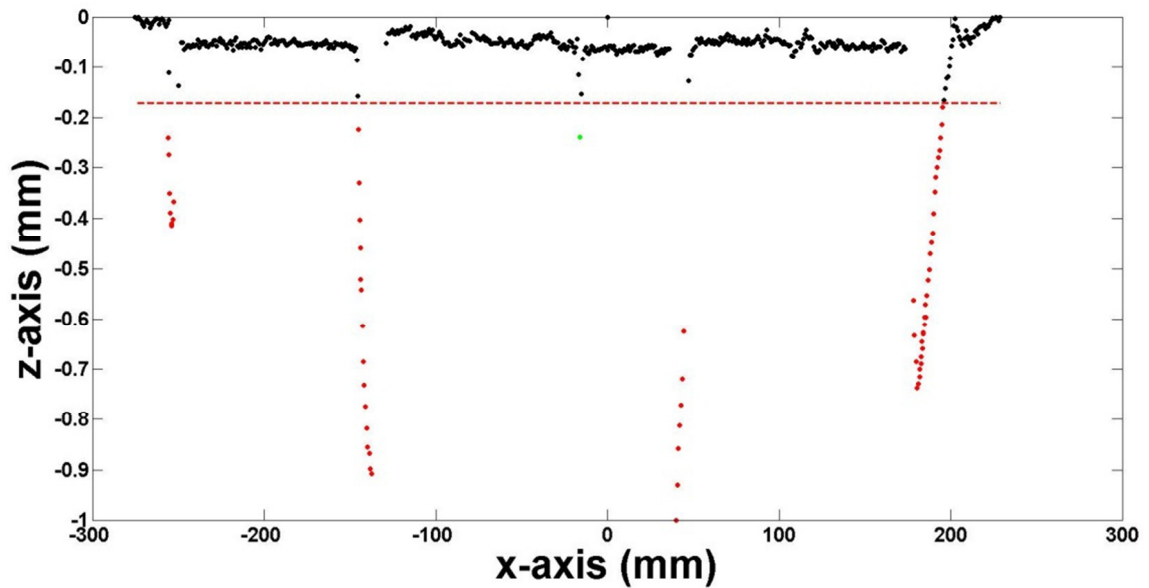


Figure 3.24: The difference between the profile model and the profile of the real core. Note the values on the z-axis are normalized to 1 for comparison between profiles. These normalized values are multiplied by negative one for visualization purposes; to look consistent with the original profile, the z-values are negative. For this example, the fracture detection threshold is the standard deviation of the difference - the red dashed line. Black dots represent data above the threshold, counted as intact core. The red dots below the threshold core are identified as fractures. Only one point is detected for the tight fracture, represented by a single green dot. Single points below the threshold are typically due to anomalous data or to scatter along the intact core surface. As such, these points are not counted as fractures.

All five fractures have at least one point below the threshold. The four open fractures have multiple points which span a wide range of z-values. One point from the tight fracture is below the threshold. Single points are not counted as fractures because they are typically due to anomalous data or to scatter along the intact core surface. Given the poor performance of this method for tight fractures, it was not further developed or tested. Instead, it was improved by squaring the difference between the profile model and the real core profile.

Method 1: Difference Squared:

To reduce scatter along the intact core surface and to highlight the fractures, the difference is squared (see equation 3.2). Note that squaring has no physical significance; it is simply a means of amplifying the difference. As illustrated in Figure 3.25, all five fractures have points below the threshold. The tight fracture has two points below the threshold, instead of a single point as with the previous method.

$$\textit{Difference squared} = (z_{\textit{profile model}} - z_{\textit{core profile}})^2 \quad (3.2)$$

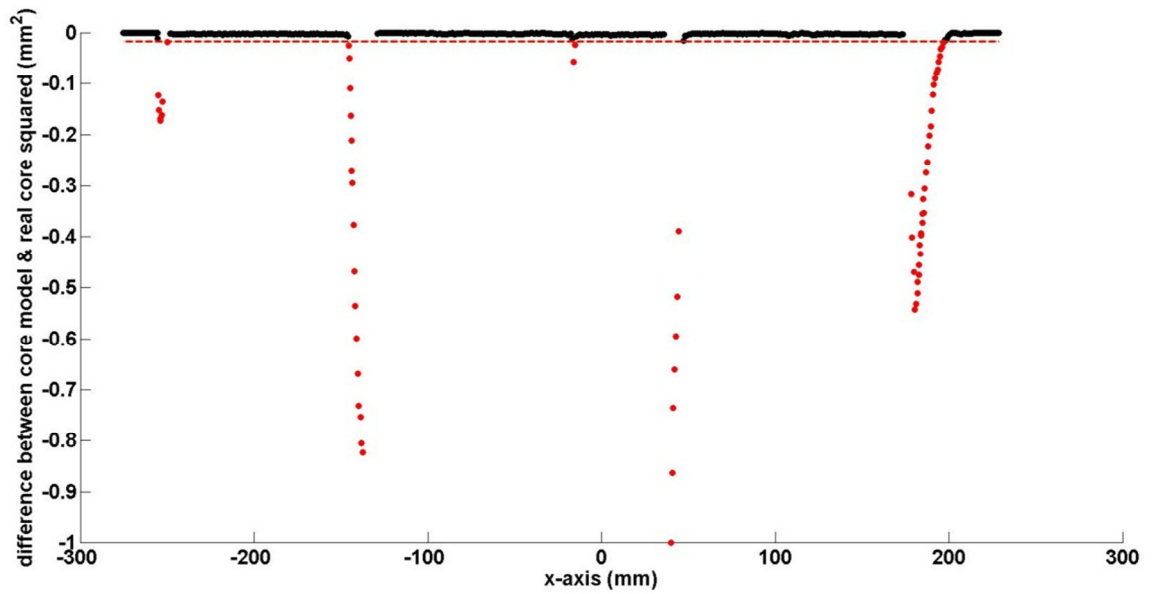


Figure 3.25: Fracture detection with the difference squared. For this example, the threshold, represented by the red dashed line, is the variance of the squared difference. The intact core data are less scattered. Two data points are detected for the tight fracture versus the single data point with the difference method (see Figure 3.24).

Method 2: Discrete Local First Derivative:

From the core profile (see Figure 3.22), it is clear a change in slope is associated with fracture zones. Because the data are discrete rather than continuous, the local derivative is taken at each point. Equation 3.3 is the formula used to compute the discrete first local derivative. It is the difference between the adjacent elements of z divided by the corresponding difference between the adjacent elements of x.

$$\frac{dz}{dx} = \frac{(z_2 - z_1)}{(x_2 - x_1)}, \frac{(z_3 - z_2)}{(x_3 - x_2)}, \dots, \frac{(z_n - z_{n-1})}{(x_n - x_{n-1})} \quad (3.3)$$

The difference between adjacent x-values can result in division by zero if two z readings are taken at the same point along x. These zeros are replaced with a very small fraction of the mean of the difference between x-values (0.001*mean). This very small number plots the coincident x-values extremely close together, rather than at the same location. The close proximity of these points is preserved and the program is able to run.

The absolute value (multiplied by negative one for visualization purposes) of the first derivative typically yields multiple peaks below the threshold at fracture locations, as illustrated in Figure 3.26. Thus, most fractures are counted more than once.

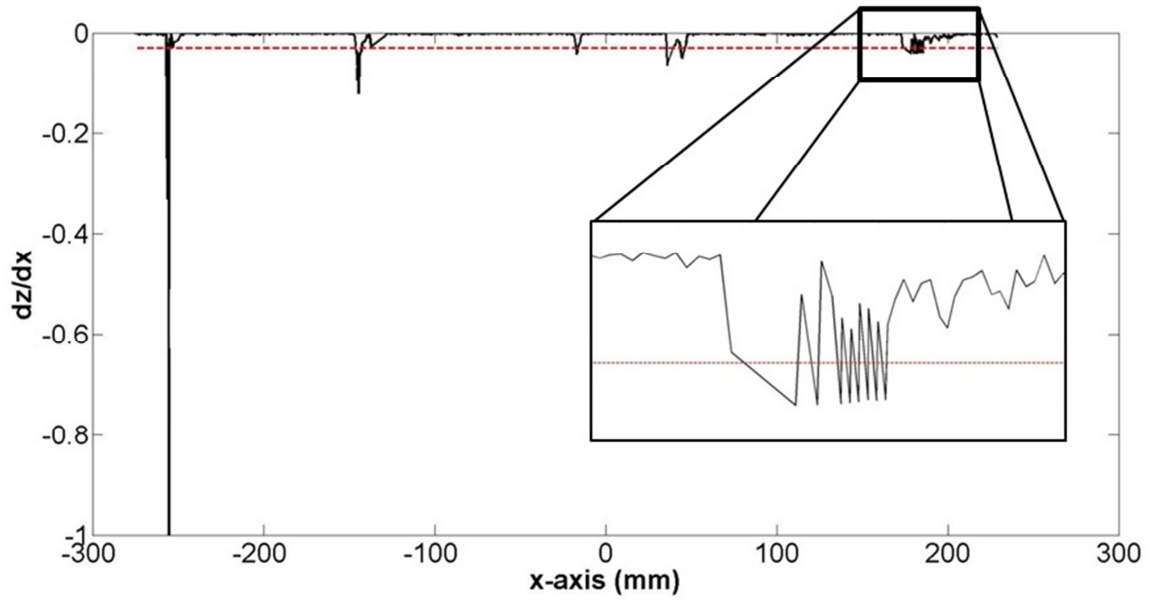


Figure 3.26: The absolute value of the first derivative (multiplied by negative one). Each peak below the threshold (red dashed line) is counted as a fracture.

The multiple peaks are removed by binning the data. The number of bins used is equal to 10% of the profile data, rounded up. For example, the profile discussed in this example is comprised of 595 xz pairs, which is equivalent to 60 bins. Therefore the bin width is approximately 10 mm. The value of each bin is the maximum value of the first derivative minus the minimum value of the first derivative (i.e. the range of the first derivative within each bin). The threshold shown in Figure 3.27 is the variance of the first derivative; all five fractures are identified.

Method 3: Detrend:

Perhaps the simplest, and most promising, method is to use the mean for the threshold. Once the trend is removed from the data, the mean is reset to a number very close to zero. All fractures contained points below the mean (see Figure 3.22). To locate fractures, all points greater than or equal to the mean are considered intact core and are re-set to zero. All points less than the mean are considered fractures, as illustrated in Figure 3.28.

To detect the fractures, a threshold is required. A dynamic threshold is favored over a fixed threshold. For profile methods 1, 2 and 3, one and two standard deviations of the difference, the variance and the root mean square error (RMSE) are tested as possible thresholds. Method 3 is also tested with the mean as a threshold. The results of these tests are presented in the next chapter.

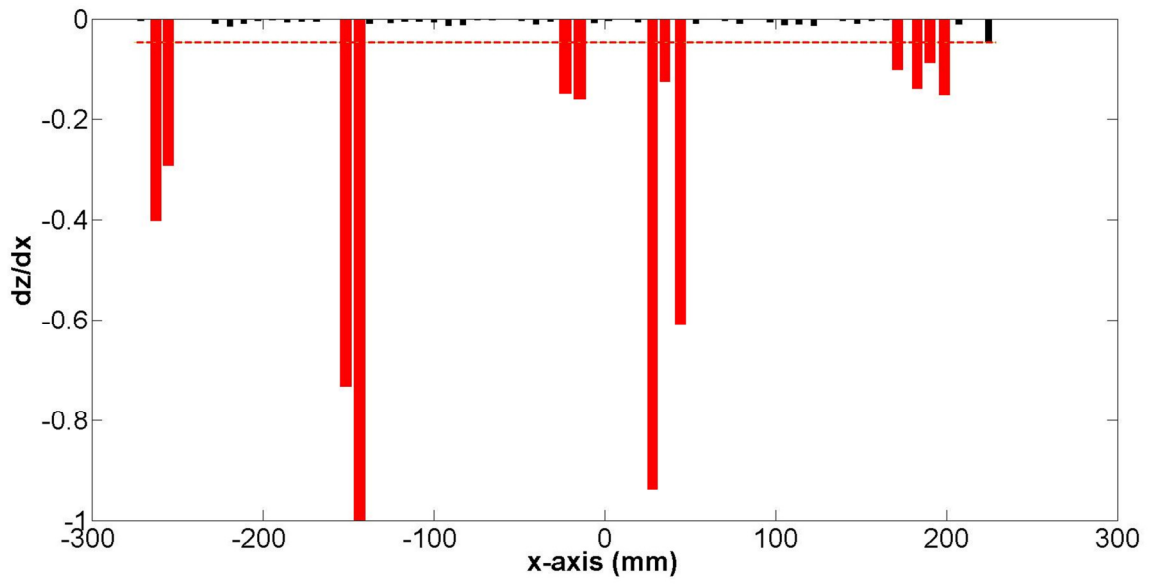


Figure 3.27: The first derivative binned. The value of each bin is the range of the first derivative. The five groups of red bins correspond to fracture zones below the threshold.

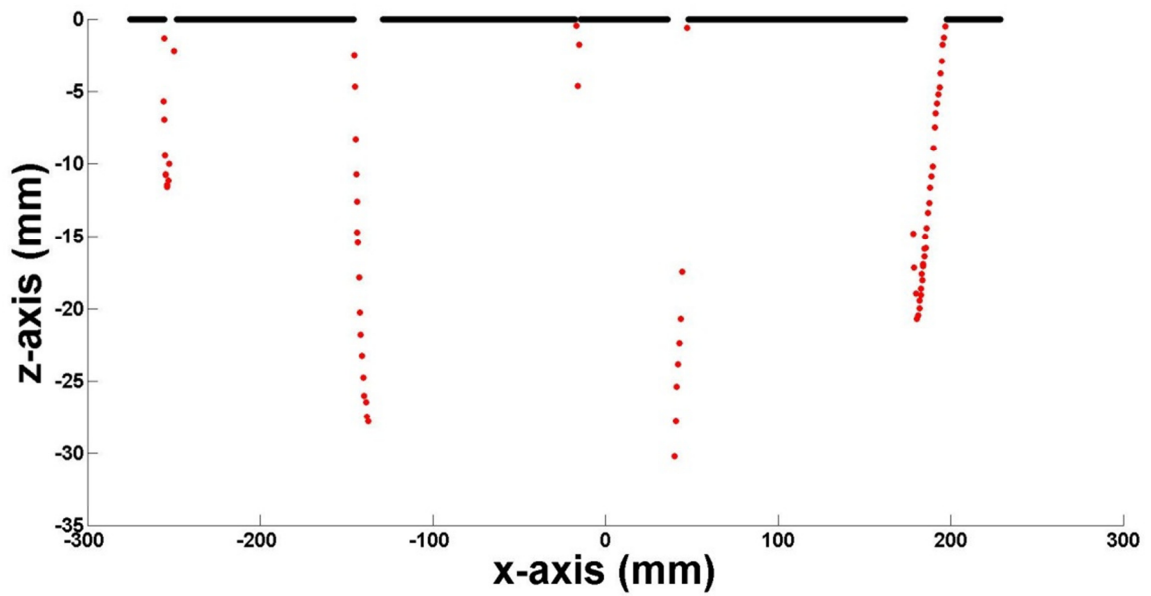


Figure 3.28: All points greater than or equal to the mean are considered intact core (black dots) and are re-set to zero. All points less than the mean are considered fractures (red dots). Three points are detected for the tight fracture versus the single point with the difference method and 2 points with single with the difference squared method (see Figures 3.24 and 3.25).

3.9 Fracture Location and RQD

Once the fractures are detected, their location and width is determined. The data identified as intact core are re-set to zero. The fracture data are re-set to one. To locate the groups of ones within the zeros (i.e. fractures between the lengths of intact core), the difference between the adjacent elements is calculated (see equation 3.4). The initial and final ones of each group are equal to 1 and -1, respectively. The value of x at these ones is determined. The initial x-values are subtracted from the final x-values to find distance between fractures. The fracture edge locations are found at the initial x-value plus one and the final x-value. See Table 3.5 for a simplified example.

$$Z_{difference} = Z_n - Z_{n-1} \quad (3.4)$$

A similar process is used to determine the length of the intact core sections with ones representing the intact core instead of zeros. The lengths of intact core greater than 10 cm are summed, divided by the length of the core run and multiplied by 100% to yield the RQD.

In fact, this is not the true RQD, as mechanical breaks have not been identified. In addition, the length of the profile is used in place of the length of the core run because the core box does not fit into a single scan. The maximum length of core able to be imaged is approximately 600 mm (the core run is 1.5 m). If the digitizer configuration were changed so the entire core box could

Table 3.5: Example of the methodology used locate fractures and to measure the distance between fracture edges. For this simple example the threshold is -1025.

x (mm)	z (mm)	Binary Intact core = 0 Fractures = 1	Fracture edge Identification Difference = $Z_n - Z_{n-1}$	Fracture edge width and location x_{start} at $z = 1$ x_{end} at $z = -1$
1	-1000	0	0	0
2	-1000	0	0	0
3	-1000	0	1	3*
4	-1050	1	0	0
5	-1050	1	0	0
6	-1050	1	0	0
7	-1050	1	-1	7
8	-1000	0	0	0
9	-1000	0	0	0
10	-1000	0	0	0
*Fracture width: $x_{end} - x_{start} = 7 - 3 = 4$				
*Fracture location: start = $3+1 = 4$; end = 7				

be captured, the point cloud concentration would be less than 1point/mm². A lower point cloud concentration would adversely impact the reliability of the fracture detection algorithms. As such, the actual value of the RQD is not meaningful; it serves only as proof-of-concept parameter. What will be tested is the consistency between the RQD calculated by the algorithm and the RQD measured by an experienced geologist, given the modifications previously mentioned. Therefore, the RQD for the purposes of this research is a “simulated” RQD.

3.10 Distance-Based Images

The distance-based images had to be created before they could be processed with established techniques. To do this, the 3-D point cloud data are converted into a matrix. In the point cloud, some values of x and y are very close together, others farther apart, a few are repeated. The xy point cloud data are adjusted to occur at equal 1 mm intervals; the number of rows is made equal to the length of y and the length of x determines the number of columns, rounded to the nearest integer. For example, if y is equal to 46.8 mm and x is equal to 97.4 mm, the number of matrix rows is 47 and the number of columns is 97. The number of cells is equal to product of the rows and columns – in this example 4,656.

The z-values populate the 1 mm² matrix cells at their respective xy coordinates. When two or more z-values belong to the same cell, their average is computed. Typically, there are a large number of z-values; too much averaging occurs and detail is lost. Therefore, the number of rows and columns is multiplied by 10 in order expand the matrix, reduce the cell size to 0.1 mm², and minimize repeat entries. For example, if the number of z-values is 138,197 for 4,656 cells, then there will be 29.7 entries per cell. By expanding the matrix, the number of z-values per cell is reduced to 0.3. If there is no z-value in the cell, one is calculated by interpolation. The result is a matrix of distance values, as shown in Table 3.6.

Table 3.6: A portion of a 470 × 970 matrix comprised of distance measurements. The orange cells are the fracture edge. The number of decimal places shown in this figure does not reflect the accuracy. Extra decimal places are included to illustrate the difference between the values.

Row/Column	848	849	850	851	852	853	854	855
194	-573.047	-573.047	-573.047	-573.047	-573.047	-573.047	-573.047	-573.047
195	-573.047	-573.047	-573.047	-573.047	-573.047	-573.047	-573.047	-573.047
196	-573.047	-573.047	-573.047	-573.047	-573.047	-573.047	-573.047	-573.047
197	-573.047	-573.047	-573.047	-573.047	-573.047	-573.047	-573.047	-543.964
198	-573.047	-573.047	-573.047	-573.047	-573.047	-573.047	-543.964	-543.964
199	-573.047	-573.047	-573.047	-573.047	-543.964	-543.964	-543.964	-543.964
200	-573.047	-573.047	-573.047	-543.964	-543.964	-543.964	-543.964	-543.964
201	-573.047	-543.919	-543.964	-543.964	-543.964	-543.964	-543.964	-543.964
202	-543.919	-543.919	-543.964	-543.964	-543.964	-543.964	-543.964	-543.964
203	-543.919	-543.964	-543.964	-543.964	-543.964	-543.964	-543.964	-543.964
204	-543.919	-543.964	-543.964	-543.964	-543.964	-543.964	-543.964	-543.964
205	-543.964	-543.964	-543.964	-543.964	-543.964	-543.964	-543.964	-543.964

The established edge and line detection methods available in the MATLAB image processing toolbox are designed for digital photographs. Therefore, the matrix must be converted to grey-scale intensity values. This conversion is done with the MATLAB image processing tool “mat2gray”. As shown in Table 3.7, the intensity values are numbers between zero and one, where 0 is black, 1 is white. The difference between these images and a digital photograph is the fact that the intensity values are derived from distance measurements, not highlights and shadows. As illustrated in Figure 3.29, the rock texture is eliminated in the distance-based image.

Table 3.7: A portion of a 470 × 970 matrix comprised of grey-scale intensity values. These intensity values have been converted from distance measurements. The orange cells are the fracture edge. The number of decimal places shown in this figure does not reflect the accuracy. Extra decimal places are included to show the difference between the values.

Row /Column	848	849	850	851	852	853	854	855
194	0.0015616	0.0015616	0.0015616	0.0015616	0.0015616	0.0015616	0.0015616	0.0015616
195	0.0015616	0.0015616	0.0015616	0.0015616	0.0015616	0.0015616	0.0015616	0.0015616
196	0.0015616	0.0015616	0.0015616	0.0015616	0.0015616	0.0015616	0.0015616	0.0015616
197	0.0015616	0.0015616	0.0015616	0.0015616	0.0015616	0.0015616	0.0015616	0.8749512
198	0.0015616	0.0015616	0.0015616	0.0015616	0.0015616	0.0015616	0.8749512	0.8749512
199	0.0015616	0.0015616	0.0015616	0.0015616	0.8749512	0.8749512	0.8749512	0.8749512
200	0.0015616	0.0015616	0.0015616	0.8749512	0.8749512	0.8749512	0.8749512	0.8749512
201	0.0015616	0.8763026	0.8749512	0.8749512	0.8749512	0.8749512	0.8749512	0.8749512
202	0.8763026	0.8763026	0.8749512	0.8749512	0.8749512	0.8749512	0.8749512	0.8749512
203	0.8763026	0.8749512	0.8749512	0.8749512	0.8749512	0.8749512	0.8749512	0.8749512
204	0.8763026	0.8749512	0.8749512	0.8749512	0.8749512	0.8749512	0.8749512	0.8749512
205	0.8749512	0.8749512	0.8749512	0.8749512	0.8749512	0.8749512	0.8749512	0.8749512

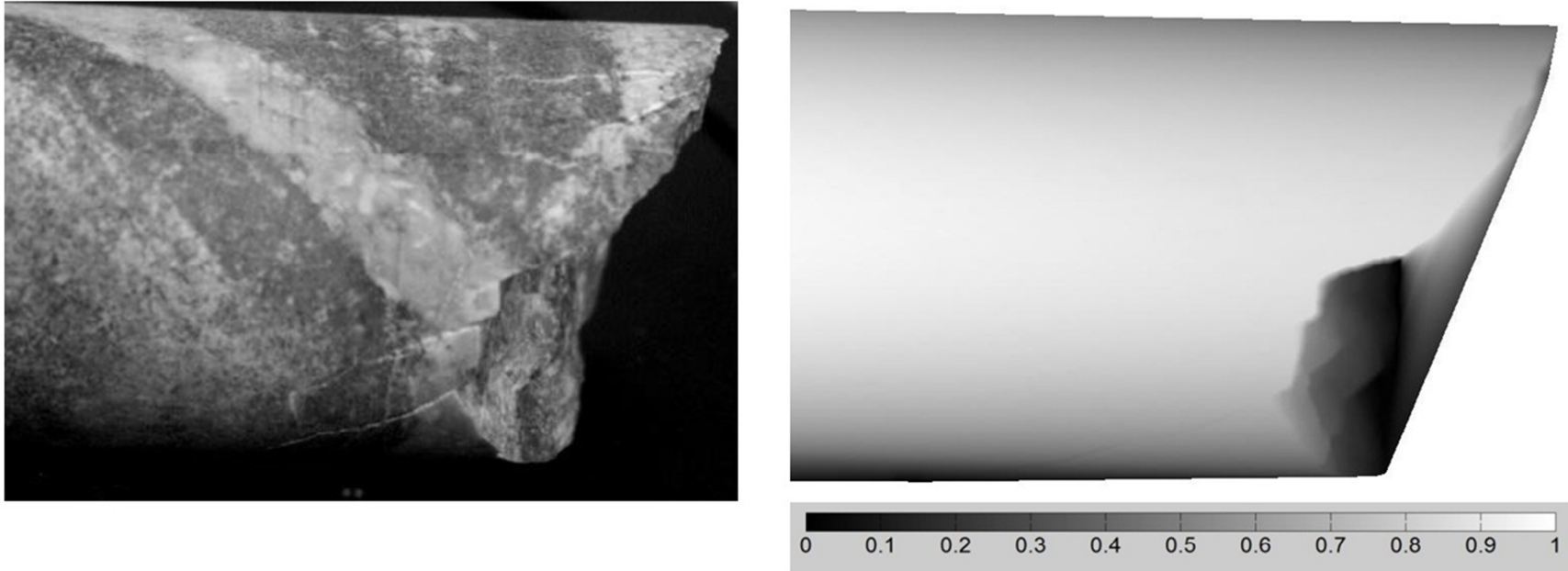


Figure 3.29: The image on the left is a black and white digital photograph of a core sample. The core diameter is 47.6 mm. The rock texture reduces the reliability of established edge and line detection tools. The image on the right is generated with 3-D data. Note that the rock texture is not visible in the distance-based image. The scale bar represents the grey level where 0 is black and 1 is white.

3.11 Fracture Characterization

The distance-based images are used for fracture characterization. As mentioned previously, a high point cloud concentration is needed to distinguish between natural and mechanical breaks. To obtain this high concentration, the core must be scanned on the turntable, at closer range, with the tele-lens. Because the digitizer configuration is different, and lens must be changed, it is not practical to integrate the fracture characterization scans into the core box fracture detection and RQD algorithms.

In order to develop a fracture characterization algorithm that *could* eventually be integrated with the core box algorithms, the fracture trace is imaged instead of the entire breakage surface. Although the breakage surface can be readily captured on the turntable, it is typically not visible or imaged well when scanned in the core box. In the core box, only the fracture trace is clearly visible. Thus, the data available for characterization are the angle and roughness of the trace. The fracture trace may be a line or curve, as illustrated in Figure 3.30. Because the breakage surface is not visible, the state of weathering or alteration on the breakage surface cannot be used to assess the origin of the fracture.

The fracture trace is detected by a similar process to the centerline profiles. Rather than using one profile line along the axis of the core, each row of the matrix serves as a “profile”, as shown in Figure 3.31. The profiles are 0.1 mm

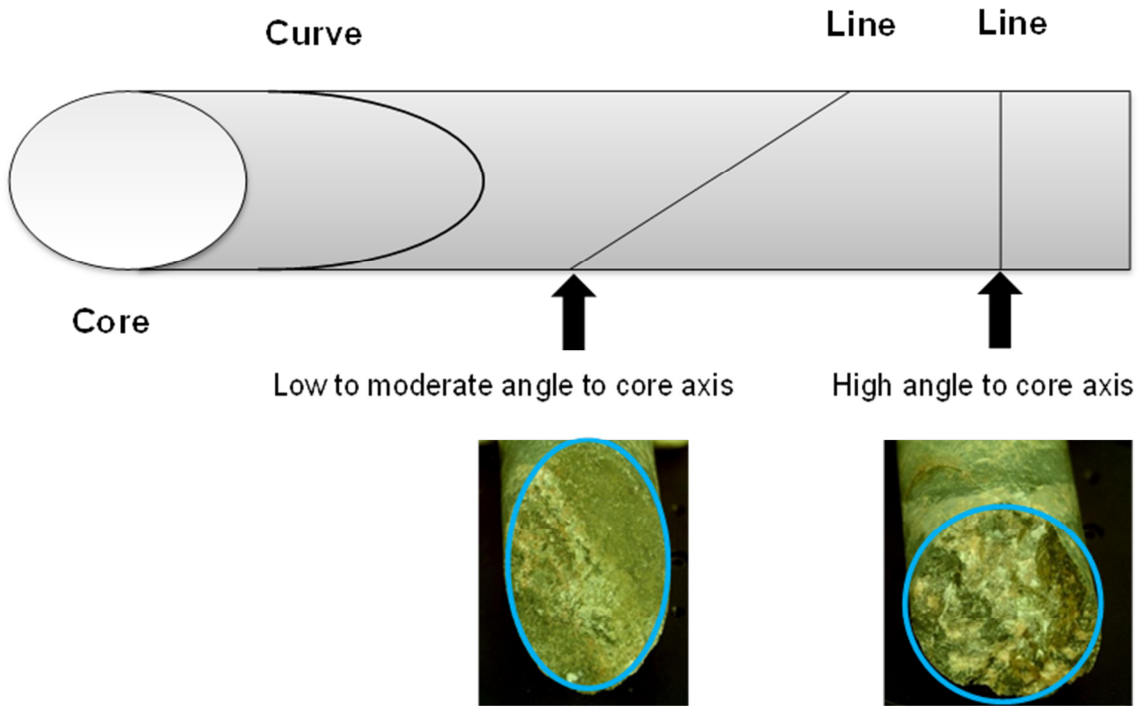


Figure 3.30: Natural fractures tend to have a breakage surface at a low to moderate angle to the long axis of the core. An ellipse can be fit to these surfaces. If the ellipse is viewed edge-on, it corresponds to a low to moderate angle line or a curve. Mechanical breaks tend to have a breakage surface at high angle to the horizontal. A circle can be fit to these surfaces. If the circle is viewed edge-on, it corresponds to a high angle line.

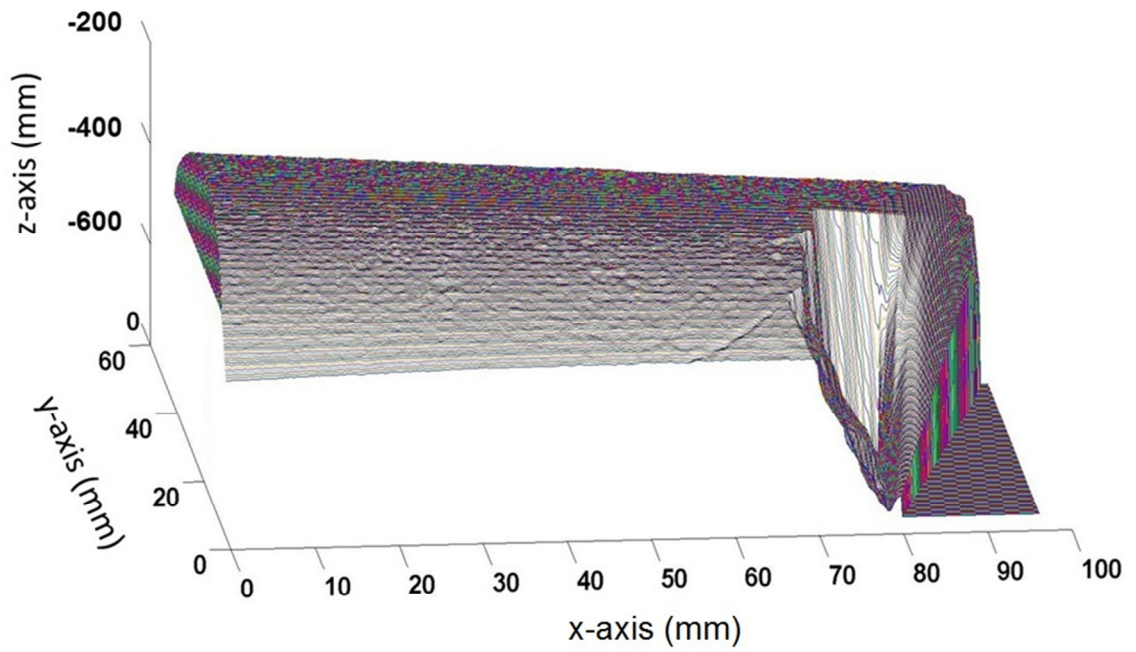


Figure 3.31: Parallel profiles capture the fracture trace. In this example, there are 360 profiles. Profile spacing is 0.1 mm.

apart. The standard deviation of the grey-level is the threshold. After the threshold is applied, the intact core is reset to zero, the fracture trace one, as shown in Table 3.8. The xy coordinates of the trace are extracted from the file and plotted. This process is illustrated in Figure 3.32.

As shown in Figure 3.33, the algorithm decides whether the trace is linear or curved. If the trace is curved, then the value of x at the median of y will either be greater than, or less than, the value of x at the initial y and final y. In other words, on the x-axis, the peak of the curve is always greater than or less than the end points of the curve. If the trace is linear, then the value of x at the initial y is either equal to, greater than, or less than, both the value of x at the median of y and final y. In other words, on the x-axis, the middle of the line is always a value between the end points of the line. A linear natural fracture trace and a linear mechanical break trace are shown in Figure 3.34.

Table 3.8: A portion of a 470 × 970 matrix comprised of binary values used to extract the fracture trace for characterization. The fracture trace is represented by the ones, the intact core by zeros.

Row/Column	848	849	850	851	852	853	854	855
194	0	0	0	0	0	0	0	0
195	0	0	0	0	0	0	0	0
196	0	0	0	0	0	0	0	0
197	0	0	0	0	0	0	0	1
198	0	0	0	0	0	0	1	0
199	0	0	0	0	1	1	0	0
200	0	0	0	1	0	0	0	0
201	0	1	1	0	0	0	0	0
202	1	0	0	0	0	0	0	0
203	0	0	0	0	0	0	0	0
204	0	0	0	0	0	0	0	0
205	0	0	0	0	0	0	0	0

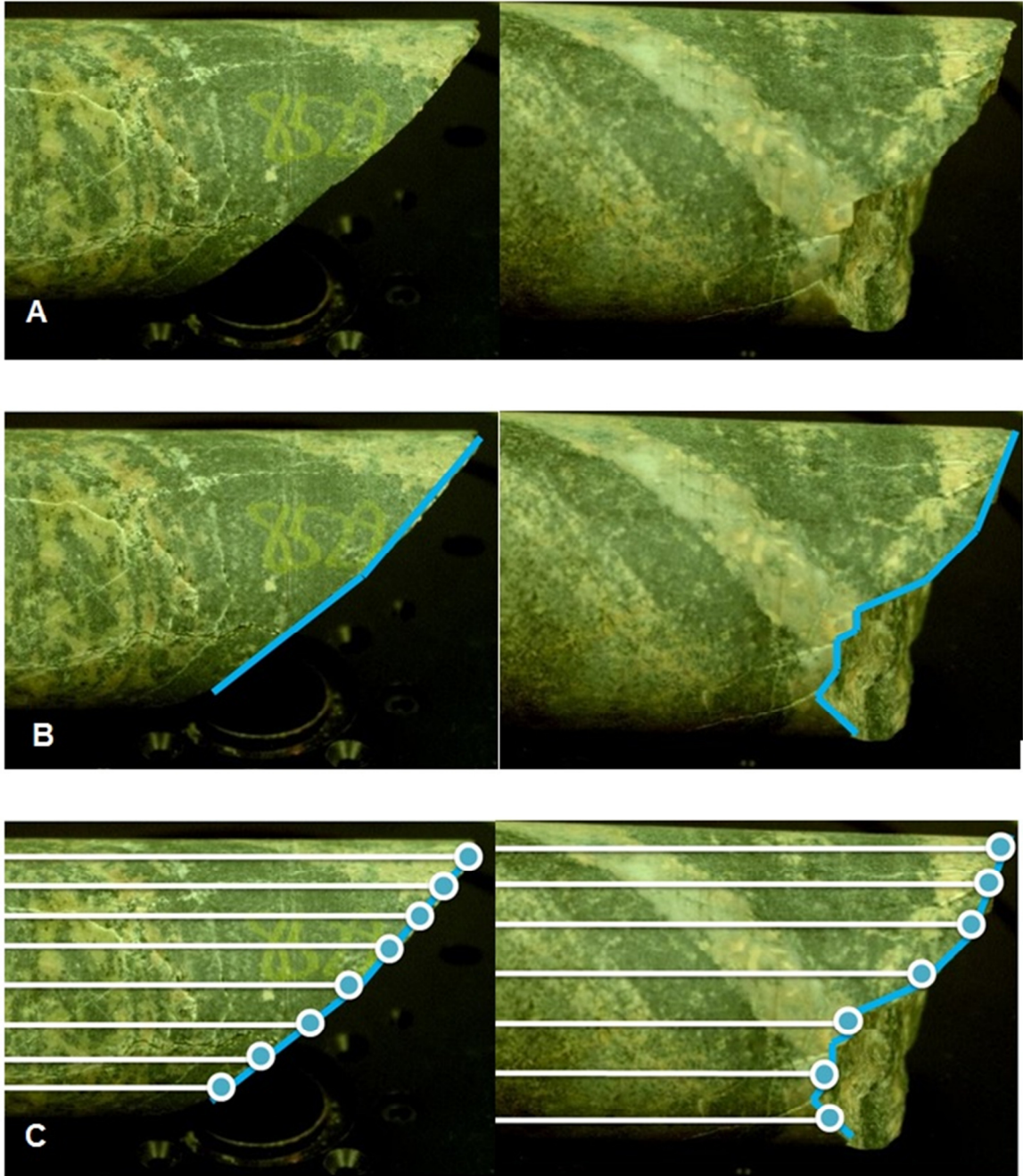


Figure 3.32: Fracture trace detection. (A) Natural fracture (left) and mechanical break (right). (B) Blue lines are the fracture traces to be detected. (C) Parallel profiles and the points intersecting the trace. The core diameter is 47.6 mm.

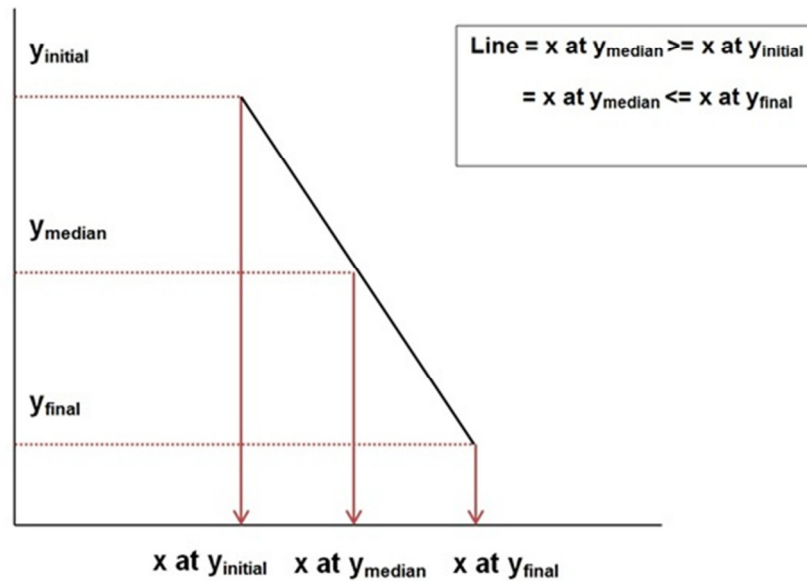
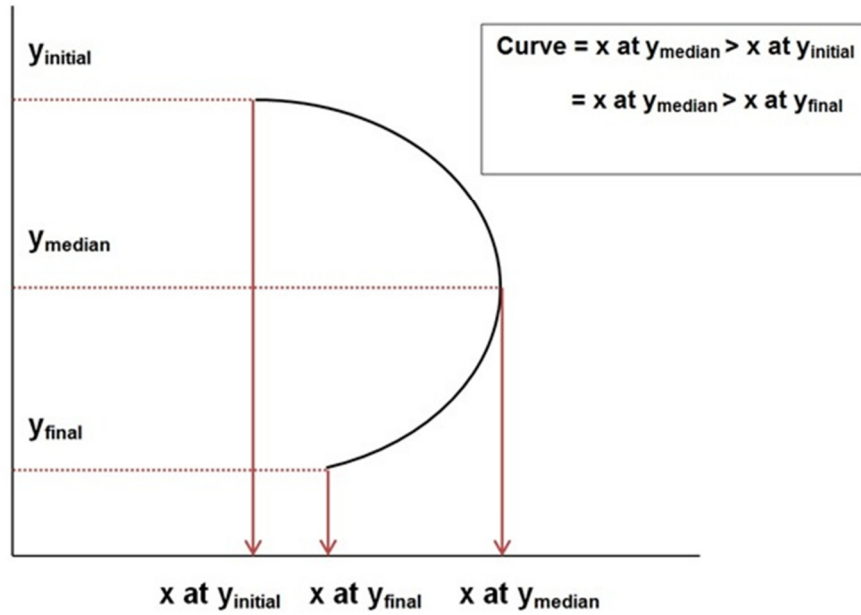


Figure 3.33: The fracture characterization algorithm decides whether the fracture trace is a curve (top) or line (bottom). If the trace is a curve, the middle of the curve will be greater than (shown), or less than, the end points of the curve with respect to the x-axis. If the trace is linear, the initial point will either be equal to, greater than, or less than (shown) the middle and final points with respect to the x-axis.

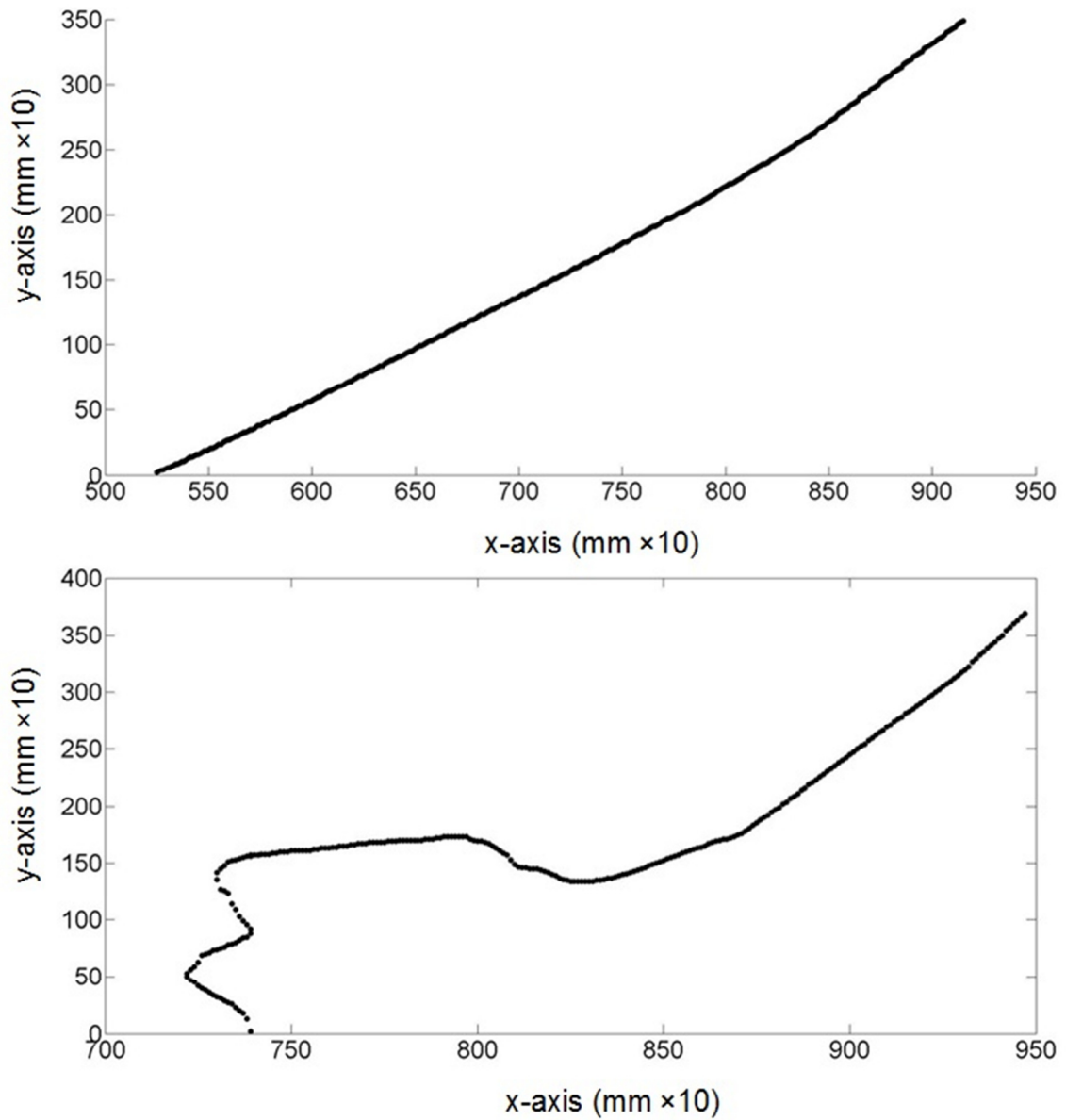


Figure 3.34: Natural fracture trace (top) and mechanical break trace (bottom). The natural fracture trace is very linear, which reflects the smooth fracture edge. The mechanical break has an irregular shape, which indicates the edge of the break is rough.

Two characterization parameters can be derived from the fracture trace; the angle of the trace with respect to long axis of the core (i.e. horizontal or $\theta =$ zero) and the roughness of the trace. The angle of the best fit line through the points serves as the angle of the trace. The roughness of the trace is quantified by two methods.

The first method is based on the vertical difference between the trace points and the best fit line – the residuals. Shown in Figure 3.35, if the fracture trace is curved, a sine wave is fit to the data instead of a straight line. As illustrated in Figure 3.36, if the trace is smooth, the data will fit the line well and the residuals are small. The residuals are much larger if the trace is rough.

The second method measures the angle between each trace point and horizontal. For a smooth trace, the angles will be similar to each other. A rough trace will be comprised of many angles. Figure 3.37 is a comparison between the natural fracture trace (smooth) and the mechanical break trace (rough) presented in Figure 3.34. For both methods, the standard deviation is used as the roughness threshold.

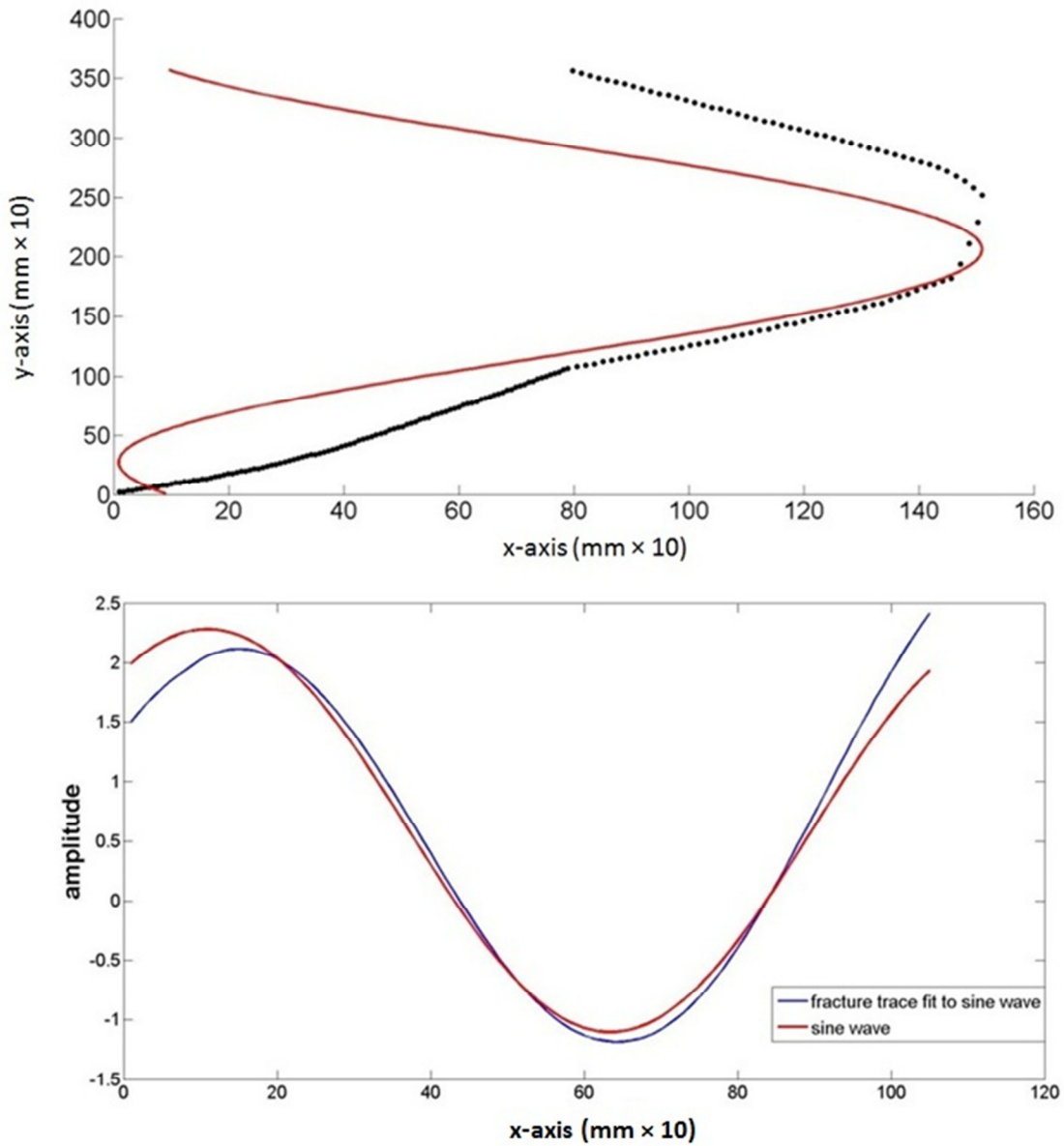


Figure 3.35: Curved fracture trace compared to sine wave by two methods. Top: Curved fracture trace (black dots) plotted with sine wave (red) with same amplitude and position on the y-axis. Bottom: Curved fracture trace data (blue) fit to sine wave (red) with the same amplitude and range of x-values.

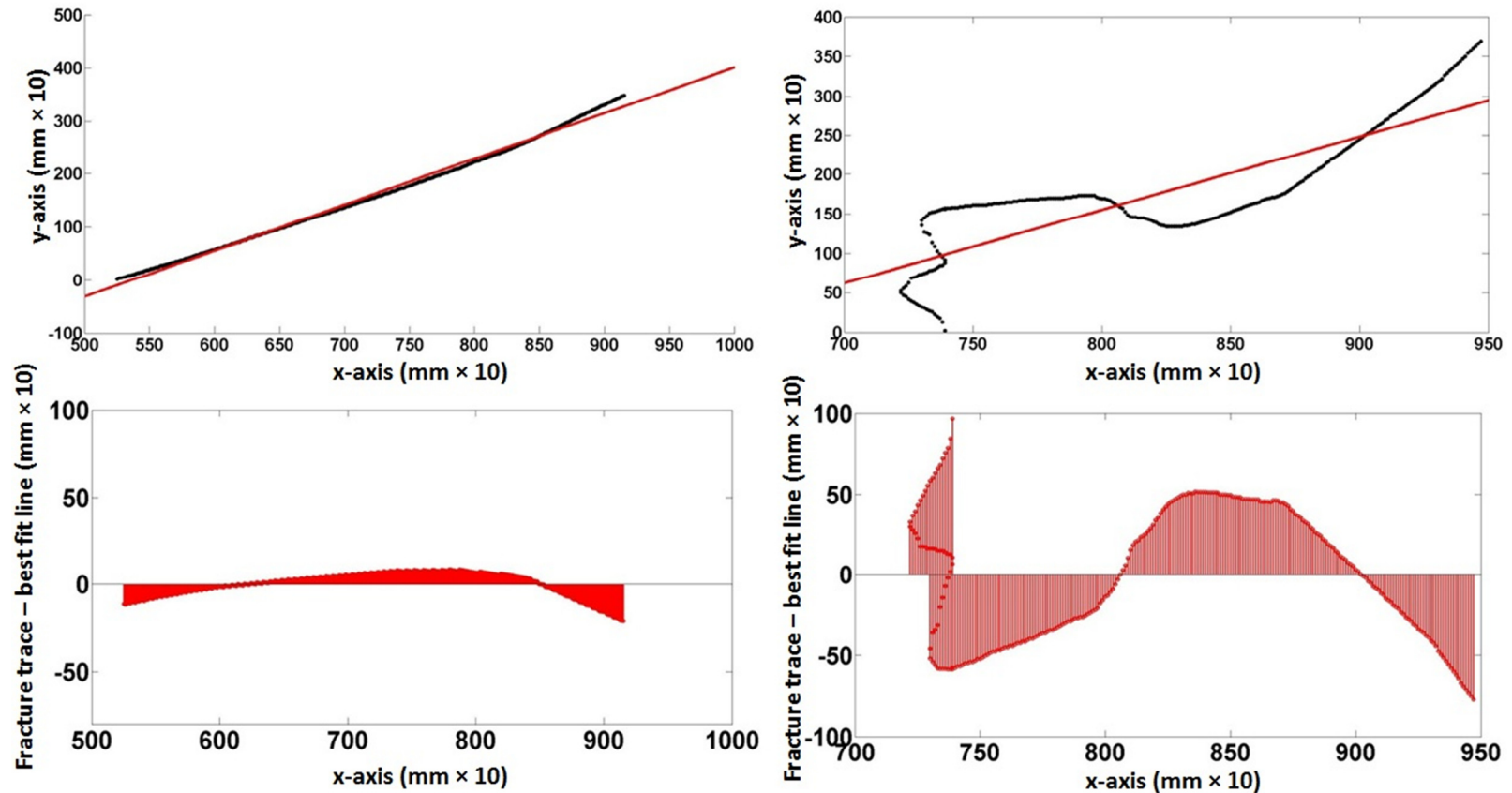


Figure 3.36: Linear fracture trace with best fit line. Natural fracture trace (top left) and mechanical break trace (top right) with best fit line shown in red. The line fits the points of the natural fracture well compared to the mechanical break. Below are the residuals – the vertical difference between the trace points and the best fit line. The standard deviation of the residuals is 7.3 and 40.2 mm for the natural fracture and mechanical break, respectively.

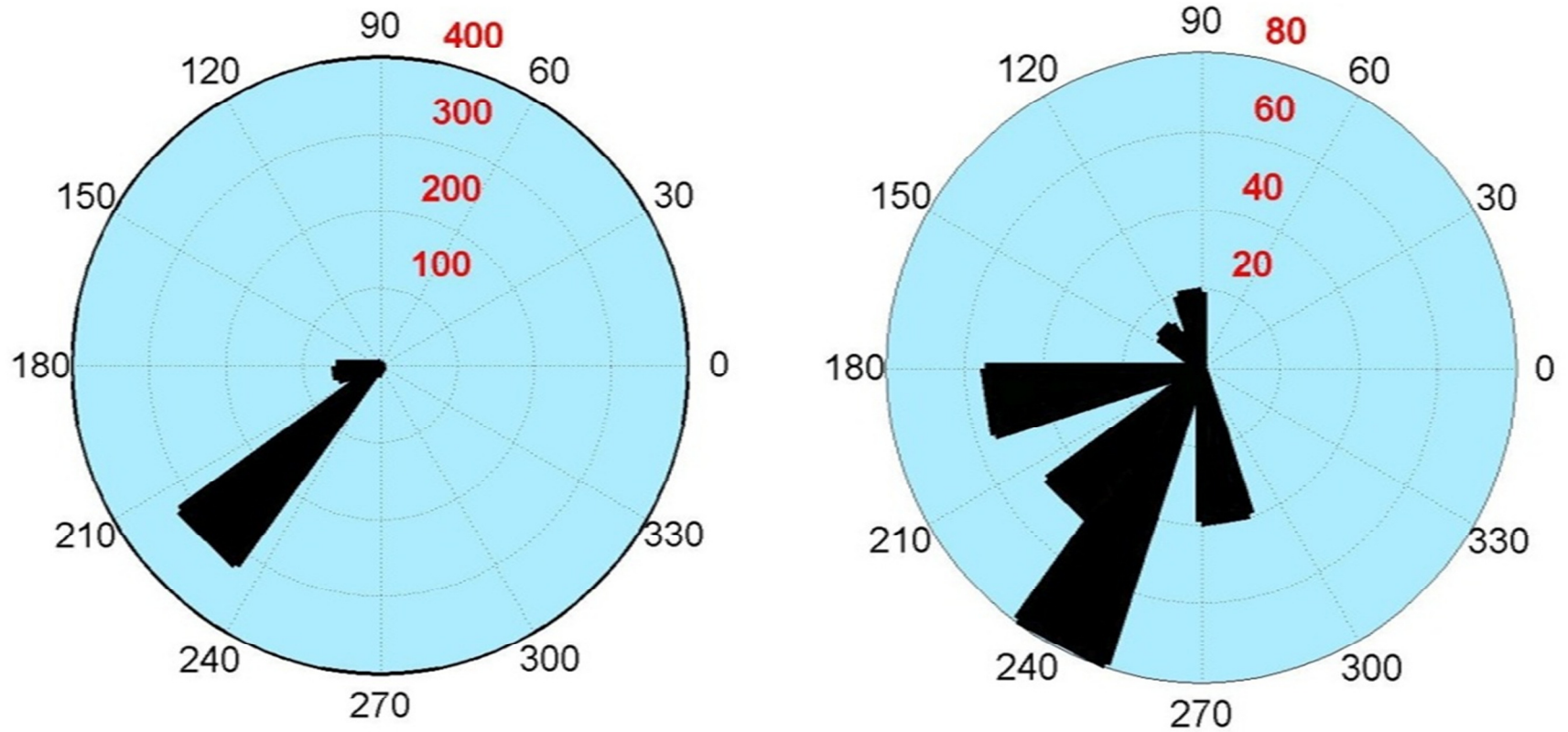


Figure 3.37: Rose diagrams (i.e. a histogram of angles) for the natural fracture (left) and the mechanical break (right). The natural fracture trace is comprised of points which are at similar angles to the horizontal. There are over 300 points in the $\sim 215^\circ$ to $\sim 235^\circ$ bin. There is a smaller bin of less than 50 entries between $\sim 180^\circ$ and $\sim 200^\circ$. The mechanical break trace has several bins representing a wide range of angles from $\sim 90^\circ$ to $\sim 290^\circ$. The largest has 80 entries from $\sim 240^\circ$ to $\sim 255^\circ$.

3.10: 3-D Core Models

As discussed in the previous sections of this chapter, the cores were scanned on the turntable, every 20°, from three orthogonal orientations, for a total of 54 images per sample. The number of images used to assemble the models is far less; ranging from 7 to 11 images per model. It is necessary to acquire a large number of images from various viewpoints because only some of the images will contain usable common features.

Much like fitting puzzle pieces together, assembling core models requires at least 1 common feature between adjacent overlapping images. The common feature should be *distinctive* – for example, a linear feature (e.g. ridge line), a protrusion (e.g. large mineral grain) or a depression (e.g. a chip) – to help orient the individual images with respect to one another. The assembly process is shown in Figures 3.38 and 3.39. When a common feature (or features) is identified, it is manually selected on both images by the operator. The PolyWorks software then aligns these images. This process is repeated until the surface of core is complete; the core model can be rotated and visualized from any angle without any missing sections. At this stage, the overlap between the images is removed and the images are merged to form a meshed model covered by a single continuous surface. Finally, any small holes in the model are filled and minor artifacts in the mesh are trimmed, as shown in Figure 3.40.

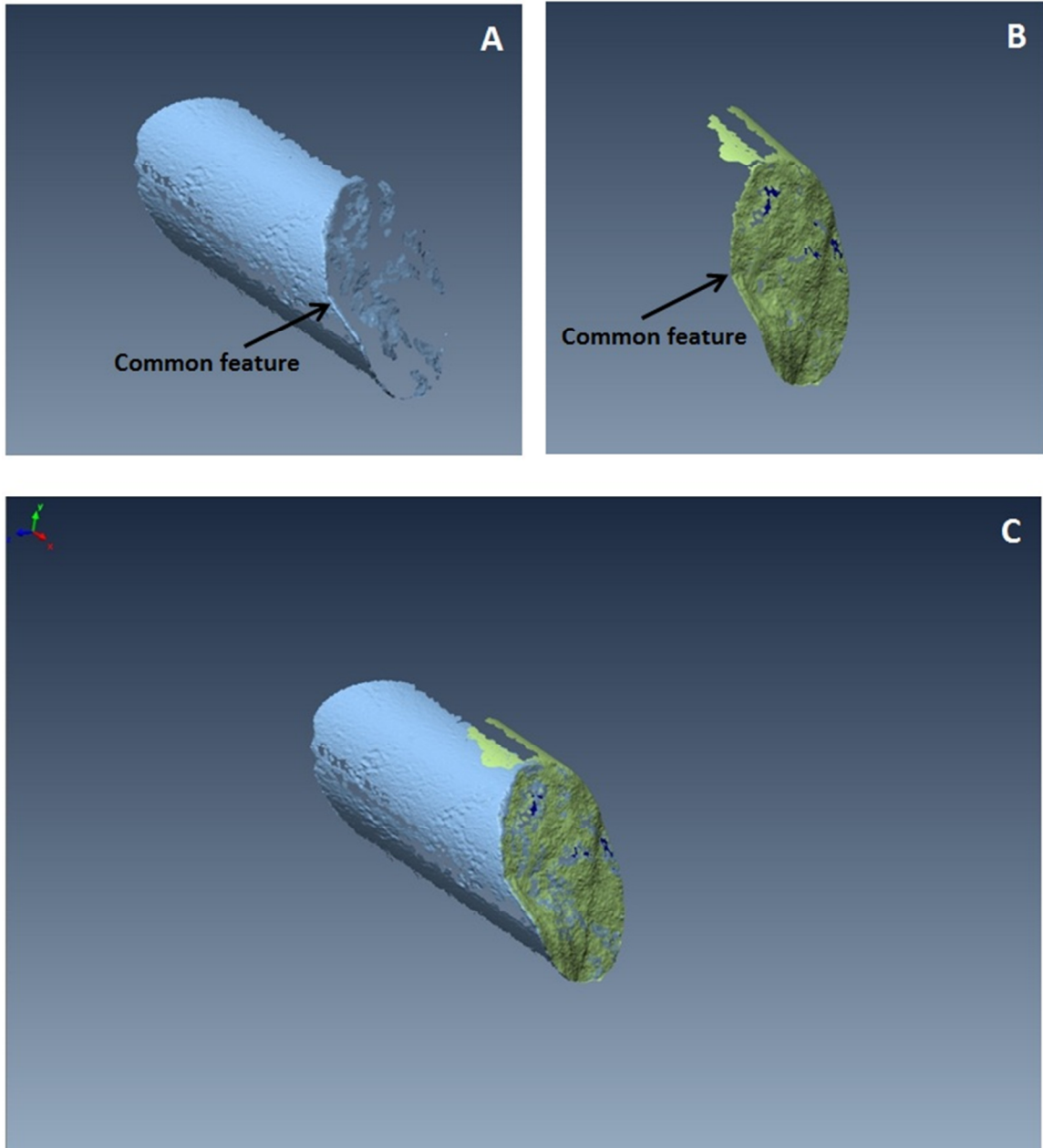


Figure 3.38: Core image acquired at an angle of incidence of 40° (A). Core image acquired at an angle of incidence of 100° (B). A common feature is identified on both A and B – a sharp change in slope along the fracture edge. Images A and B are aligned (C). Core diameter is 47.6 mm.

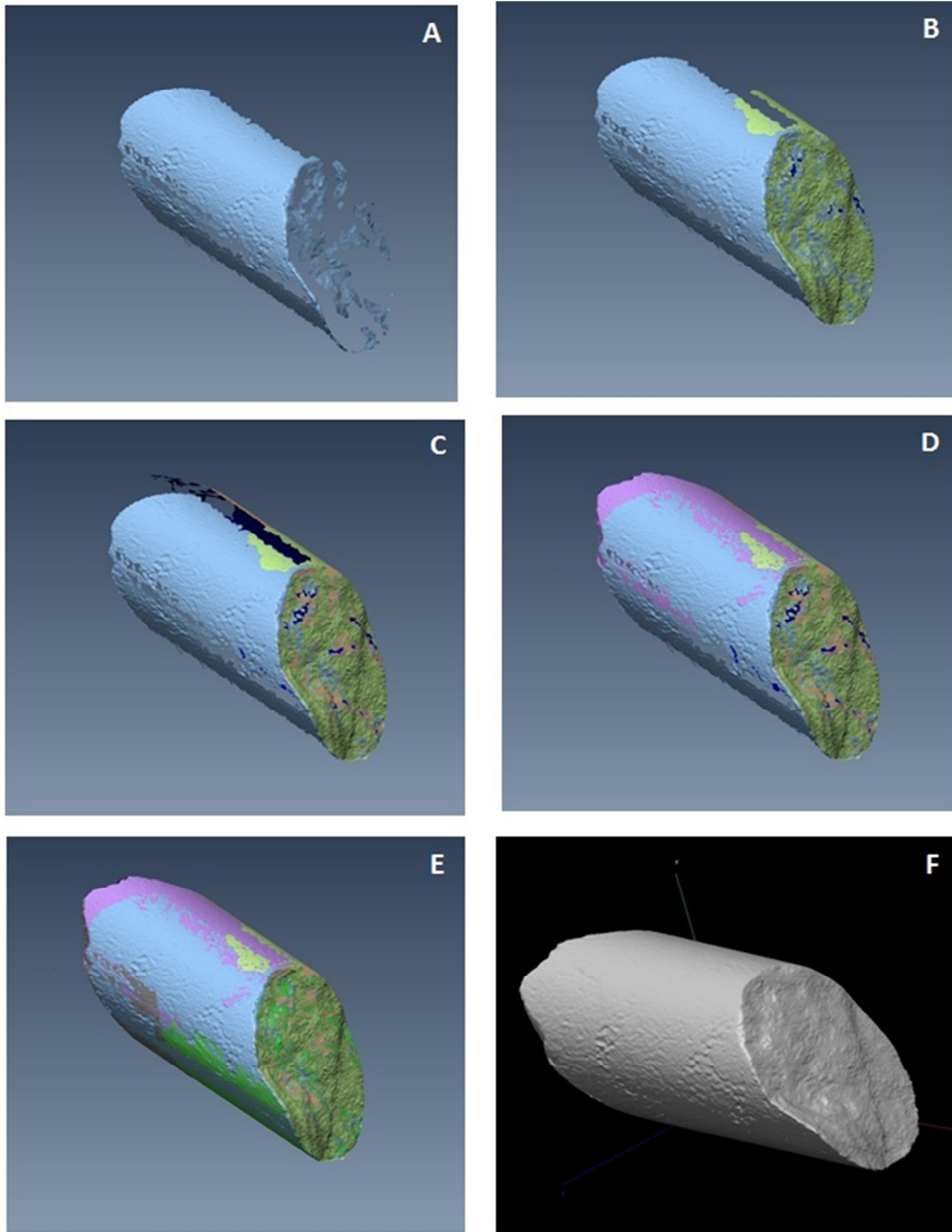


Figure 3.39: The alignment process is shown in images A through E. Image F is the final core model. The various colours correspond to points selected from different images.

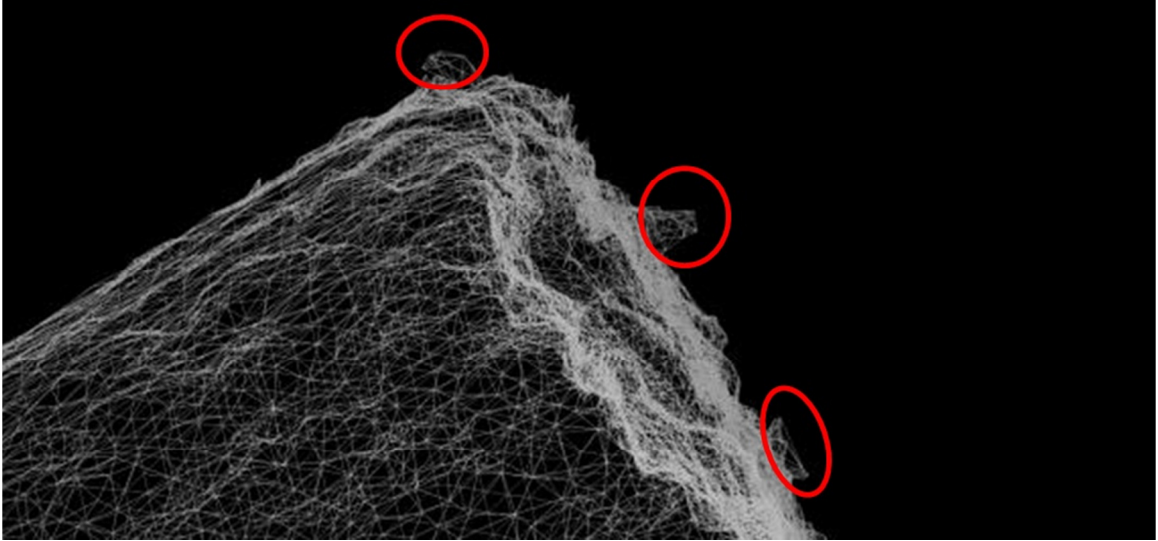


Figure 3.40: Close-up image of a core model in mesh view. The areas circled in red are artifacts that need to be edited out manually.

Acquiring the scans for all three cores took approximately five hours. To align, merge, fill and manually edit each core model took approximately four to five hours per model. Therefore, each model represents a minimum of one day of work.

Once the core model is complete the software can calculate the volume. If the mass is measured then the density of the sample can also be determined.

It should be noted that regular 3-D shapes with smooth surfaces, sharp edges and few distinguishing features – cubes, pyramids, cylinders, etc. – are difficult to model. Cores are cylindrical. As such, the more the core sample approaches this shape, the more extreme the modeling challenge will be.

4. Evaluation and Results

4.1 Overview

Presented in this section is an evaluation of the fracture identification, simulated RQD and fracture characterization algorithms. The performance of the algorithms is assessed against manual measurements, which are referred to as “observed” values. Terms such as “detected” or “measured” refer to values calculated by the algorithms.

A comparison of the performance of feature detection tools on digital photographs and distance-based images is also shown. Finally, the three core models will be described and assessed.

4.2 Profile Methods

As described in section 3.7 there are 36 profiles. The profiles are identified as profiles 1 through 36. Each of the three profile methods was tested with four different thresholds. The detrend method had an additional threshold. Therefore, 468 profile tests were conducted.

The reliability of each profile method is determined by the difference between the number of fractures observed manually and the number of fractures detected by the algorithms. The ideal outcome is zero difference – all fractures detected. Figure 4.1 is an example of one of the bar graphs used to compare the number of fractures observed to the number of fractures detected.

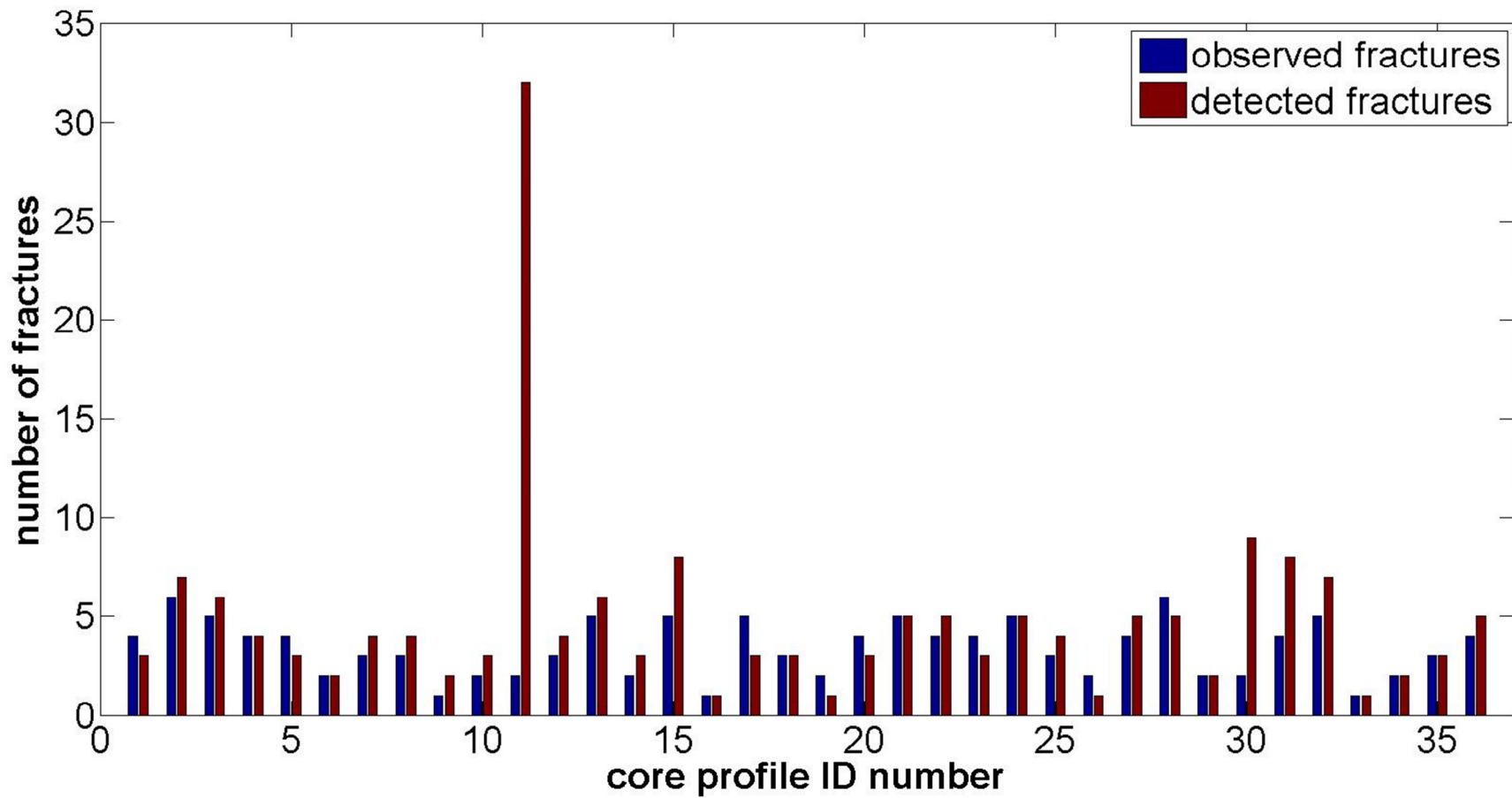


Figure 4.1: Comparison of the number of fractures observed and the number of fractures detected by the algorithm. The method used in this example is “detrend” with the threshold equal to the mean.

At least two comments can be made about Figure 4.1. First, most of the bars are not equal, which means that the algorithm is either detecting more, or detecting less fractures than observed. To determine whether the threshold is too high or too low, the number of observed fractures is subtracted from the number of detected fractures. In addition, the mean, median, mode and standard deviation of the difference are close to zero which suggests that the algorithm is detecting the correct number of fractures reliably. Shown in Figure 4.2 is the difference between the detected and observed fractures presented in Figure 4.1. Figure 4.3 is a pie chart of the percentage of detected fractures equal to, or more or less than the number of observed fractures. Table 4.1 is a summary of these percentages for all the profile methods and thresholds tested. As shown in Figures 4.2 and 4.3, the number of fractures detected is too high. A positive mean of 1.4, mode of 1.0, median of 0.5 and a standard deviation of 5.2 also indicate that more fractures were detected than observed. These basic statistics are presented in Table 4.2 and for the other profile methods and thresholds as well.

The second comment relates to the discrepant results for core profile 11, for which the number of fractures detected is 33 compared to 2 observed. This core has 2 very tight fractures. The points that represent these fractures in the profile are very close to the intact core surface. As such many points on the intact surface are above the threshold and are counted as fractures. Profiles such as these require a much lower threshold.

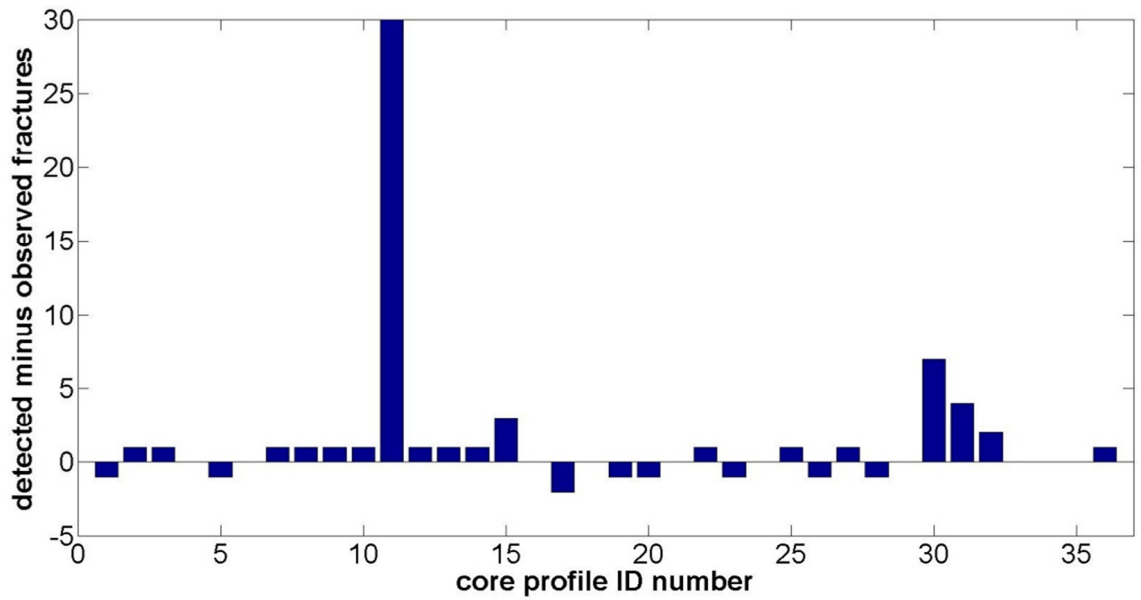


Figure 4.2: The number of fractures detected minus the number of fractures observed. The mean, median and mode of this difference are 1.4, 1.0 and 1.0, respectively. The standard deviation is 5.2. These observations suggest the number of fractures detected is too high.

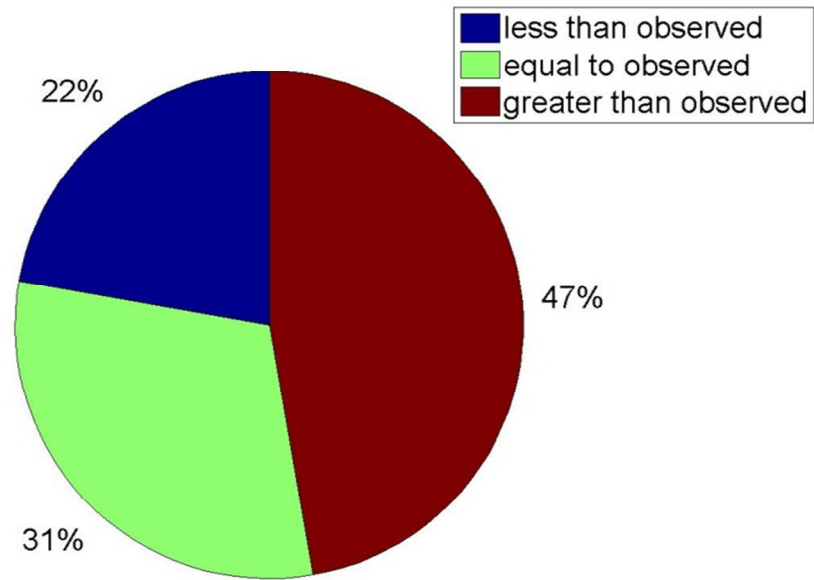


Figure 4.3: The percentage of fractures detected is 31% and is shown in green. The largest wedge is 47% and is shown in red; this indicates that the algorithm is systematically detecting more fractures than are observed.

Table 4.1: A summary of the percentage of fractures detected for each profile method and threshold. The detrend method with the variance as a threshold performed best.

Method	Threshold	Less than observed (%)	Equal to observed (%)	More than observed (%)
Detrend	Mean	22	31	47
	RMSE	58	33	8
	Standard deviation × 1	36	39	25
	Standard deviation × 2	64	25	11
	Variance	47	44	8
First derivative	RMSE	11	25	64
	Standard deviation × 1	36	28	36
	Standard deviation × 2	61	28	11
	Variance	6	11	83
Core profile model	RMSE	44	31	25
	Standard deviation × 1	47	22	31
	Standard deviation × 2	58	25	17
	Variance	19	28	53

Table 4.2: A summary of the mean, median, mode and standard deviation of the difference between the number of fractures detected and the number of fractures observed. The first derivative method with a threshold of twice the standard deviation tended to systematically under-detect fractures, whereas the variance threshold for the same method over-detected fractures. The detrend method with the variance as a threshold performed best.

Method	Threshold	Mean	Median	Mode	Standard deviation *
Detrend	Mean	1.4	0.5	1.0	1.2
	RMSE	0.3	-1.0	-1.0	1.7
	Standard deviation × 1	0.9	0.0	0.0	1.7
	Standard deviation × 2	-0.9	-1.0	-1.0	1.7
	Variance	0.5	0.0	0.0	1.7
First derivative	RMSE	1.8	1.0	0.0	2.4
	Standard deviation × 1	0.1	0.0	0.0	1.6
	Standard deviation × 2	-1.0	-1.0	-1.0	1.5
	Variance	2.9	2.0	2.0	3
Core profile model	RMSE	2.1	0.0	0.0	5.5
	Standard deviation × 1	2.5	0.0	0.0	8.3
	Standard deviation × 2	0.8	-1.0	-1.0	4.3
	Variance	2.9	2.0	2.0	3.0
*Tight and no fracture profiles removed					

Therefore, sections of core which had only tight fractures or no fractures were removed from the analysis at this stage. Once this profile was removed the standard deviation decreased from 5.2 to 1.2.

Based on the results presented in Tables 4.1 and 4.2 it is clear that none of the methods are very reliable. The most reliable is the detrend method with the variance as the threshold which correctly detected 44% of the fractures. However, this method also detected 47% less fractures than are observed. Part of the reason is that the digitizer did not image many of the tight fractures (fractures with a gap of less than 1mm) observed. It was predicted in the previous chapter that tight fractures would not be reliably imaged or detected. A few of the tight fractures are imaged by the digitizer, however they contain a small number of points; these points are typically very close to the core axis which means they are difficult to detect (recall Figure 3.14 from chapter 3).

Furthermore, if a fracture contains points below the threshold, punctuated by points above the threshold, then it is detected more than once. This is an issue for open fractures with fragments of core (rubble) in the gap and core segments with debris lodged underneath. Binning the data minimized this problem.

The results of the 468 profile tests and the conclusions made about the data are used to improve the algorithm with the following changes:

- Tight (gap < 1mm) fractures are not counted when manually observing core;
- Profiles with only tight fractures or no fractures are identified based on the difference between the maximum and minimum value of z. If this difference is less than 20% of the core diameter, the core likely contains no fractures or only tight fractures;
- Tight fracture and no fracture profiles use three standard deviations as a threshold;
- The data are binned by the method described in section 3.8;
- Other profiles use the variance as a threshold.

With these changes, the reliability of the detrend algorithm is significantly improved. As shown in Table 4.3 and Figures 4.4, 4.5 and 4.6, observed fractures were detected by the revised algorithm on 30 out of 36 profiles, or in 83% of cases. An equal percentage of fractures were over- and under-detected which suggested that algorithm is not biased. The mean is equal to 0.03, the median and mode are both equal to 0.0, and the standard deviation is 0.5. In the instances when the algorithm detected too many fractures there was typically rubble in the fracture gap or debris lodged under the core segments. As mentioned, binning the data only minimizes this issue – it is not fully resolved.

Cores with a combination of very open and borderline tight fractures were also problematic because the large range of z-values increases the value of the variance and lowers the threshold. Thus fractures with a small range of z-values (i.e. borderline tight fractures) tend to be above the threshold and not detected.

Table 4.3: Summary of the results of the revised detrend method.

Method	Threshold	Less than observed (%)	Equal to observed (%)	More than observed (%)	Mean	Median	Mode	Standard Deviation
Revised Detrend	Variance or Standard Deviation $\times 3$	8.0	83.0	8.0	0.03	0.0	0.0	0.5

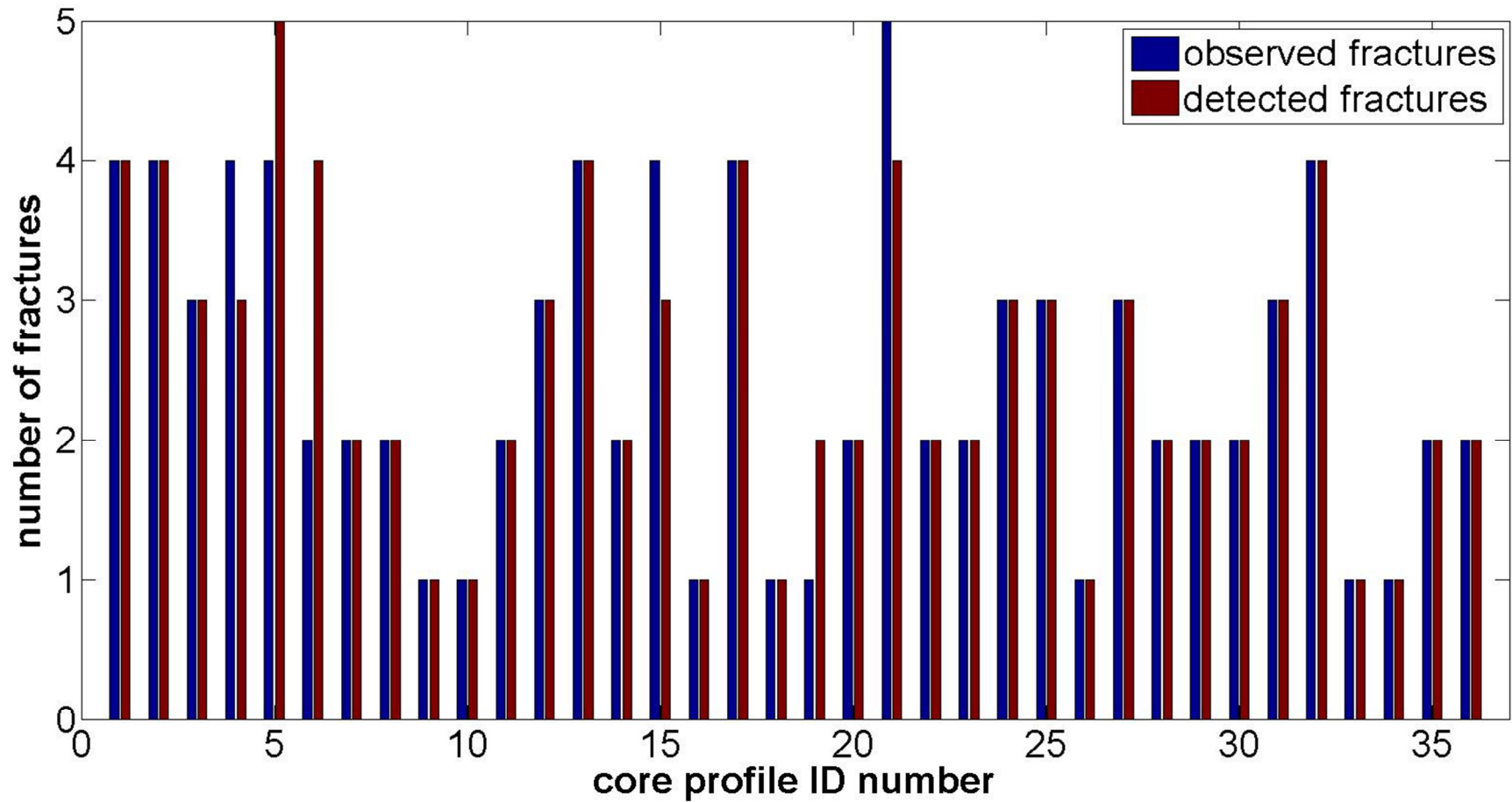


Figure 4.4: Comparison of fractures observed and fractures detected by the revised detrend algorithm. Only the bars of profiles 4, 5, 6, 15, 19 and 21 are not equal.

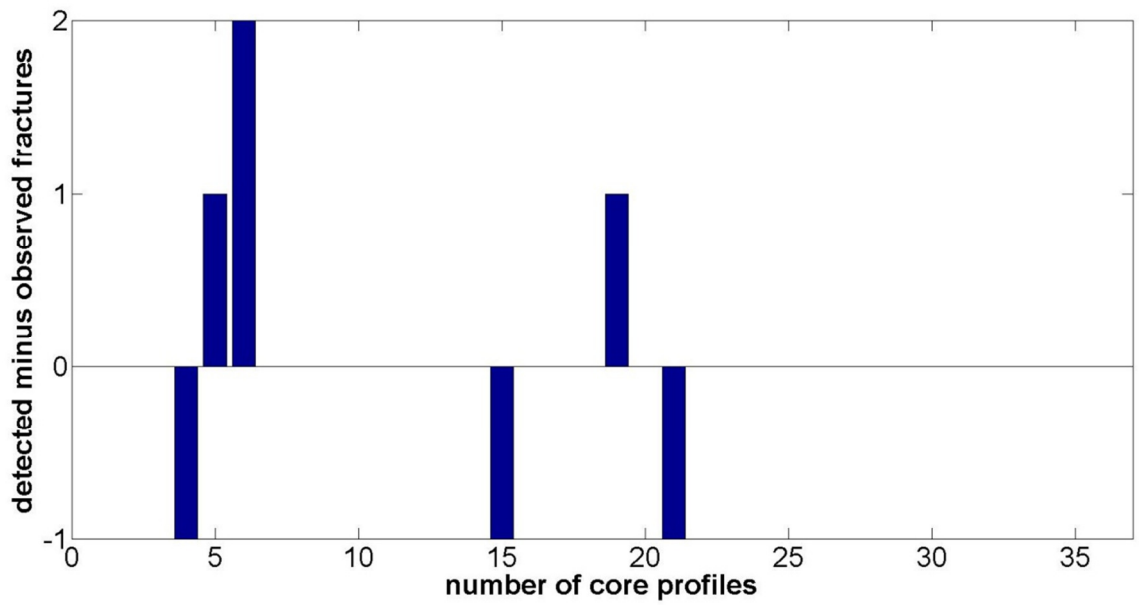


Figure 4.5: Difference between the number of fractures observed and detected (the difference between the bars in Figure 4.4). Profile 6 is over-detected by 2 fractures and the rest are either over- or under-detected by 1 fracture.

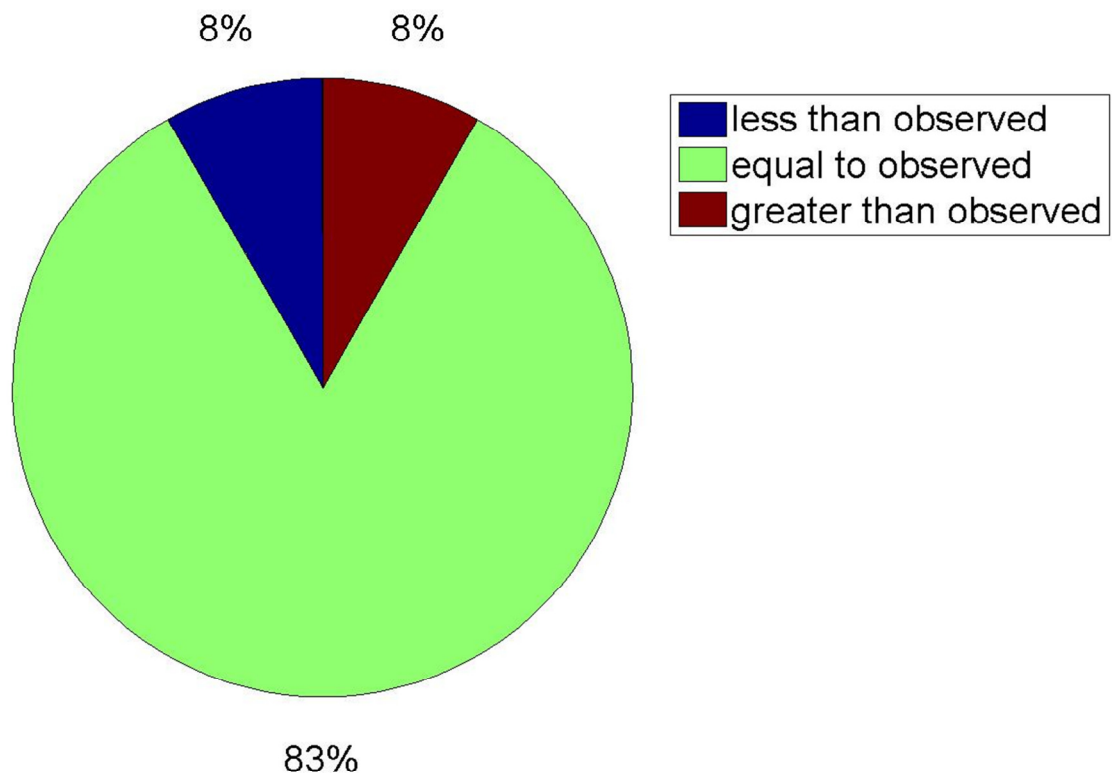


Figure 4.6: The percentage of fractures detected accurately is 83%. Equal percentages (8%) of fractures detected were less than, or greater than observed; this suggests the algorithm is not systematically over- or under-detecting fractures.

4.3 The RQD

The simulated RQD algorithm was tested on 30 of the 36 original profiles; the profiles that had the correct number of fractures detected by the revised detrend algorithm. The results are summarized in Table 4.4. The difference between the detected and observed simulated RQD is used to assess the reliability of the algorithm. The mode of this difference indicates that the algorithm typically underestimates the simulated RQD by 3.0%. The mean, median and standard deviation of the difference are -1.03%, -2.0% and 4.5%, respectively.

The maximum difference is 15% which is well outside the standard deviation. Figure 4.7 is a histogram of the differences between the detected and observed simulated RQD percentages. The vertical lines are the “fences”, outside of which a percentage is considered an “outlier”. The fences are based on the interquartile range (IQR) of the differences. To calculate the IQR, the data are sorted in ascending order. The first quartile (Q_1) is the median between first entry and middle value of the entire data set (i.e. the first quarter of the data are below the value of Q_1). The third quartile (Q_3) is the median between the middle value of the entire data set and the last entry (i.e. the fourth quarter of the data are above the value of Q_3). The IQR is the difference between Q_3 and Q_1 . The lower and upper fences are determined using the following equations:

$$\text{Lower fence} = Q_1 - 1.5(IQR) \quad (4.1)$$

$$\text{Upper fence} = Q_3 - 1.5(IQR) \quad (4.2)$$

Table 4.4: The simulated RQD observed compared to the simulated RQD detected. Core box 2, Section C, Row I and Core box 4, Section A, Row IV were the only two qualitative simulated RQD descriptions which were not consistent.

Core Box	Section	Row	RQD observed		RQD detected	
			(%)	Description	(%)	Description
1	C	I	89	Good	83	Good
		II	73	Fair	70	Fair
	B	I	74	Fair	68	Fair
2	C	I	42	Poor	57	Fair
		II	66	Fair	63	Fair
		III	100	Excellent	100	Excellent
		IV	97	Excellent	93	Excellent
	B	I	78	Good	78	Good
		II	63	Good	72	Good
		III	46	Poor	43	Poor
		IV	80	Good	83	Good
	A	I	98	Excellent	93	Excellent
		III	50	Fair	55	Fair
		IV	98	Excellent	97	Excellent
3	C	II	74	Fair	68	Fair
	B	II	97	Excellent	95	Excellent
	A	I	95	Excellent	91	Excellent
		II	78	Good	78	Good
4	C	I	83	Good	85	Good
		II	100	Excellent	100	Excellent
		III	29	Poor	28	Poor
		IV	42	Poor	40	Poor
	B	I	79	Good	76	Good
		II	71	Good	72	Good
		III	53	Fair	52	Fair
		IV	36	Poor	33	Poor
	A	I	100	Excellent	100	Excellent
		II	98	Excellent	94	Excellent
		III	81	Good	77	Good
		IV	78	Good	73	Fair

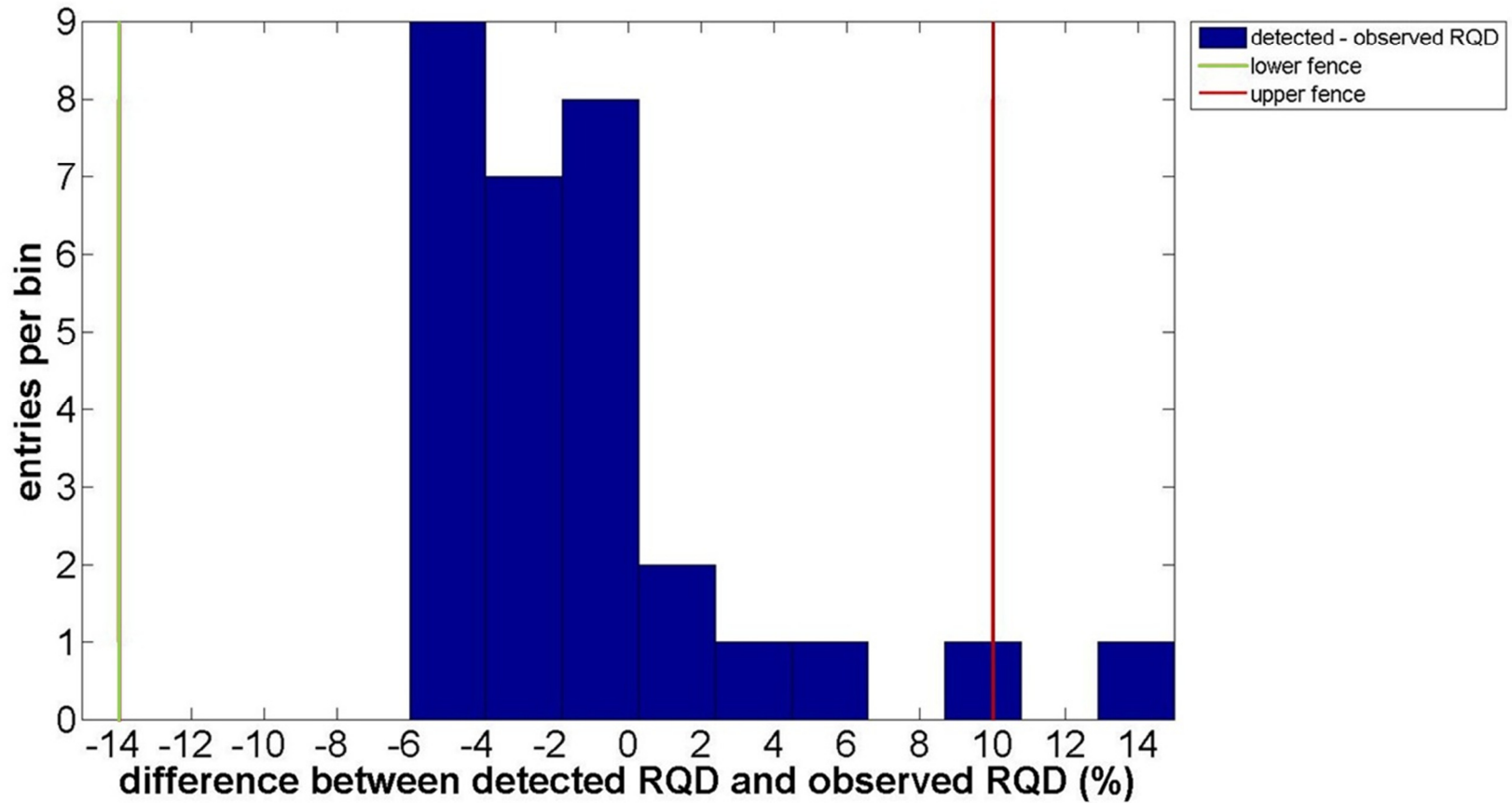


Figure 4.7: A histogram of the percent difference between the detected simulated RQD and the observed simulated RQD. There is one borderline outlier in the ~ 9 -11% bin and a definite outlier in the ~ 13 -15% bin.

As shown in Figure 4.7, the difference of 15% in the ~13-15% bin is outside the upper fence and therefore corresponds to an outlier. There is a borderline outlier in the ~ 9-11% bin. A closer look at the simulated RQD measurements of these outliers reveals that the algorithm extracted the second edge of a fracture instead of the first edge; the gap between the fractures was included in the core segment measurement.

Despite the failure to extract the correct edge of the fracture in the two cases previously discussed, the simulated RQD algorithm performed very well. Differences of a few percent did not have a significant impact on the qualitative description of the simulated RQD; 28 of the 30 profiles were correctly described, as shown in Table 4.4.

4.4 Fracture Characterization

The fracture characterization algorithm is tested on 16 fracture traces, labeled A through P; where fracture traces A-E are curved and F-P are linear.

Two parameters were identified to distinguish natural fractures from mechanical breaks – the angle of the fracture trace and the roughness of the trace. The roughness is determined based on the residuals and the angle of the trace points with respect to the horizontal. Each of these parameters is assigned a value of 0 or 1; mechanical break properties (high angle, rough trace) are 0 and natural fracture properties (low to moderate angle, smooth trace) are 1. Table 4.5 summarizes how the parameters are scored.

Table 4.5: Natural fracture and mechanical break scoring system. The value of each parameter is summed. If all conditions are satisfied for a natural fracture, the score is 3, for a mechanical break the score is 0. For ambiguous fractures, only some of the conditions are satisfied and the score is either 1 (ambiguous mechanical) or 2 (ambiguous natural).

Discontinuity type	Score	Trace angle		Trace roughness (residuals)		Trace roughness (angle of trace points)	
		Description	Value	Description	Value	Description	Value
Natural	3	Low-moderate: 0° to 75°	1	Less than 68.2% of the residuals greater than the standard deviation	1	More than 68.2% of the angles are in a single histogram bin	1
Ambiguous natural	2	105° to 255° 285° to 0°					
Ambiguous mechanical	1	High: 75° to 105° 255° to 285°	0	More than 68.2% of the residuals greater than the standard deviation	0	Less than 68.2% of the angles are in a single histogram bin	0
Mechanical	0						

As discussed in the previous chapter, the fracture characterization algorithm must first distinguish between traces which are curved or linear. This part of the program had a 100% success rate, as shown in Table 4.6.

If the trace is curved, a sine wave is used to determine the roughness. With the first method the trace data are recalculated to fit to a sine wave. To determine whether the trace is rough or smooth, a sine wave with the same amplitude and range of x-values is subtracted from the fitted trace data. Unfortunately, the fitting worked too well, as illustrated in Figures 4.8 and 4.9. The residuals for the rough and smooth traces were very similar. Therefore this method did not successfully distinguish rough traces from smooth traces – all the fractures were categorized as natural. Interestingly, this is correct; all the curved traces tested are from natural fractures.

The second method involves overlaying a sine wave, with the same amplitude and range of y-values as the trace data, on the raw fracture trace. This approach did not produce better results, as illustrated in Figure 4.10. The amplitude of the sine wave and the trace match reasonably well; as do the sine wave and the lower limb of the trace. However, the sine wave is too narrow to align with the upper limb of the trace; the reason appears to be that, unlike sine waves, fracture traces are typically not symmetrical. Again, the roughness of the fracture trace could not be determined and all fractures tested were categorized as ambiguous mechanical by the algorithm.

Table 4.6: Results of the curve-line detection algorithm test. The shape of each fracture trace was correctly identified.

Fracture Trace	Observed	Detected
A	Curve	Curve
B	Curve	Curve
C	Curve	Curve
D	Curve	Curve
E	Curve	Curve
F	Linear	Linear
G	Linear	Linear
H	Linear	Linear
I	Linear	Linear
J	Linear	Linear
K	Linear	Linear
L	Linear	Linear
M	Linear	Linear
N	Linear	Linear
O	Linear	Linear
P	Linear	Linear

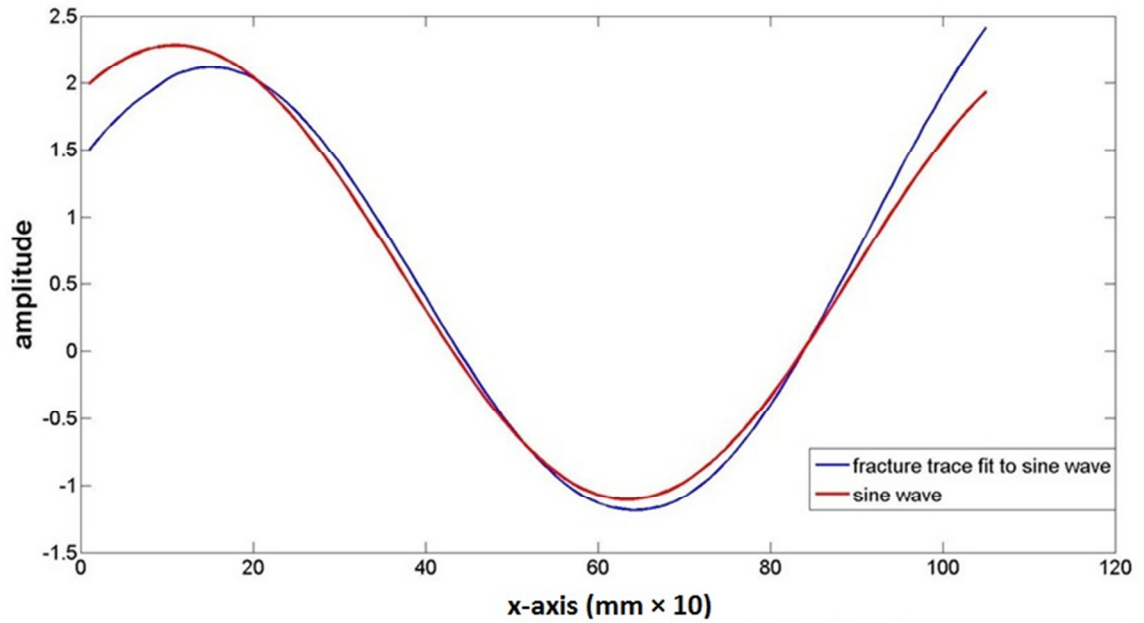


Figure 4.8: Below, digital photograph of core sample B with a smooth curved fracture trace. Above, the smooth curved fracture trace for this core is recalculated to fit a sine wave (blue) compared to a sine wave with the same amplitude and range of x-values (red).

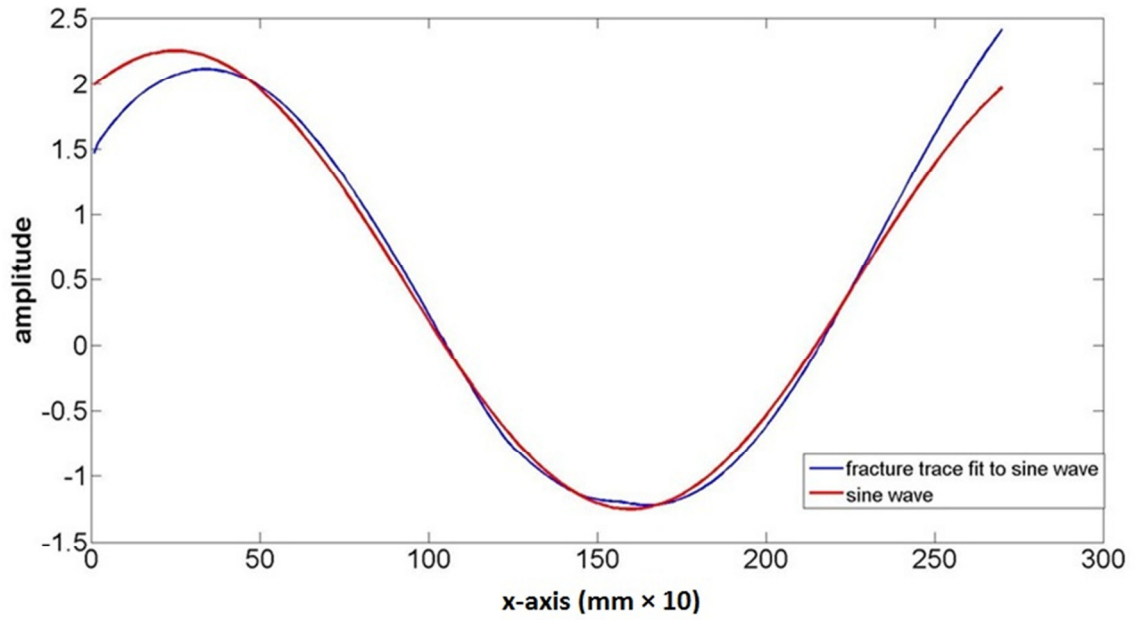
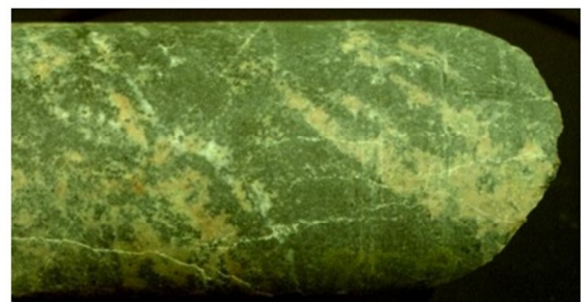
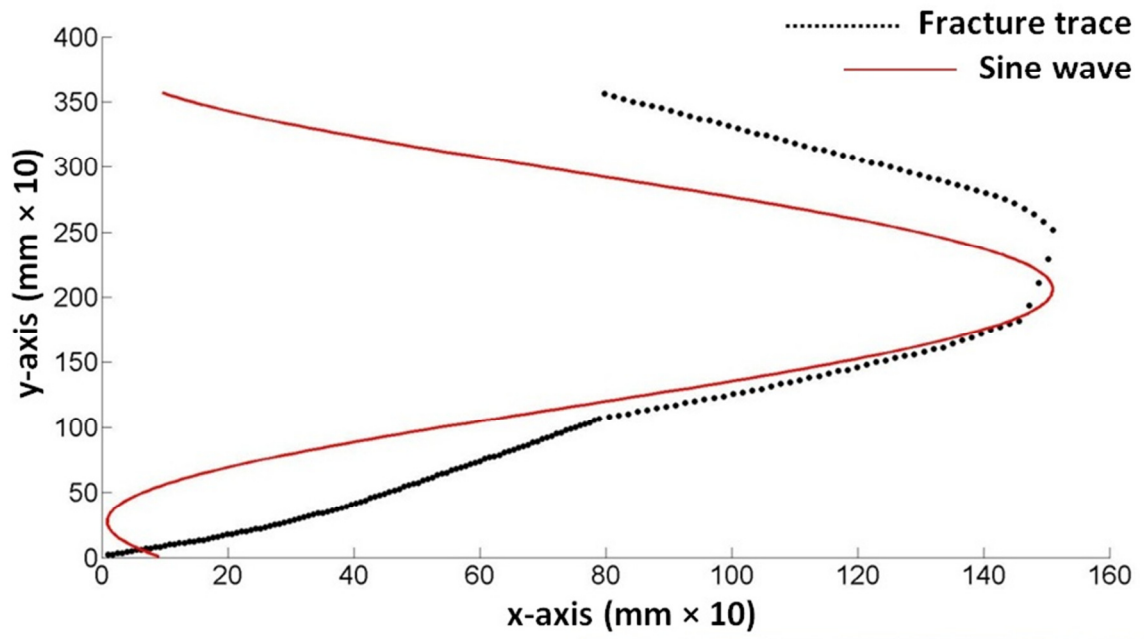


Figure 4.9: Below, digital photograph of core sample A with a rough curved fracture trace. Above, rough curved fracture trace recalculated to fit to a sine wave (blue) compared to a sine wave with the same amplitude range of x-values (red). The result is very similar to that of the smooth trace in Figure 4.8.



4.10: Below, digital photograph of core sample C with a slightly rough curved fracture trace. Sine wave (red), with the same amplitude and range of y values as the trace data overlaid on the raw fracture trace (black). The trace shape is too irregular and asymmetrical, and does not fit the sine wave well.

The algorithm for linear traces is much more reliable. The outputs were 100% consistent with the observations, as shown in Table 4.7. The 11 linear fracture traces are tested, labeled F through P. Samples G and M each had a combination of mechanical and natural trace attributes and were the most ambiguous in origin. Sample G is a mechanical fracture with a low angle of 206° . The breakage surface had to be compared to others in the same core box to determine if it was fresh, and confirm that the break was, in fact, mechanical. Sample M was originally selected as an example of a mechanical fracture because of its high-angle breakage surface. However, on closer inspection, it was clear that the breakage surface was weathered, indicating that the fracture was natural. It is important to note that, given the ambiguous characteristics of these fractures, others may describe them differently; this only underscores the need for more research on the properties of natural fractures and mechanical breaks. These fractures are illustrated in Figure 4.11.

Table 4.7: Results of the linear trace fracture characterization algorithm are consistent with the observations.

Sample	Trace Angle		Roughness Residuals		Roughness Angles		Score	Observations	Detected
	Angle	Value	(%)	Value	(%)	Value			
F	100.7	0	80.9	0	50	0	0	High angle Rough trace	Mechanical
G	206.8	1	77.8	0	39.6	0	1	Low angle Rough trace	Ambiguous mechanical
H	90	0	98.5	0	47.8	0	0	High angle Very rough trace	Mechanical
I	90	0	89	0	51.9	0	0	High angle Very rough trace	Mechanical
J	135	1	39.8	0	41.4	0	1	Moderate angle Rough trace	Ambiguous mechanical
K	135	1	87.3	0	50.2	0	1	Moderate angle Very rough trace	Ambiguous mechanical
L	243.5	1	12.5	1	56.3	0	2	Moderate angle Smooth trace	Ambiguous natural
M	95.7	0	0	1	92.9	1	2	High angle Very smooth trace	Ambiguous natural
N	225	1	66	0	75.5	1	2	Moderate angle Rough trace	Ambiguous natural
O	225	1	5.9	1	85.8	1	3	Moderate angle Very smooth trace	Natural
P	225	1	12.1	1	65	0	2	Moderate angle Smooth trace	Ambiguous natural

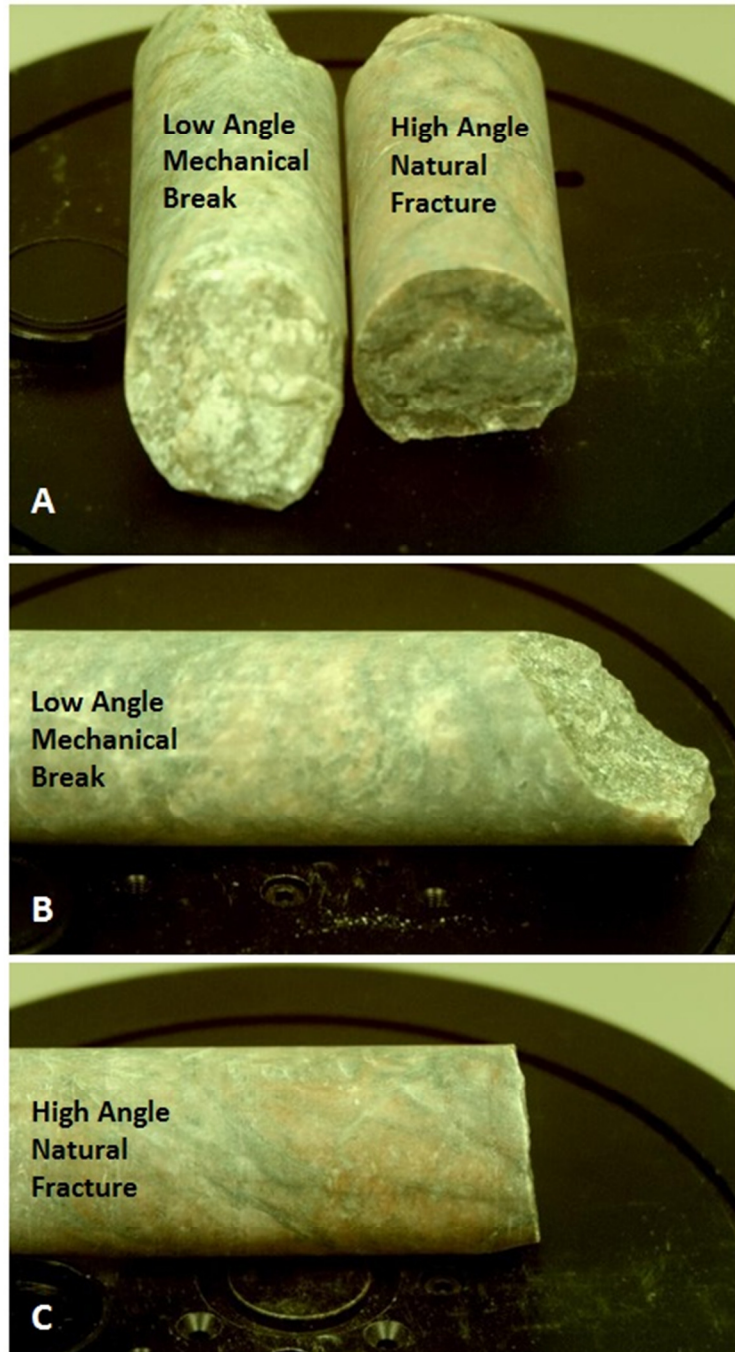


Figure 4.11: Shown in A, B and C is the core of the same rock type (gneiss). Illustrated in A (left) and B is a low angle mechanical break. The fresh breakage surface visible in A (left) is much brighter than the weathered surface shown in A (right). High angle natural break A (right) and C. The dark weathered surface is visible in A (right). These ambiguous fractures were correctly identified by the fracture characterization algorithm.

4.5 Distance-Based Images

Presented in Figures 4.12 and 4.13 is a comparison of the performance of some of the image processing and feature detection techniques available in the MATLAB image processing toolbox. The comparison is between digital photographs and distance-based images of core. No pre- or post-processing is used to enhance or obscure any features. Figure 4.12 is a sample that was not fractured and had pronounced gneissic texture with alternating bands of light and dark minerals. The tools did not detect the rock texture when used on the distance-based images. The tools detected a significant amount of rock texture on the digital photograph which would make further processing – to detect fractures – problematic.

As illustrated in the right column of Figure 4.13, with the rock texture eliminated, boundary and object detection tools were better able to highlight fractures. This is a single core from a core box scan at a digitizer-to-target distance of approximately 1 m.

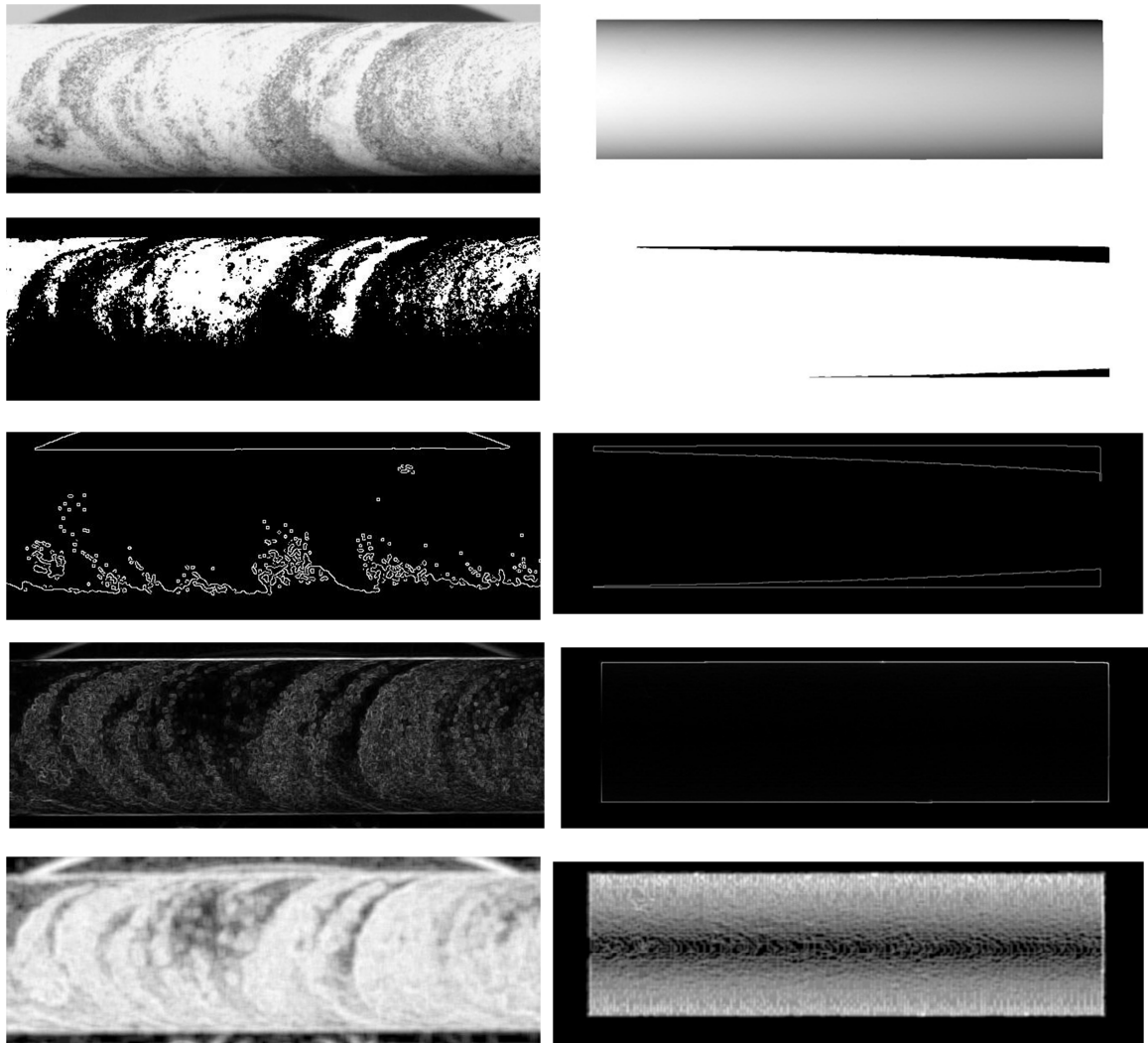


Figure 4.12: Core with pronounced gneissic rock texture and no fractures. A comparison of the performance of several functions from the MATLAB image processing toolbox. Single core image: black and white digital photograph (first row left) and range-based image (first row right). The same boundary and object detection tools were applied to each image type. From top to bottom: binary image, Sobel edge detector, local standard deviation and local entropy.

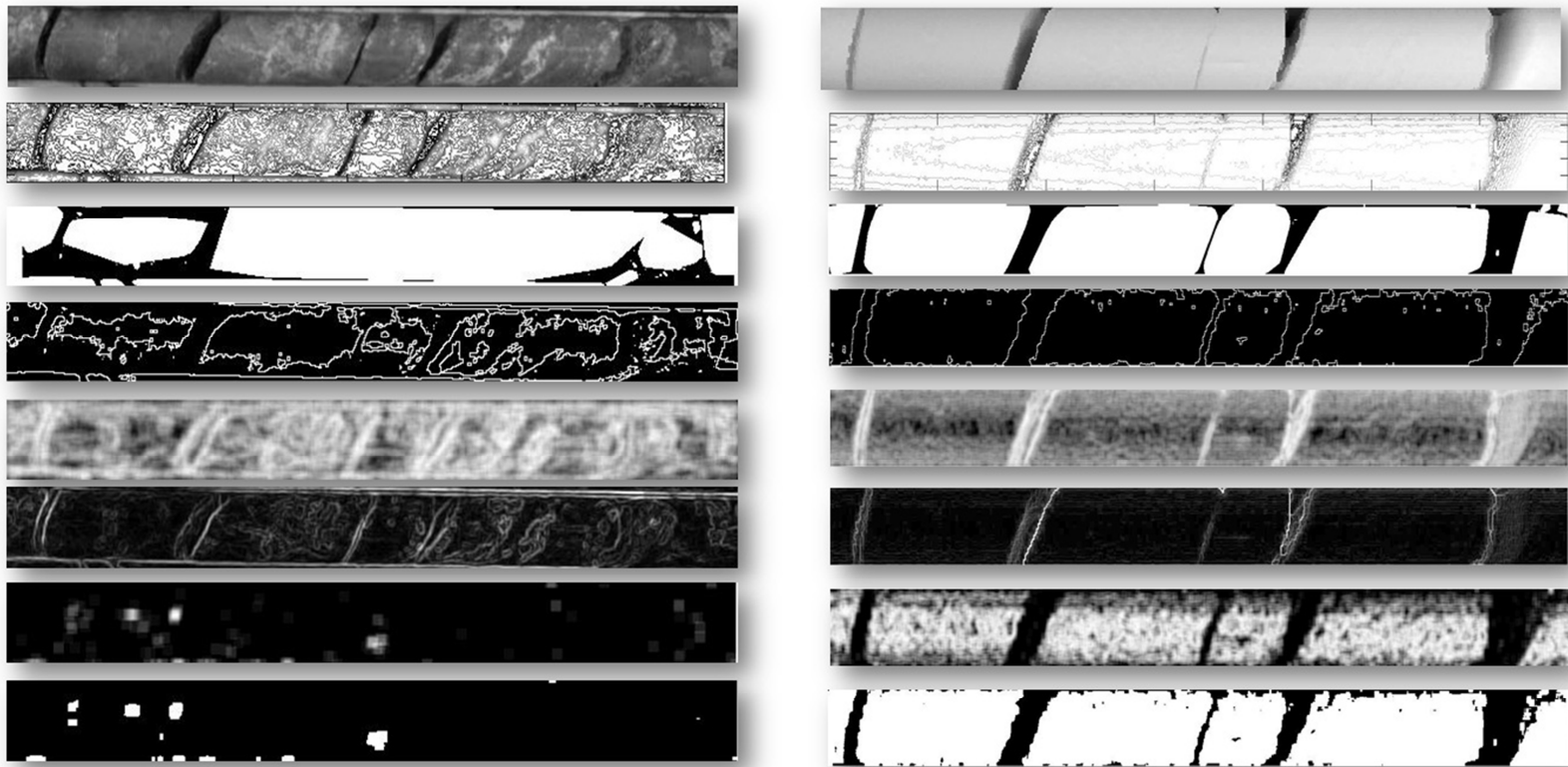


Figure 4.13: Comparison of the performance of several functions from the MATLAB image processing toolbox. Single core image: black and white digital photograph (first row left) and range-based image (first row right). The same boundary and object detection tools were applied to each image type. From top to bottom: contour plot, convex hull, perimeter of convex hull, local entropy, local range, entropy of local range and binary image of the entropy of local range.

4.6 The 3-D Core Models

Three cores were scanned; digital photographs of the cores are shown in Figures 4.14, 4.15 and 4.16. The cores represent a spectrum of modeling difficulty. Core 1 approaches the shape of a cylinder, whereas core 3 has the greatest number of distinctive features.

- Core 1: granite with moderately rough, high-angle mechanical breaks at each end. One breakage surface has a large potassium feldspar crystal which protrudes slightly from the edge – this is the only distinguishing feature.
- Core 2: gneiss with one very smooth, moderate-angle natural fracture and one relatively smooth, high-angle fracture with a chip along part of the fracture edge.
- Core 3: fine-grained gabbro with rough, moderate-angle natural fractures. These fractures have several distinguishing features.

The corresponding three core models are presented in Figures 4.17, 4.18 and 4.19. As shown in these figures, the models can be rotated and viewed from any angle. Studying these figures, it is clear that core 1 (Figure 4.14) is not as well rendered as core 2 and core 3. A comparison of the rendering quality is shown in Figure 4.20. The rendering difficulties reflect poor alignment of the original images, which in turn is due to a lack of identifiable features on the core surface. A more quantitative evaluation of the quality of the models is the average standard deviation automatically calculated by the Polyworks software; it corresponds to the average standard deviation of the distance between the

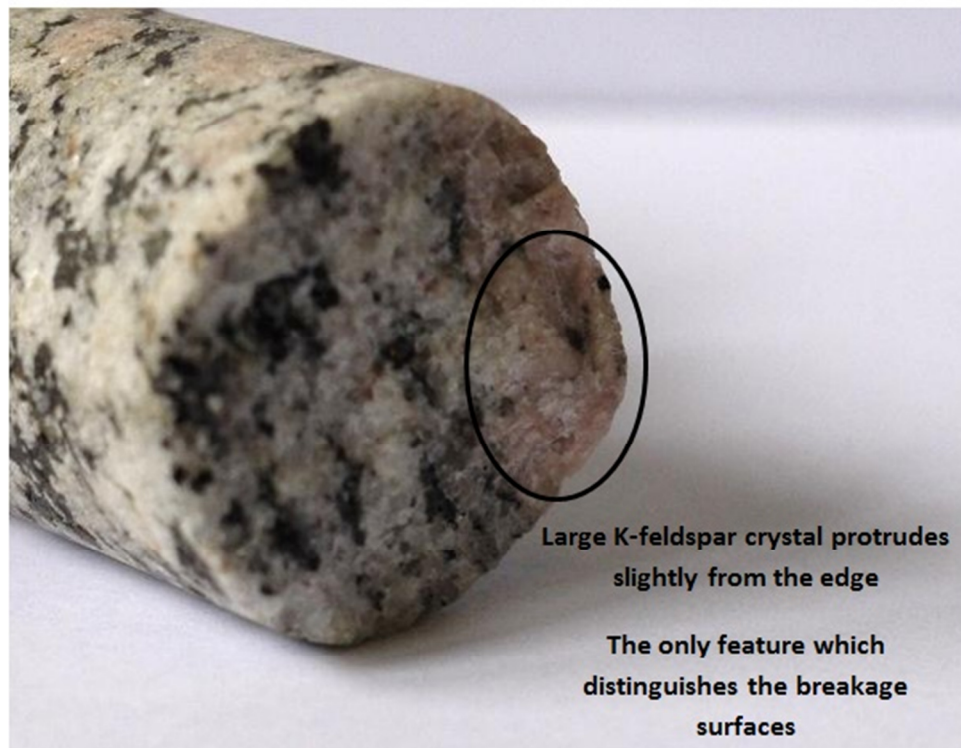
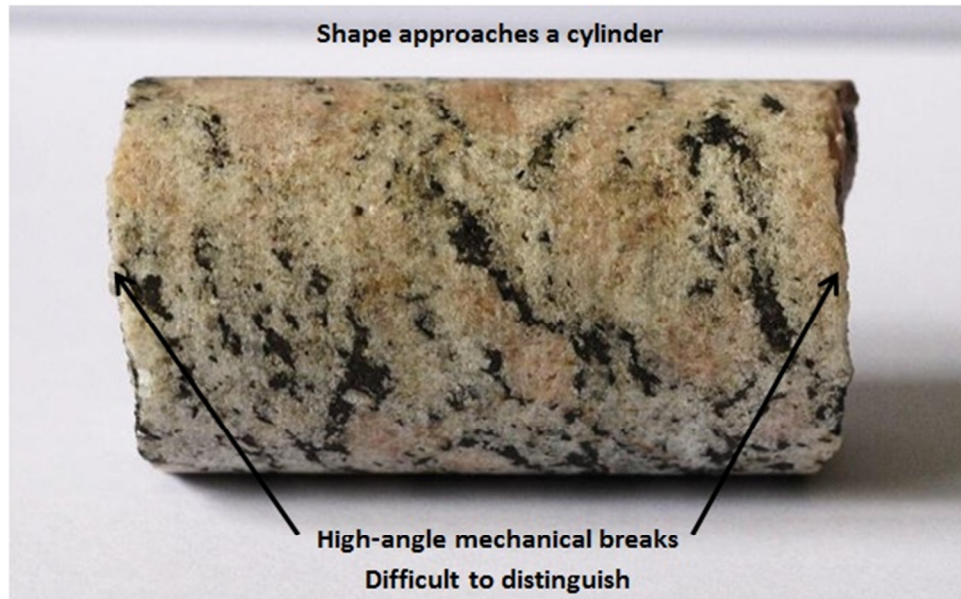


Figure 4.14: Digital photograph of core 1, granite. Core breakage surfaces are difficult to distinguish from each other. Core 1 approaches the shape of a cylinder more closely than the other two cores. Core diameter is 36.5 mm.

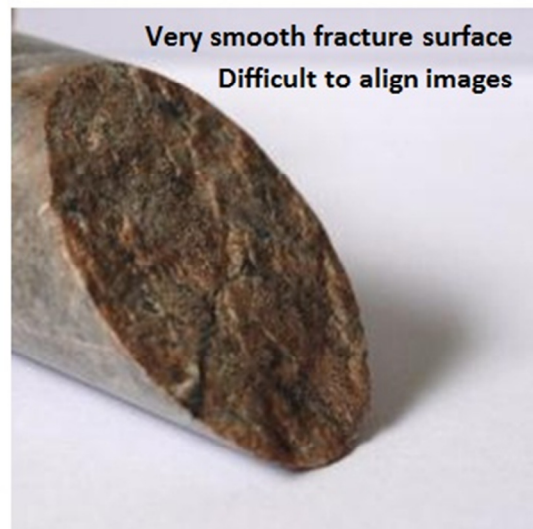


Figure 4.15: Digital photograph of Core 2, gneiss. Core breakage surfaces are easy to distinguish from each other. The natural fracture has a very smooth surface with minimal identifiable features which makes aligning the images difficult. Core diameter is 36.5 mm.

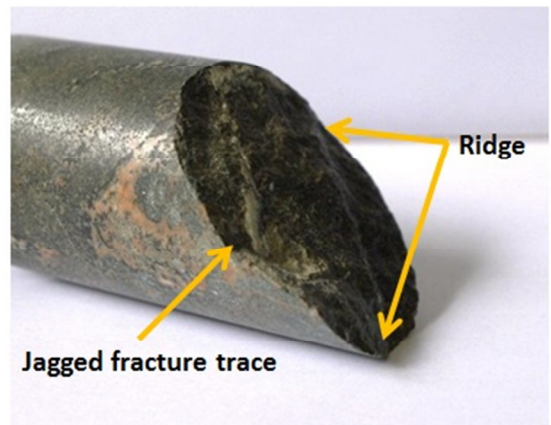
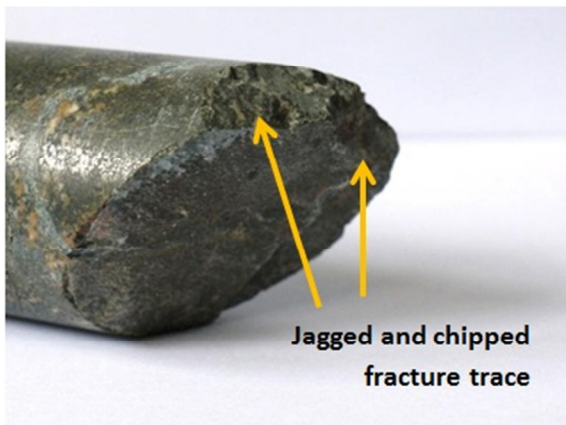
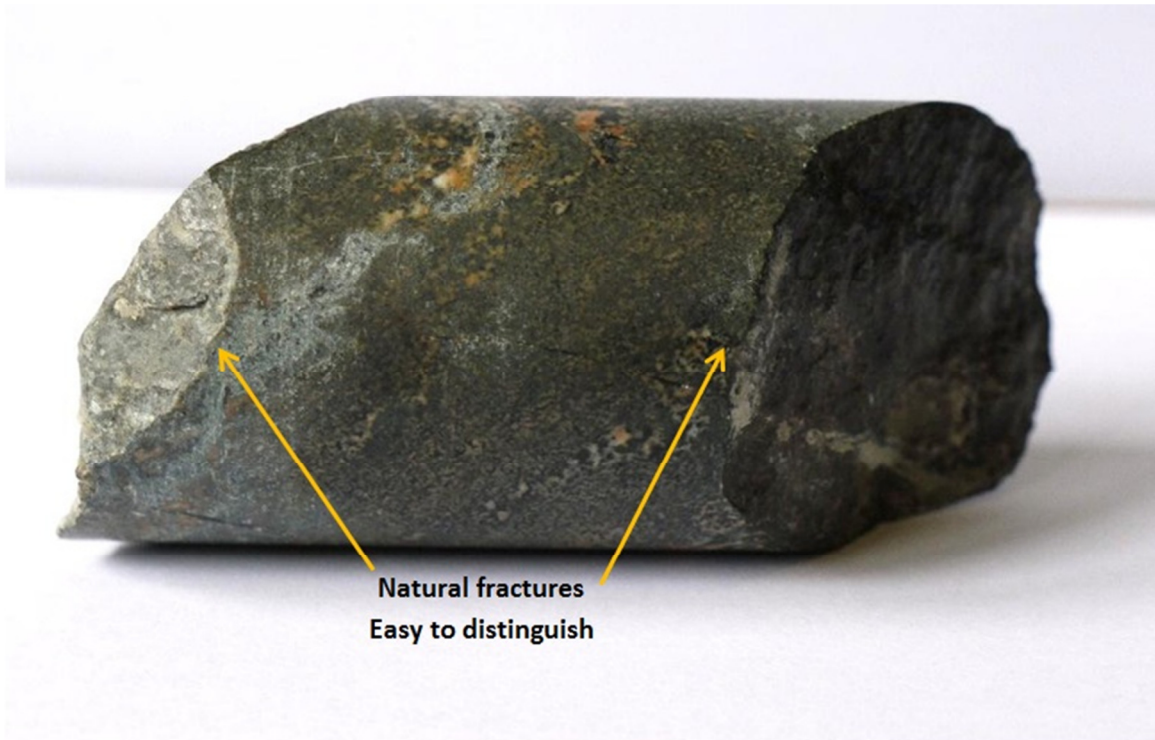


Figure 4.16: Digital photograph of Core 3, gabbro. Core breakage surfaces are easy to distinguish from each other. Both natural fractures have several identifiable features. Image alignment for core 3 was easier than for cores 1 and 2, though still challenging due to the general cylindrical shape. Core diameter is 46.7 mm.

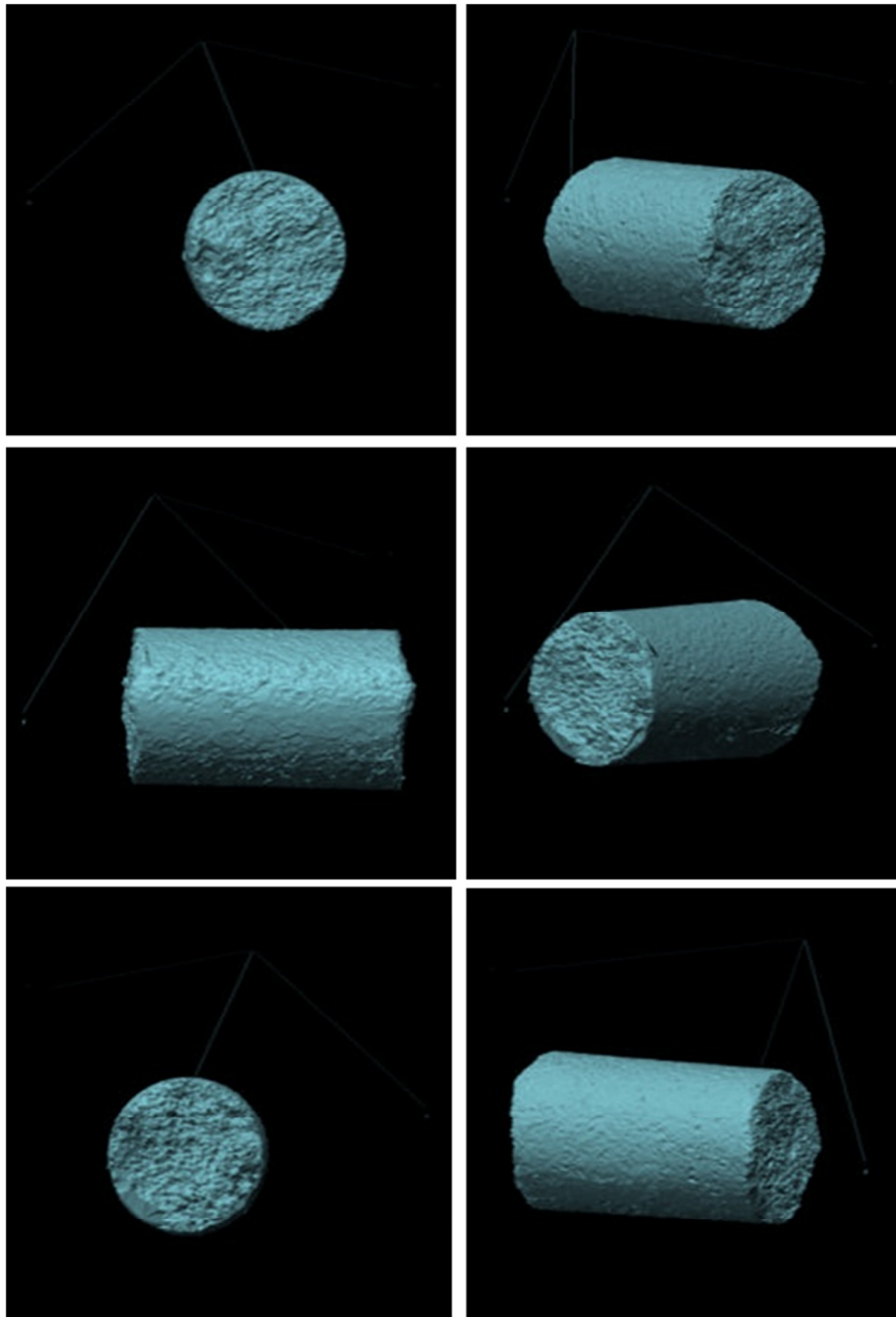


Figure 4.17: 3-D model of core 1 viewed from various perspectives. The breakage surfaces are very similar in appearance.

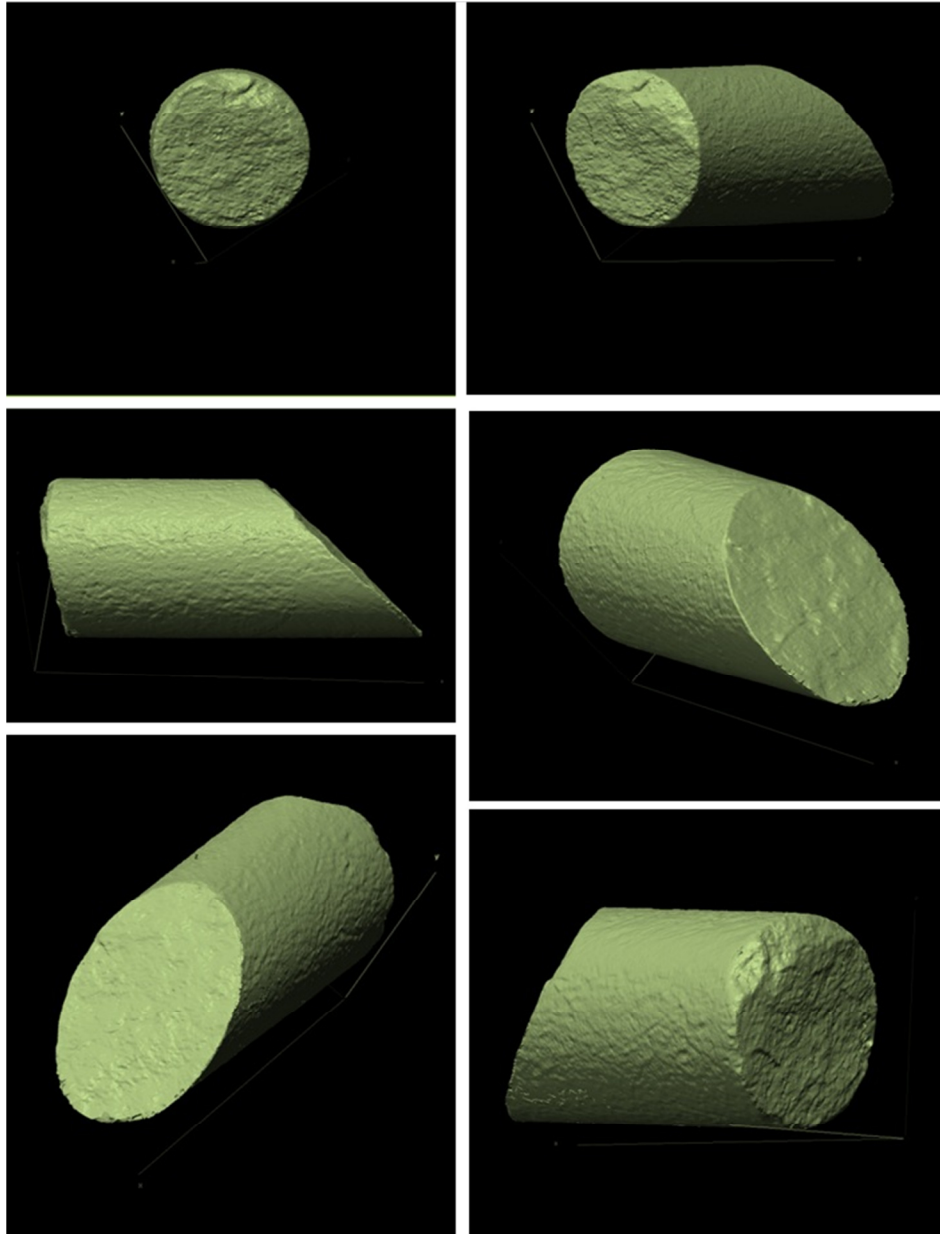


Figure 4.18: 3-D model of core 2 viewed from various perspectives. The breakage surfaces are easy to distinguish from each other. The chip on the mechanical breakage surface is clearly visible. The natural fracture surface has few identifiable features.

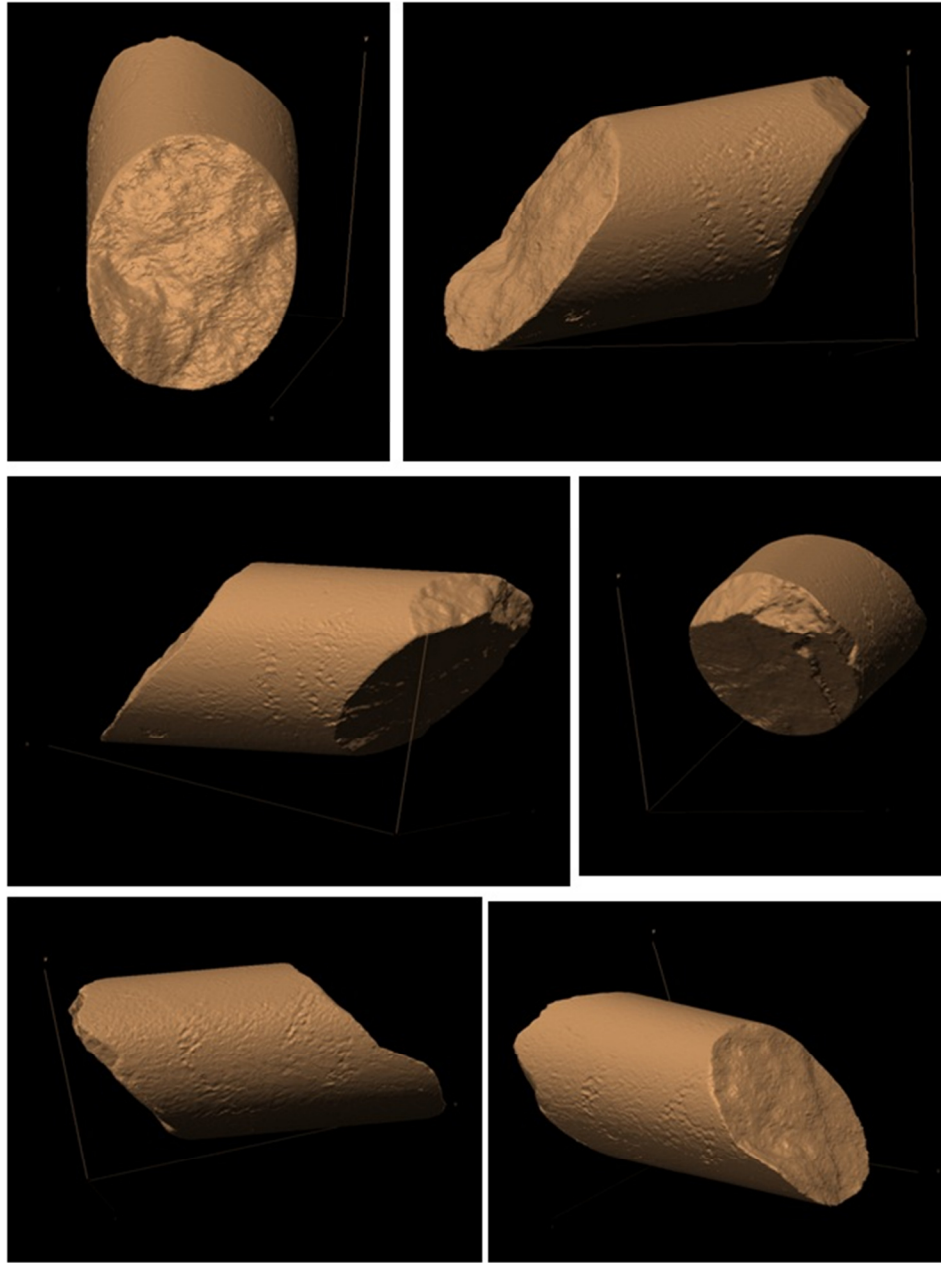


Figure 4.19: 3-D model of core 3 viewed from various perspectives. The breakage surfaces are easy to distinguish from each other.

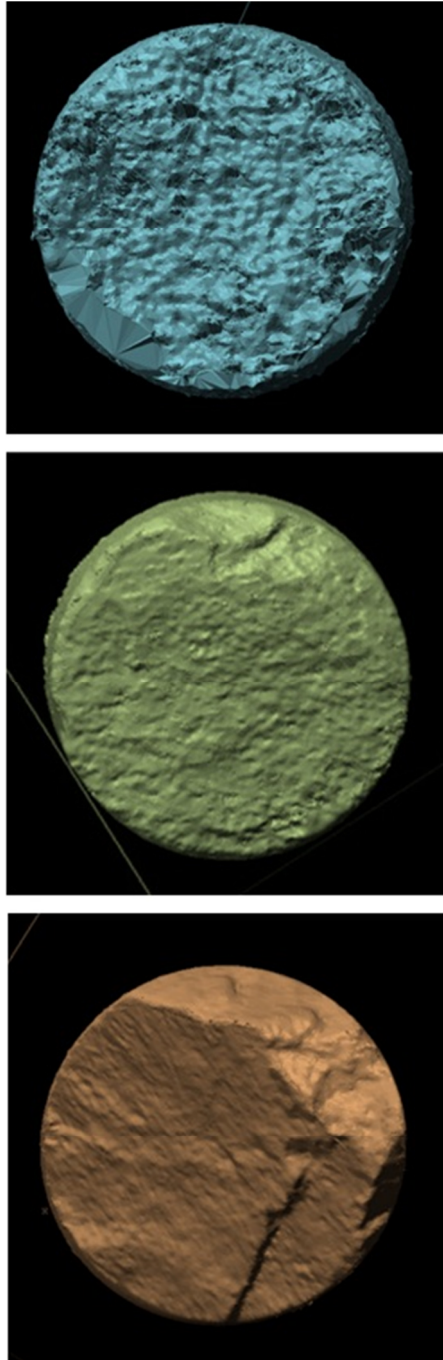


Figure 4.20: Comparison of the rendering quality between the core models. Core 1 is shown in blue, core 2 in green and core 3 in orange. Core model 1 has pits and smooth areas, and does not represent the breakage surface well compared to core models 2 and 3.

points of each image used to assemble the model. For core models 1, 2 and 3 the average standard deviation is 0.20 mm, 0.09 mm and 0.06 mm, respectively. The average standard deviation of core model 3 is close to the accuracy of the digitizer (0.05 mm).

The volume is automatically calculated by the Polyworks software. By measuring the mass with a balance, the density can be manually calculated. The volume, mass and density measurements are summarized in Table 4.8, and compared to the density range of the associated rock types. The density of each core sample falls within the density range of the rock type.

Table 4.8: The density of core samples compared to the density range of the rock type. The density ranges were taken from Reynolds (1997).

Core Model	Volume (cm ³)	Mass (g)	Density (g/cm ³)	Density range (g/cm ³)	
1 Granite	58.96	145.55	2.47	Granite	2.5 – 2.8
2 Gneiss	70.87	184.30	2.60	Gneiss	2.6 – 3.0
3 Gabbro	125.48	357.10	2.85	Gabbro	2.7 – 3.5

5. Summary of Image Processing Algorithms

5.1 Overview

The programs described in the previous sections are presented in this chapter as a series of flowcharts. Figure 5.1 is summary flow chart of the overall flow of the image processing tasks.

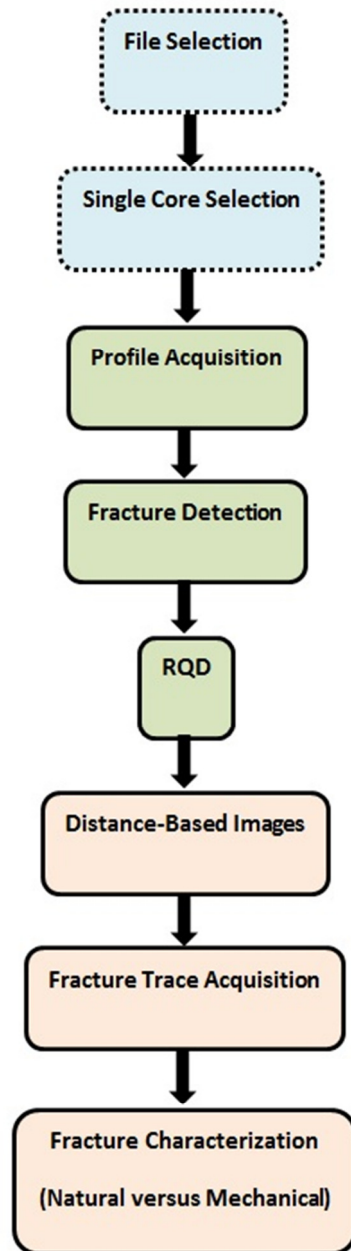


Figure 5.1: Summary of the image processing tasks presented in the following figures. The blue shaded squares with dashed outlines indicate the operation is performed by the program user through a GUI. A solid outlined square denotes that the operation is done automatically by the algorithm. A green shaded square indicates that the algorithm analyzes profiles, whereas an orange shaded square denotes that the program uses the distance-based images.

5.2 *The Flowchart Legend*

Figure 5.2 is the flowchart legend. In this section, the symbols used to represent program inputs, actions, decisions point, outputs, etc. are explained. The program inputs are rectangles and may be an ASCII file or an output from a previously run algorithm. Trapezoids represent actions, such as measuring distances, calculating the standard deviation, or using a MATLAB function. Hexagons represent instances when data above, below or equal to a certain threshold or within certain coordinates are extracted or located. A solid blue arrow indicates the next step in the program. If a shape outline is dashed, the action is controlled by the program user through a graphical user interface (GUI). For shapes with a solid outline, the action is performed by the algorithm automatically. A light blue filled diamond indicates a decision point within the algorithm, such as which threshold to use, or how to categorize the data. Outlined arrows are linked to the decision diamonds. The direction of these arrows indicates which decision the algorithm has made. A solid blue inverted triangle is used after a decision. Regardless of the decision, the data are merged back into the program and subsequently processed with the same steps. A shaded triangle is a program output.

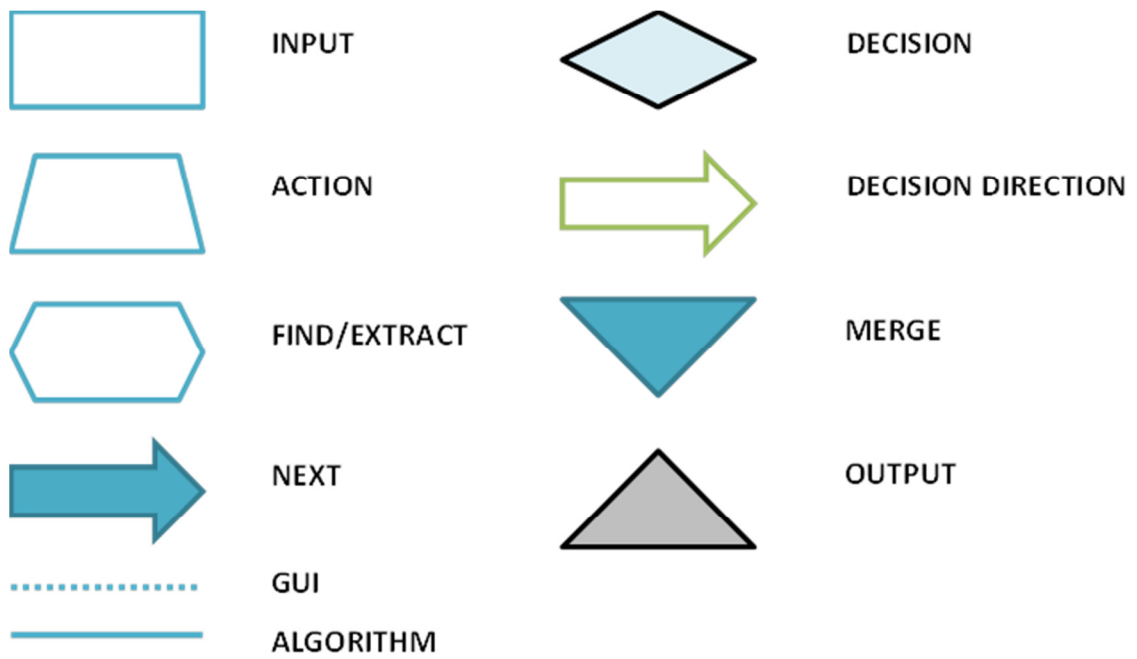


Figure 5.2: Flowchart legend.

5.3 Single Core Image Acquisition Algorithm

This is the only stage of the image analysis process where a graphical user interface (GUI) is required. As indicated by the dashed lines in Figure 5.3, the user chooses the desired ASCII file and then selects the core of interest through a GUI. The GUI interaction is shown in Figure 5.4 and 5.5. From this point forward, the algorithm extracts the data and processes it automatically. The output is a point cloud of a single core. The single core data are used to obtain the centerline profile and generate the distance-based images.

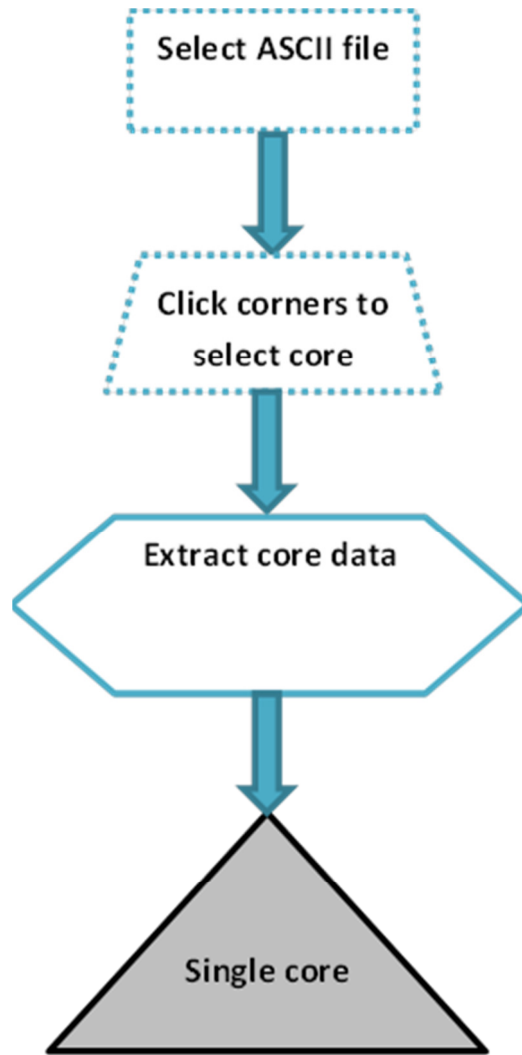


Figure 5.3: Single core image acquisition algorithm.

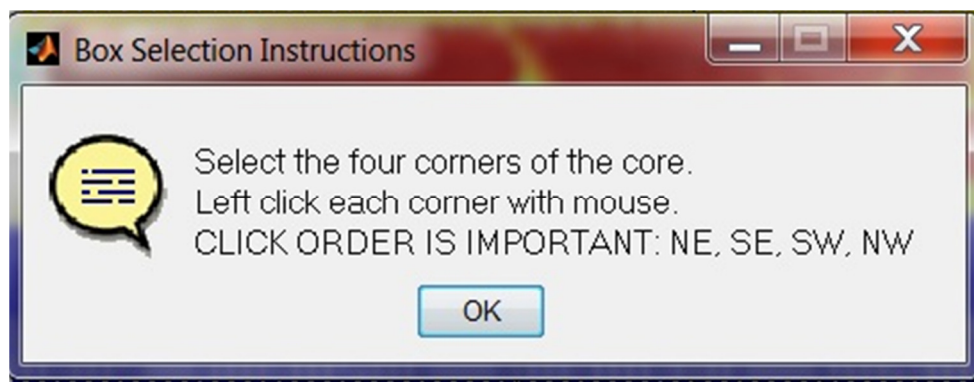
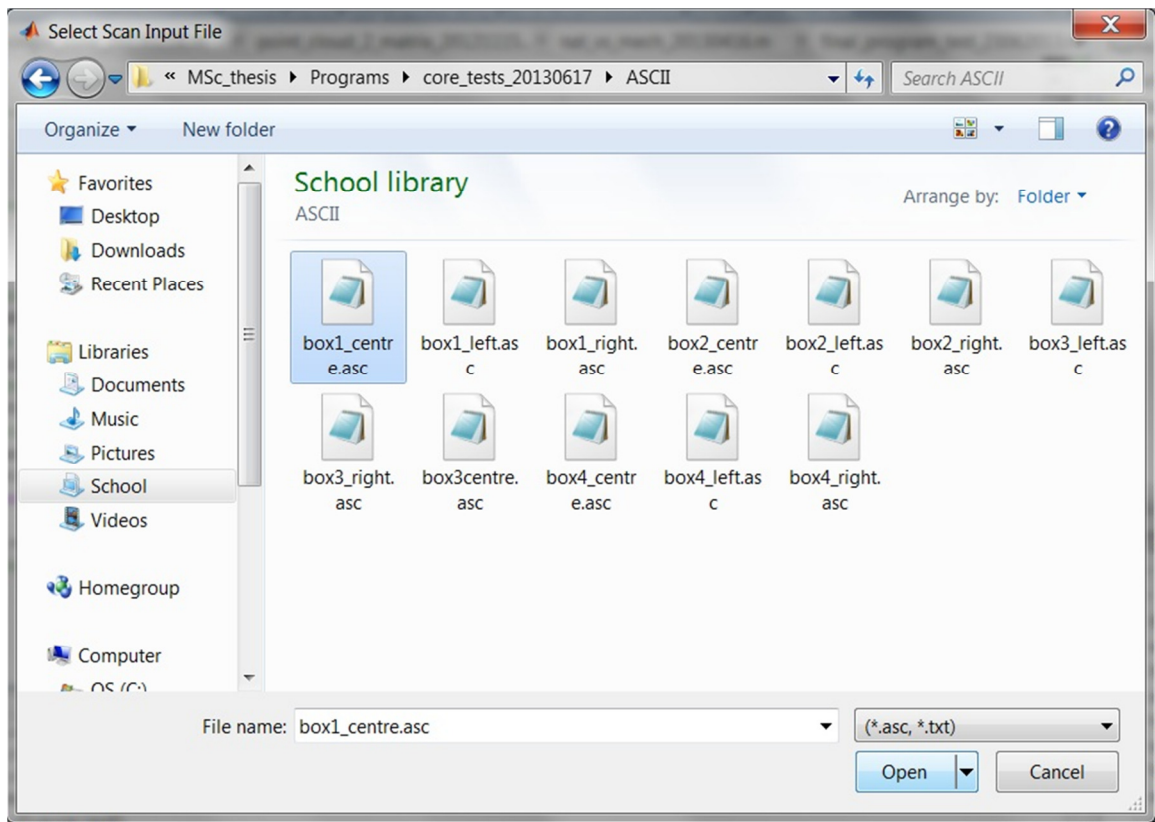


Figure 5.4: The GUI used to select the desired ASCII file (top). After the file is selected, the core box data are plotted using Delaunay triangulation. The user selects the core of interest directly on the plot. Before the selection a pop-up window appears with the instructions (bottom).

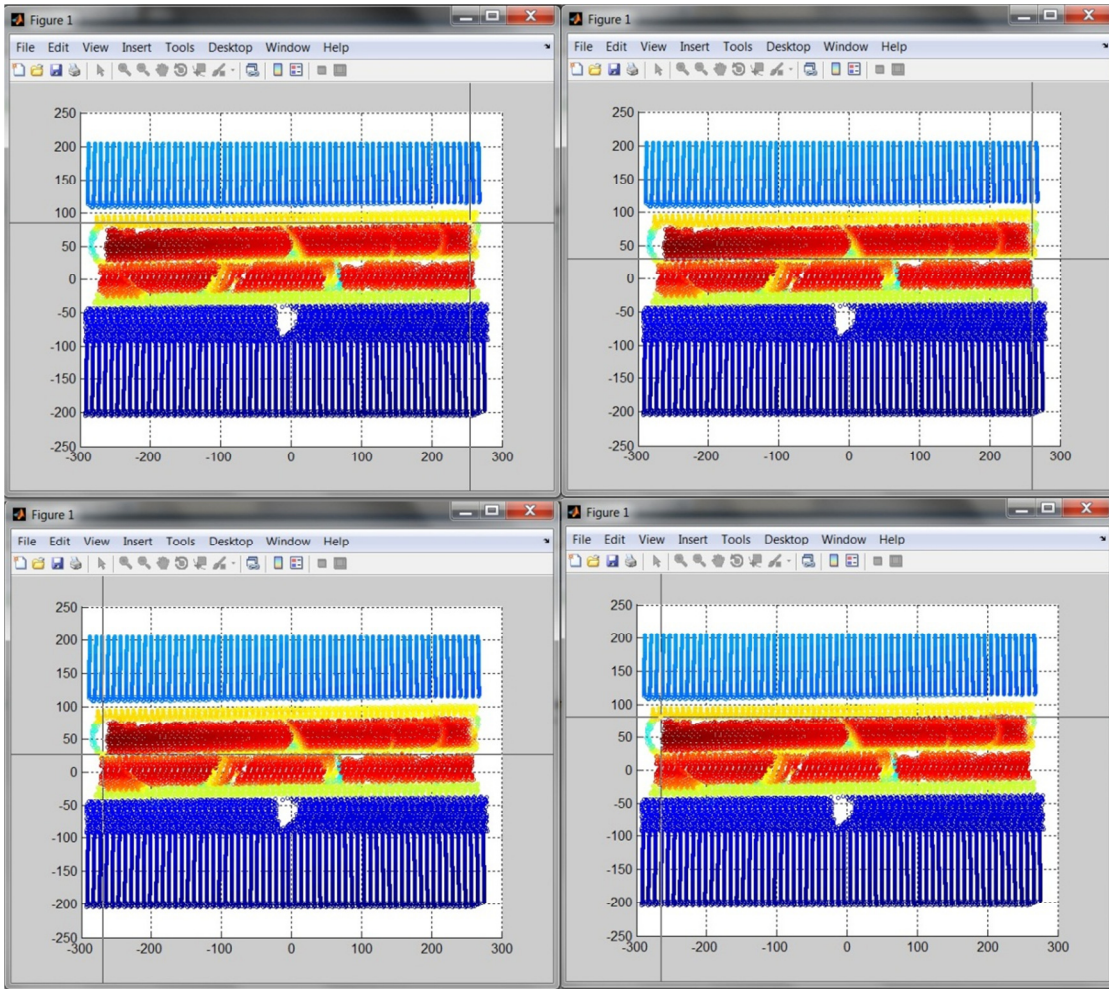


Figure 5.5: The user selects the four corners around the core interest directly on the Delaunay triangulation. The corners must be left clicked with the mouse in clockwise order, starting in the northeast (top right) corner.

5.4 Profile Acquisition Algorithm

Illustrated in Figure 5.6 is the profile acquisition algorithm. The single core point cloud is the input for this program. The algorithm automatically locates the centerline and extracts the profile data. The output is an xz profile along the axis of the core. The profile is used to determine the number of fractures.

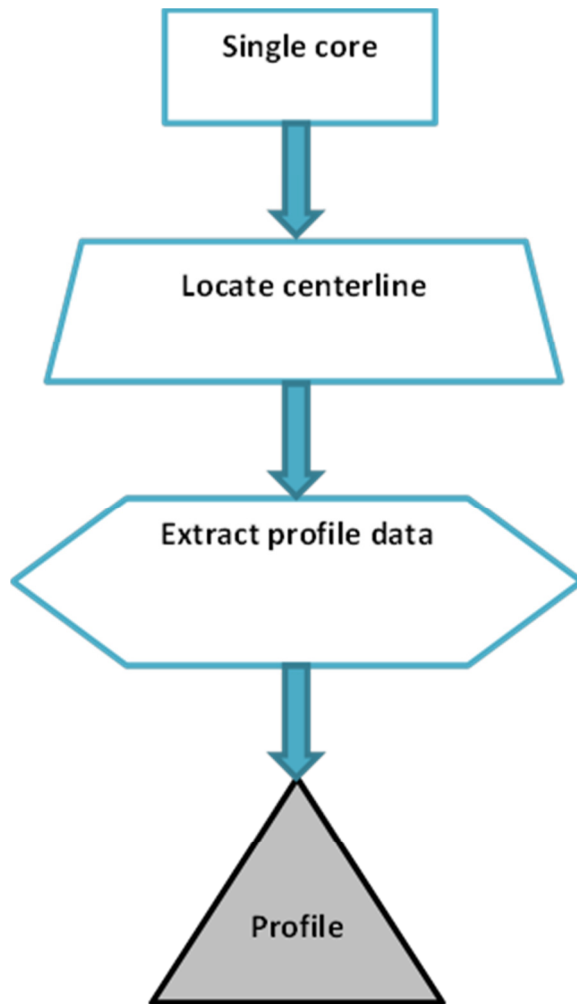


Figure 5.6: Profile acquisition algorithm.

5.5 Fracture Detection Algorithm

The fracture detection algorithm is shown in Figure 5.7. The profile output is the input for this algorithm. The trend is removed from the profile and the data are binned. Data greater than the mean are identified and extracted. The variance is the threshold for data with a large range of z-values (left hexagon shown in green). For data with a small range of z-values (i.e. with tight fractures only or no fractures), three standard deviations are used as threshold for fracture identification (right hexagon shown in orange). Regardless of the threshold used, the groups of ones (flagged for positive fracture identification) within the zeros (no fracture) are used to locate and count fractures. The program outputs are a pop-up message box which displays the number of fractures, shown in Figure 5.8, and a binary profile of fractures and intact core. The binary profile is used to determine the RQD.

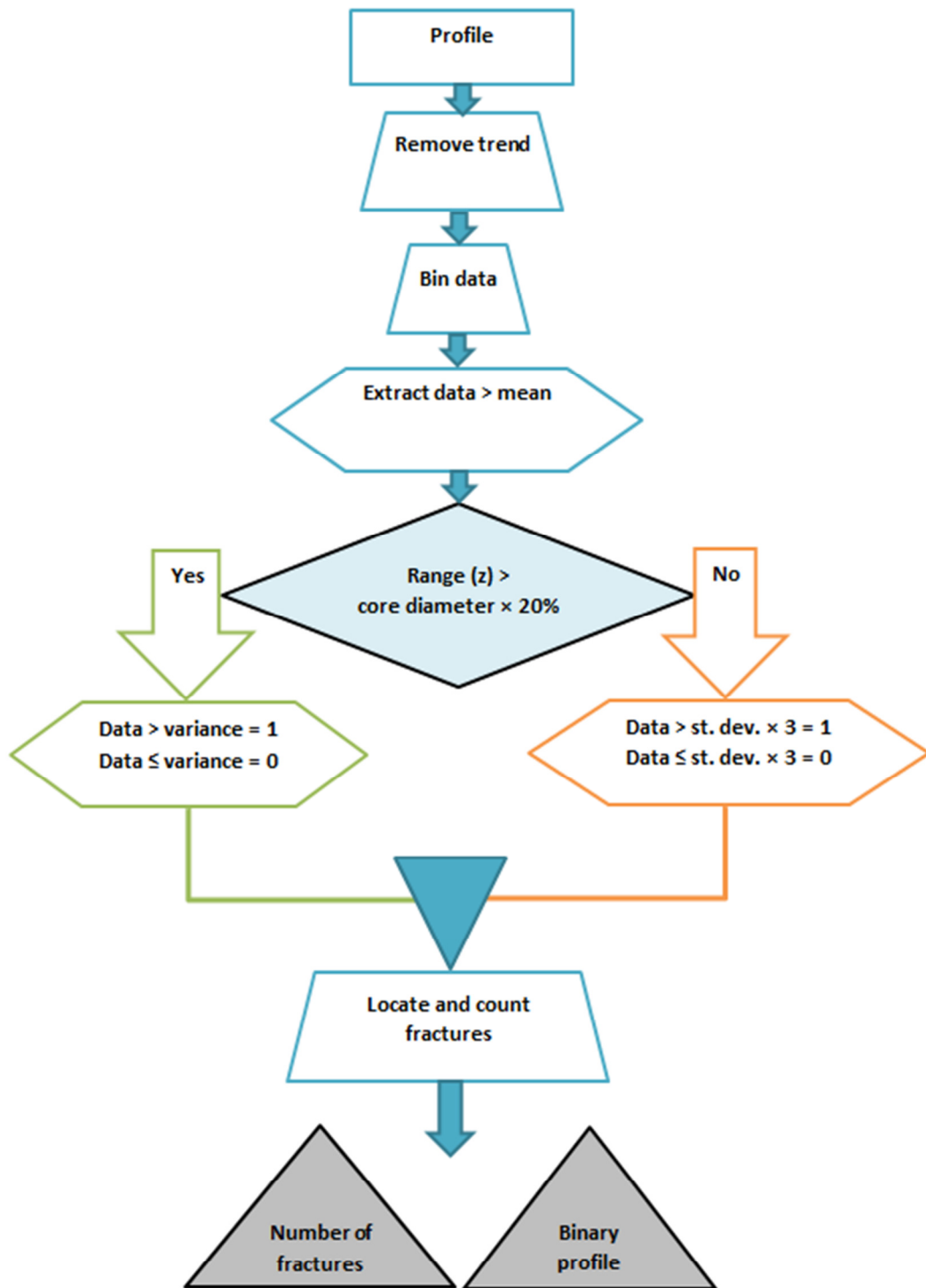


Figure 5.7: Fracture detection algorithm.

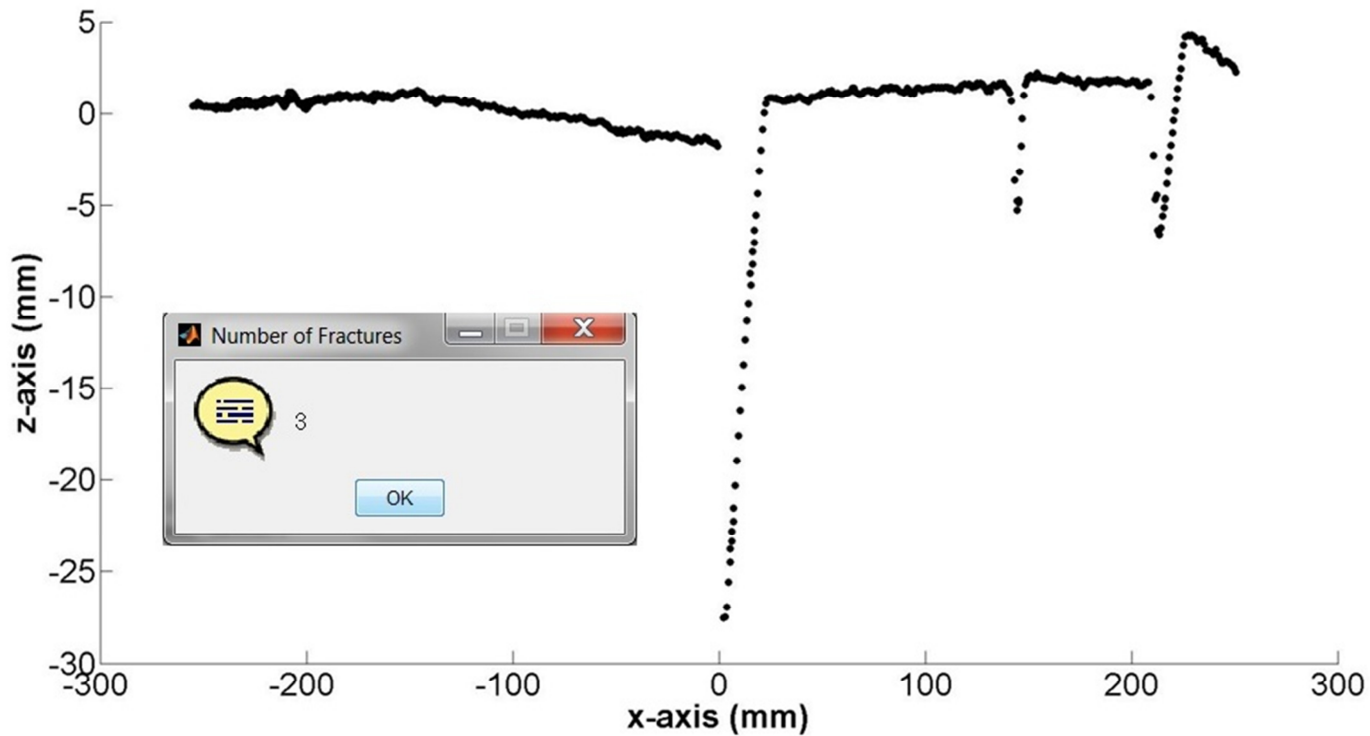


Figure 5.8: Core profile with trend removed. The pop-up window shows that the algorithm detected 3 fractures. The 3 fractures (at $x \approx -10$ mm, $x \approx 130$ mm, $x \approx 215$ mm) detected by the algorithm are visible as points extending below the zero on the z-axis. From the profile it is clear that the longer 2 core sections on the left are greater than 100 mm (10 cm) and will be included in the RQD. The shorter 2 sections on the right are less than 100 mm and will be excluded.

5.6: The Simulated RQD Algorithm

The simulated RQD algorithm is illustrated in Figure 5.9. The binary profile is the input for this algorithm. The length of the intact core segments are measured, the lengths greater than 10 cm summed, divided by the length of the core run and multiplied by 100%. The percentage is categorized to determine the qualitative RQD category. The simulated RQD percentage and qualitative RQD outputs are displayed in pop-up message boxes, shown in Figure 5.10.

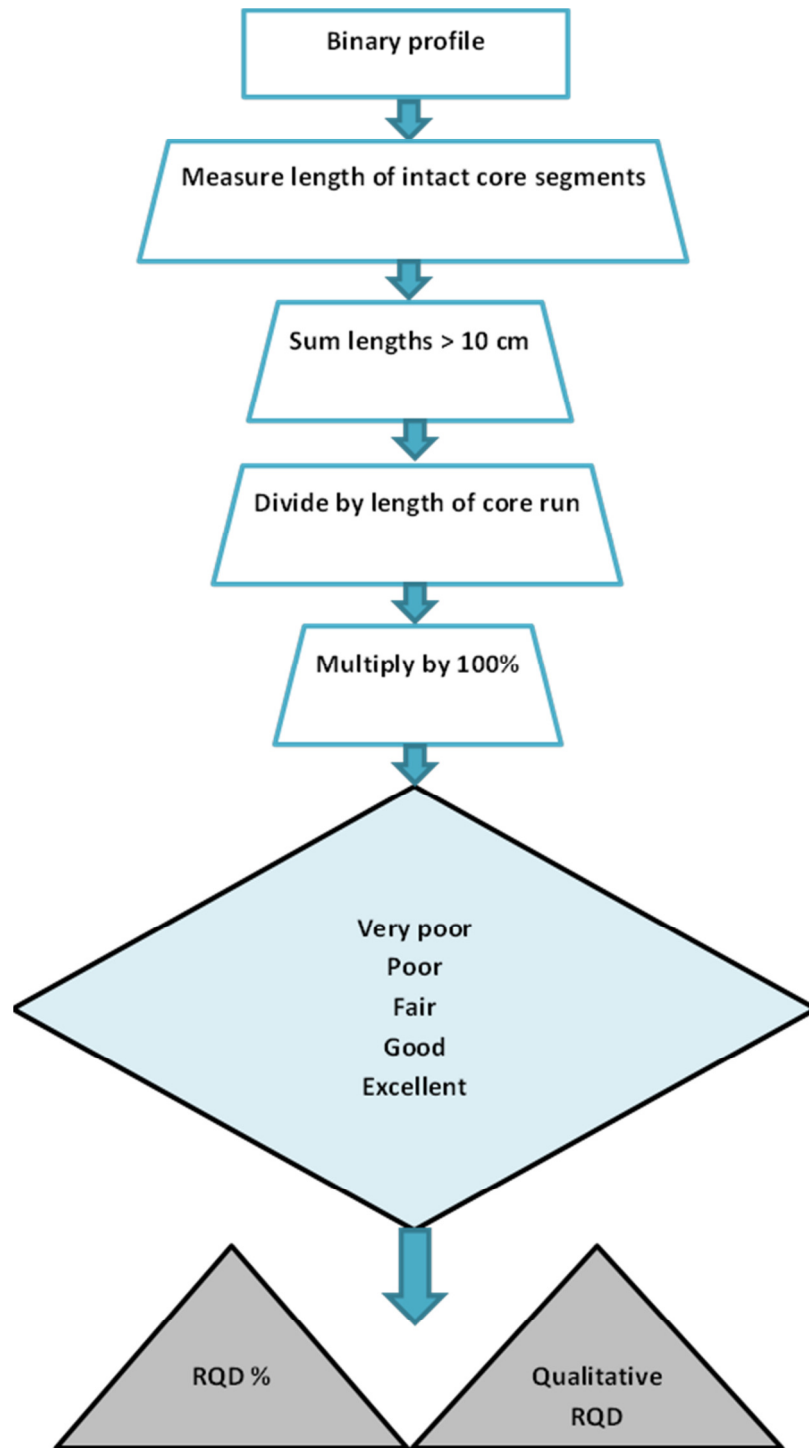


Figure 5.9: The simulated RQD algorithm.



Figure 5.10: The simulated RQD percentage and description are displayed in pop-up message boxes. In this case, the RQD is 68% which corresponds to fair quality.

5.7 Distance-Based Image Algorithm

Shown in Figure 5.11 is the distance-based image algorithm. The single core point cloud is the input for this algorithm. The length of the x and y axes are measured and multiplied by 10. These lengths define the size of the matrix. The matrix is populated with the corresponding z-values. The value of z is interpolated for empty cells. For cells with more than one z-value, the average is taken. The output is a grey-level distance-based image. The distance-based images are used for fracture characterization (Figures 5.13 and 5.14) and with the MATLAB image processing tools.

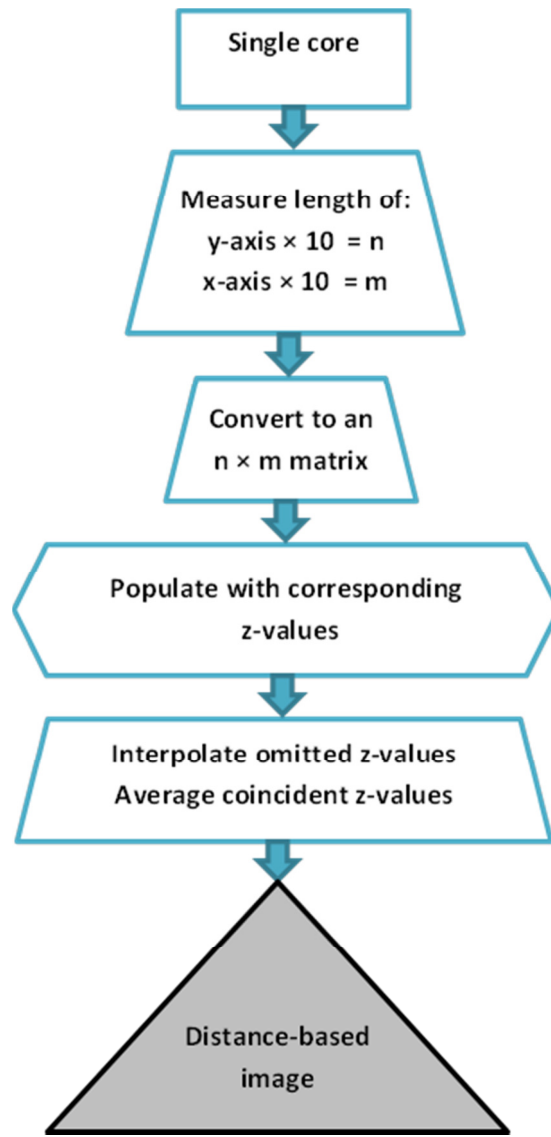


Figure 5.11: Distance-based image algorithm.

5.8 Fracture Trace Algorithm

The fracture traces algorithm is illustrated in Figure 5.12. The distance-based image output is the input for this algorithm. A profile is taken along each row. The standard deviation of each profile is calculated and used as a threshold. The fracture edge coordinates are located and extracted. The output is the xy coordinates of the fracture trace.

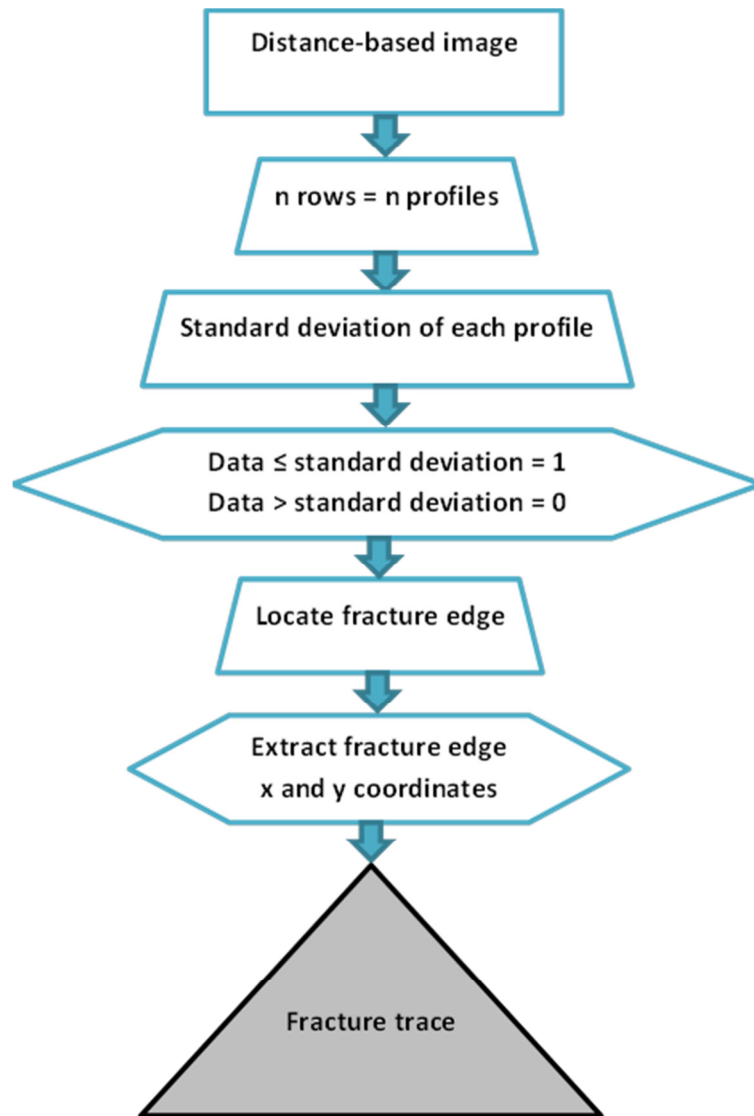


Figure 5.12: Fracture trace algorithm.

5.9 Fracture Characterization Algorithm

The fracture characterization algorithm is shown in Figure 5.13. The fracture trace output is the input for this program. The program determines whether the trace is linear or curved. If the trace is curved, the fracture is classified as natural (N.). If it is linear, the algorithm measures the angle of the trace. Once the angle is determined, the roughness of the trace is assessed by two tests. If the angle is low to moderate and the trace is smooth, the fracture is natural; if the trace rough then it is ambiguous (A.). Similarly, for high angle traces, if the trace is rough it is mechanical (M.); if it is smooth is ambiguous. The trace is further classified as ambiguous natural or ambiguous mechanical depending on the angle of the trace and whether none, one, or both of the roughness tests are satisfied. This program displays a pop-up box with a message indicating the fracture type, as illustrated in Figure 5.14.

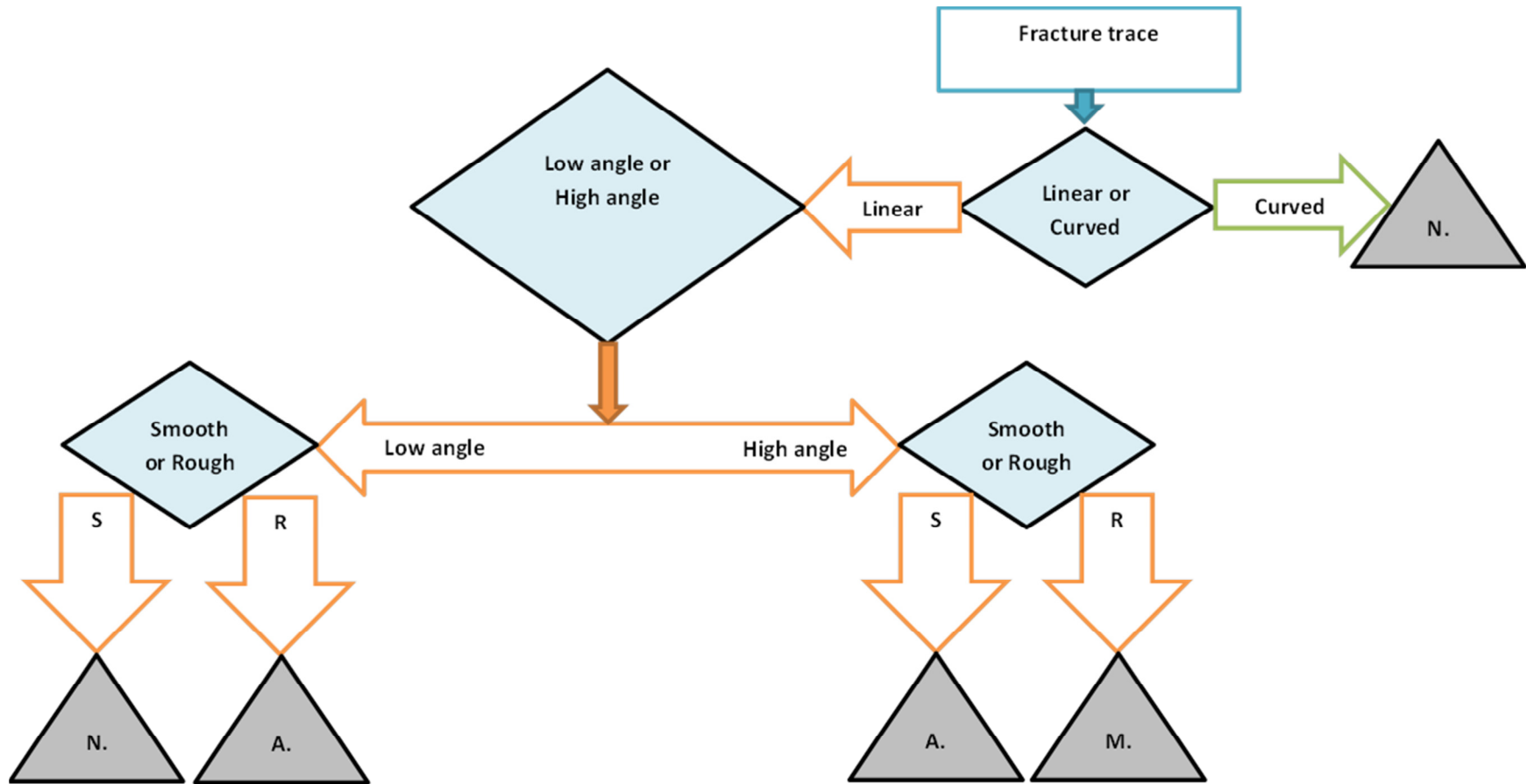


Figure 5.13: Fracture characterization algorithm.

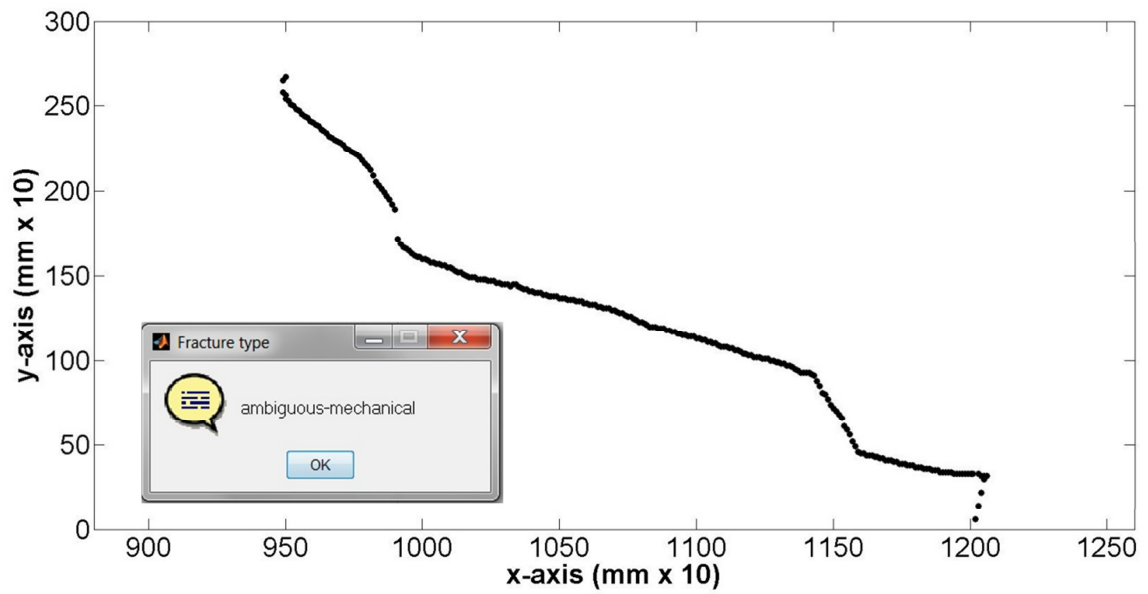


Figure 5.14: Ambiguous mechanical break. The trace is categorized as such because it has a moderate angle (a natural fracture characteristic) and is rough (a mechanical break characteristic).

6. Discussion, Recommendations for Future Work, Concluding Remarks

6.1 Overview

Various imaging procedures and algorithms were developed to investigate whether 3-D image data could be used to determine the simulated RQD. The purpose of this research was not to produce an industry-ready core logging tool. This was a proof-of-concept project in an emerging field of research – 3-D imaging of geological materials.

Each of the objectives listed in the introduction was achieved. Equally important was determining the merits and limitations of each aspect of the research project – the digitizer, the 3-D data, the fracture detection, simulated RQD and fracture characterization algorithms, the distance-based images, the 3-D core models and the level of automation that could be achieved.

6.2 The Digitizer

The advantages of the particular digitizer used include sub-millimeter accuracy, portability and many configuration options when mounted on the tripod. The image acquisition time was very reasonable at approximately 11.5 seconds. The Konica Minolta Polygon Editing Tool software was easy to use. The scan range of 0.5 to 2.5 m allowed for small and large objects to be imaged. Large objects, such as a core box, however, had to be scanned at a greater distance. Given a fixed image resolution, the greater the distance, the lower the point cloud concentration representing the surface features of the target.

The point cloud concentration was the major limiting factor of this research. For fracture detection and the RQD, each core box had to be imaged in sections. Thus, the RQD was could not be determined from a single image of the core box. The lens and digitizer configuration had to be changed to increase the point cloud concentration for fracture characterization. Natural fractures and mechanical breaks were distinguished by a separate algorithm. The result was a simulated RQD with an artificially short core run length and all fractures counted as natural. In order to adapt the algorithm to compute the true RQD:

- The field of view must be enlarged so that the entire core box can be visualized in a single image;
- A minimum point cloud concentration of 11 point/mm² is needed so the fracture characterization algorithm can be integrated into the RQD algorithm.

6.3 The 3-D Data

The advantage – and limitation – of 3-D imaging is that it is distance-based. The data are measurements of the changes in the core surface, which are represented by the z coordinate. Limitations arise when there is little change in z. For example, very tight fractures, especially ones that fit together seamlessly, essentially have no change in z. Healed fractures, though not included in the RQD, may be of interest for other purposes; these fractures would not be detected either.

For this research, it was predicted that tight fractures with a gap of 1 mm or less could not be reliably detected. This limit was due to a point cloud concentration of 1 point/mm². The prediction was correct. However, it is difficult to know whether a higher point cloud concentration would measure a wider range of z values for a tight fracture, or simply add redundant z-values. If the latter is true, then this is a significant limitation.

6.4 Fracture Detection

The final fracture detection algorithm had a success rate of 83%. The typical error was ± 1 fracture. There were an equal number of instances where fractures were missed, or erroneous fractures were detected. This result suggests that the threshold does not systematically over- or under-detect fractures.

As discussed in the previous section, tight fractures were not consistently detected. In some instances, core fragments and other debris lodged under intact core sections, and rubble in the fracture gap caused the program to detect erroneous fractures – the number of fractures detected was greater than the number observed. In other instances, the debris under the core and rubble in the fracture gap had no effect on the performance of the algorithm. Whether the algorithm was adversely affected depended on the combination of size of the debris or rubble and the value of threshold. Large core fragments and rubble were typically above the threshold, and as such, were identified as intact core.

Though removing core fragments and rubble would have yielded better results, the decision was made to leave these objects in the core box; at a mine site it is not practical to remove the debris under core segments or from fracture gaps. Any time-saving potential offered by 3-D imaging would be significantly reduced. As a result, the algorithm was tested under real-world conditions and this operational issue was identified for further study.

6.5 The Simulated RQD

The merits of the simulated RQD algorithm are that it mimics the centerline method recommended by Deere and Deere (1989) and, compared to an experienced geologist logging the core manually, the standard deviation was approximately 4.5% and the mode was - 3%. The mean, median and mode were all negative which indicates that the algorithm tends to systematically underestimate the RQD. However, differences of a few percent between the detected and observed simulated RQD would not likely have a significant impact on the value of the RMR system and Q-system as the RQD is only one of several parameters considered in these rock mass assessment schemes.

Many of the limitations were due to the image resolution and point cloud concentration – not the algorithm. For instance, the RQD is sensitive the length of the core run. The values determined for these experiments were probably artificially low because the core boxes were scanned in sections. In addition, counting all fractures as natural also artificially lowered the RQD. Ideally, the

mechanical breaks should have been fitted together and the core segments treated as intact. Thus, the RQD for the purposes of this project is a proof-of-concept parameter – the percentages have no physical meaning. The important finding is the RQD calculated by the algorithm was consistent with the observed RQD. When the technology allows for the entire core box to be scanned at a higher resolution, without changing the digitizer configuration or lens, the algorithm could be easily modified to characterize the fractures and calculate the RQD for the full length of the core run.

6.6 Fracture Characterization

The linear fracture trace characterization algorithm was perhaps the most successful of the project – the categorization was fully consistent with observations. This result was much better than expected as only the fracture trace was used. To be consistent with what is visible in a core box and real-world working conditions, the breakage surface was not imaged; this was a disadvantage because the level of weathering could not be assessed – a key parameter used to distinguish natural fractures from mechanical breaks.

Although curved traces were distinguished from linear traces with 100% reliability, they could not be further characterized. Fitting the data to a sine wave (or a sine wave to the data) yielded ambiguous results – it was not possible to determine whether the trace was smooth or rough.

6.7 Distance-Based Images

For fracture detection, the functions in MATLAB's image processing toolbox performed better on the distance-based images than the intensity-based digital photographs. For the digital photographs, rock texture was interpreted as areas of high or low elevation, or as edges or boundaries. Real changes in elevation and physical boundaries such as fractures and the edges of the core were detected on the distance-based images. Rock texture was eliminated. It is important to note that despite the clear advantage of using 3-D data with the image processing tools, if there is little or no change in the value of z, fractures may not be visible.

6.8 The 3-D Core Models

The cylindrical shape of the cores provided a significant 3-D modeling challenge. Core 1 had two high angle breakage surfaces which were very similar in appearance. In most cases, it was impossible to tell one end of the core from the other or how the core was oriented. Careful labeling of the scan angle and position during image acquisition facilitated identification. One breakage surface had a large potassium feldspar crystal that protruded slightly – this was the only distinguishing feature. Otherwise, subtle changes in the fracture trace were used to align images; this involved some subjective interpretation, which is reflected in the relatively high average standard deviation. Of the three samples, this core

approximated a cylinder the best. Thus, as predicted, it was the most difficult to model.

Cores 2 and 3 had distinct breakage surfaces which made them easier to model – at least it was almost always possible to distinguish which end of the core was which. However, core 2 was very smooth so there were few variations on the breakages surfaces to use for alignment. Core 3 was the easiest model to assemble because the breakage surfaces were rough and had a variety of distinctive features. Core 3 also had the lowest average standard deviation.

The density of the core samples was consistent with the known density range of the given rock types; though this was not conclusive as most rock density ranges have some overlap.

6.9 Level of Automation

The level of automation achieved for this project was very high compared to some of the research outlined in chapter 2. For many of those programs, the user had to select a different threshold and adjust the preprocessing steps, such as contrast enhancement, manually for each image. The algorithms developed for this project required three user interactions – program selection, file selection and core selection. Arguably, the first two interactions cannot be automated. The core selection interaction should be automated because various users may select the core in different ways – including more or less of the area around the core. These selection biases may affect the reliability of the algorithms. The

automation could be achieved by creating a permanent digitizer set-up. For example, the digitizer mounted to the ceiling, a specific area marked out on a table where the core is placed.

Unlike the actual core, which is typically discarded, the 3-D data can be archived and accessed at any point in the future.

6.10 Recommendations for Future Work

The Digitizer:

The latest version of the digitizer is the Konica Minolta RANGE 7. The image resolution has increased to 1280×1024 pixels/voxels compared to the VIVID 9i at 640×460 pixels/voxels. However, the scan range has decreased from 0.50 m – 2.50 m (VIVID 9i) to 0.45 m – 0.8 m (RANGE 7). Even at the maximum scan distance the entire core box would not fit in a single image, though the point cloud concentration would be higher. In addition, the lenses still have to be changed manually. A zoom lens would be preferable. Given that the core box would still have to be imaged in sections, it does not appear that the RANGE 7 digitizer would perform significantly better than the VIVID 9i. The ideal digitizer would have the scan range of the VIVID 9i and an image resolution sufficient to yield a point cloud concentration of approximately 11 point/mm².

The 3-D Data:

For tight fractures with no discernable change in z, the fracture trace may be visible as a dark line or curve crosscutting the core. In these cases, using intensity-based 2-D imaging in parallel may be appropriate.

Fracture Detection:

The performance of the fracture detection algorithm on sedimentary rock (the algorithm was tested on metamorphic and intrusive igneous rocks such as gneiss and gabbro) was not tested. Is there a change in z associated with bedding planes and contacts between matrix and clasts of rock such as conglomerate or breccia? Would the drilling process smooth the core surface and effectively erase these contacts? The answer to these questions may limit the potential use of 3-D imaging for fracture detection to hard rock mining, or expand its use to energy and environmental projects in sedimentary systems.

The RQD:

An important aspect of the RQD which was not taken into account is the weathering grade. It is difficult to imagine how weathering could be assessed with 3-D data. One possibility is to integrate a 3-D digitizer into the mobile core laboratory discussed in Chapter 2 (Ross et al. 2011).

The algorithm was not tested on core that is essentially all rubble, with an RQD of zero. The assumption was there would be intact lengths of core to

measure between the fractures. Based on the performance of the algorithm in fracture gaps that contain rubble, however, it is likely that the algorithm, detecting no material greater than 10 cm, would return an RQD of 0.

There is a dearth of information and parameters related to fracture characterization. In many cases, the origin of a fracture is ambiguous. Increasing the number of parameters and introducing a formal classification scheme would improve matters. However, the parameters need to be quantifiable to be incorporated into a fracture characterization algorithm. For this project, the roughness of the trace was quantified by two very simple methods with great success, which suggests that other parameters could be as well.

Fracture Characterization:

To further characterize curved fracture traces, some of the functions from MATLAB's curve fitting toolbox could be tested. The toolbox contains pre-programmed functions specifically designed for data with this type of geometry.

Distance-Based Images:

Rock texture was one of the primary limiting factors of the 2-D imaging research discussed in chapter 2. It would be interesting to see if the distance-based images improved the performance of those algorithms.

The 3-D Core Models:

Given the amount of time and expertise required to construct 3-D models, and the challenges presented by the cylindrical shape of the core, it is difficult to imagine the practical application of these techniques to solve problems in the time-limited environment of the mining sector. This line of research seems best suited to delicate materials, where non-destructive methods and a permanent visual record are desirable – soft sediment cores or ice cores, for example.

6.10 Concluding Remarks

The 3-D imaging of drill core is a relatively unexplored topic in an emerging field of research. The research presented here shows that fractures in core can be detected and characterized, and the RQD can be measured with a high level of automation using 3-D data. The performance of image processing tools is also improved when used on distance-based images generated from 3-D data. Models of core in 3-D can also be constructed successfully despite the inherent difficulty posed by their cylindrical shape. Once the limitations identified in this research project have been addressed, and further research is done, 3-D imaging has the potential to become a viable alternative to manual core logging in the future.

7. References

Barton, N., Lien, R., and Lunde, J. 1974. Engineering classification of rock masses for the design of tunnel support. *Rock Mechanics*, **6**: 189 – 236.

Bieniawski, Z.T. 1973. Engineering classification of jointed rock masses. *Transactions of the South African Institution of Civil Engineers*, **15**: 335 – 344.

Bieniawski, Z.T. 1974. Geomechanics classification of rock masses and its application in tunneling. *In Proceedings of the 3rd International Congress on Rock Mechanics*, Denver, Colorado, Vol. 2A, pp. 27 – 32.

Bieniawski, Z.T. 1976. Rock mass classification in rock engineering. *In Proceedings of the Symposium on Exploration for Rock Engineering*, Johannesburg, South Africa, Vol. 2, pp. 97 – 106.

Bieniawski, Z.T. 1979. The geomechanics classification in rock engineering applications. *In Proceedings of the 4th International Congress on Rock Mechanics*, Montreux, Switzerland, Vol. 3, pp. 41 – 48.

Bieniawski, Z.T. 1988. The rock mass rating (RMR) system in engineering practice. *In Rock Classification Systems for Engineering Purposes. Edited by L. Kirkaldie*. American Society for Testing and Materials, Philadelphia, Pennsylvania. pp. 17 – 34.

Boivin, A., Lai, P., Samson, C., Cloutis, E., Holladay, S., and Monteiro Santos, F.A. 2013. Electromagnetic induction sounding and 3D laser imaging in support of a Mars methane analogue mission. *Planetary and Space Science*, **83-83**: 27 – 33.

Canny, J. 1986. A computational approach to edge detection. *IEEE Transactions on Pattern Analysis and Machine Intelligence*. **8**(6): 679–698.

Dearman, W. R. 1976. Weathering classification in the characterization of rock: A revision. *Bulletin International Association Engineering Geologists*. **13**: 373 – 381.

Deb, D., Hariharan, S., Rao, U.M., and Chang-Ha, R. 2008. Automatic detection and analysis of discontinuity geometry of rock mass from digital images. *Computers & Geosciences*, **34**: 115 – 126.

Deere, D.U., Hendron A.J. Jr., Patton F.D., and Cording E.J. 1967. Design of surface and near surface construction in rock. *In Proceedings of the 8th U.S. Symposium in Rock Mechanics on Failure and Breakage of Rock*, New York, pp. 237 – 302.

Deere, D.U. 1968. Geologic Considerations. *In Rock Mechanics in Engineering Practice*. Edited by K. Stagg and O. Zienkiewicz. Wiley, New York, pp. 1 – 20.

Deere, D.U., and Deere, D.W. 1988. The rock quality designation (RQD) index in practice. *In Rock Classification Systems for Engineering Purposes*. Edited by L.

Kirkaldie, American Society for Testing and Materials Special Publication 984, Philadelphia, Pennsylvania, pp. 91 – 101.

Deere, D.U., and Deere, D.W. 1989. Rock quality designation (RQD) after 20 years. US Army Corps of Engineers Contract Report. Waterways Experimental Station, Vicksburg, MS. Report No. GL-89-1.

¹Dixon, L., Samson, C., and McKinnon, S.D. 2011a. Using 3-D laser imaging to map fractures in core samples. *In* Proceedings of the Annual Scientific Meeting of the Canadian Geophysical Union, Banff, Canada.

¹Dixon, L., Samson, C., and McKinnon, S.D. 2011b. 3-D Laser imaging of core for fracture mapping. *In* Proceedings of the Geological Association of Canada – Mineralogical Association of Canada, Annual Meeting, Ottawa, Ontario, Vol.34, pp. A54.

Fekete, S., and Diederichs, M. 2013. Integration of three-dimensional laser scanning with discontinuum modelling for stability analysis of tunnels in blocky rock masses. *International Journal of Rock Mechanics and Mining Sciences*. **57**: 11–23.

Ferrero, A.M., Forlani, G., Roncella, R., and Voyat, H.I. 2009. Advanced geostructural survey methods applied to rock mass characterization. *Rock Mechanics and Rock Engineering*. **42**: 631 – 665.

Ferrero, A.M., and Umili, G. 2011. Comparison of methods for estimating fracture size and intensity applied to Aiguille Marbrée (Mont Blanc). *International Journal of Rock Mechanics & Mining Sciences*. **48**: 1262 – 1270.

Gigli, G., and Casagli, N. 2011. Semi-automatic extraction of rock mass structural data from high resolution LIDAR point clouds. *International Journal of Rock Mechanics & Mining Sciences*. **48**: 187 – 198.

Gonzalez, R.C., and Woods, R.E. 2008. Point, line and edge detection. *In Digital Image Processing*. Edited by M. McDonald. Prentice Hall, Upper Saddle River, New Jersey. pp. 692-737.

Hadjigeorgiou, J., Lemy, F., Côté, P., and Maldague, X. 2003. An evaluation of image analysis algorithms for constructing discontinuity trace maps. *Rock Mechanics and Rock Engineering*. **36**(2): 163 – 179.

Hadjigeorgiou, J. 2012. Where do the data come from? *Mining Technology*. **121**(4): 236 – 247.

Hardy A. J., Ryan, T.M., and Kemeny, J.M. 1997. Block size distribution of *in situ* rock masses using digital image processing of drill core. *International Journal of Rock Mechanics and Mining Science*. **34**(2): 303 – 307.

Heuze, F.E. 1971. Sources of errors in rock mechanics field measurements and related solutions. *International Journal of Rock Mechanics and Mining Sciences*. **8**: 297 – 310.

Hu, J., Sakoda, B., and Pavlidis, T. 1992. Interactive road finding for aerial images. In *Proceedings of the IEEE Workshop on Applications of Computer Vision*, Palm Springs, California, pp. 56 – 63.

Jakubec, J., and Esterhuizen, G.S. 2007. Use of the mining rock mass rating (MRMR) classification: Industry experience. *In Proceedings of the International Workshop on Rock Mass Classification in Underground Mining. Edited by C. Mark, R. Pakalnis, and R.J. Tuchman*. NIOSH Information Circular 9498, pp. 73 – 78.

Konica Minolta. Non-contact 3D digitizer VIVID 9i/VI-9i instruction manual (hardware).

Lauffer, H. 1958. Gebirgsklassifizierung für den Stollenbau. *Geol Bauwesen*. **24**(1): 46 – 51.

Lemy, F., Hadjigeorgiou, J., Côté, P., and Maldague, X. 2001. Image analysis of drill core. *Transactions of the Institution of Mining and Metallurgy: Section A – Mining Technology*. **110**: A172 – A177.

Lemy, F., and Hadjigeorgiou, J. 2003. Discontinuity trace map construction using photographs of rock exposures. *International Journal of Rock Mechanics & Mining Sciences*. **40**: 903 – 917.

Longoni, L., Arosio, D., Scaioni, M., Papini, M., Zanzi, L., Roncella, R., and Brambilla, D. 2012. Surface and subsurface non-invasive investigations to improve the characterization of a fractured rock mass. *Journal of Geophysics and Engineering*. **9**: 461 – 472.

Mah, J., Samson, C., and McKinnon, S.D. 2011. 3D laser imaging for joint orientation analysis. *International Journal of Rock Mechanics & Mining Sciences*. **48**: 932 – 941.

Mah, J., Samson, C., McKinnon, S.D., and Thibodeau, D. 2013. 3D laser imaging for surface roughness analysis. *International Journal of Rock Mechanics & Mining Sciences*. **58**: 111 – 117.

MATLAB and MATLAB Image Processing Toolbox. 2012. Mathworks Inc.

McCausland, P., Samson, C., and McLeod, T. 2011. Meteorite bulk density via visible light 3-D laser imaging. *Meteoritics and Planetary Science*. **46**(8): 1097 – 1109.

Milne, D., Hadjigeorgiou, J., and Pakalnis, R. 1998. Rock mass characterization for underground hard rock mines. *Tunnelling and Underground Space Technology*. **13**(4): 383 – 391.

²Olson, L., Samson, C., and McKinnon, S.D. 2013a. Fracture detection with profiles and range-based images from 3-D laser digitizer data. In *Proceedings of the 1st Joint Scientific Congress CMOS-CGU-CWRA*, Saskatoon, Saskatchewan.

²Olson, L. Samson, C., and McKinnon, S.D. 2013b. The 2-D and 3-D imaging of core for fracture mapping. In *Proceedings of the 46th American Rock Mechanics Association Symposium*, San Francisco, CA, 23-26 June.

Pantelidis, L. 2009. Rock slope stability assessment through rock mass classification systems. *International Journal of Rock Mechanics & Mining Sciences*. **46**: 315 – 325.

PolyWorks V11 3-D visualization software. 2011. InnovMetric Software Inc.

Reid, T.R., and Harrison, J.P. 1997. Automated tracing of rock mass discontinuities from digital images. *International Journal of Rock Mechanics & Mining Sciences*. **34** (3–4): 256.e1 – 256.e19.

Reid, T.R., and Harrison J.P. 2000. A semi-automated methodology for discontinuity trace detection in digital images of rock mass exposures. *International Journal of Rock Mechanics & Mining Sciences*. **37**: 1073-1089.

Reynolds, J.M. 1997. *An Introduction to Applied and Environmental Geophysics*. John Wiley & Sons Inc., Hoboken, N.J.

Ritter, W. 1879. *Die Statik der Tunnelgewölbe*. J. Springer, Berlin, Germany.

Ross, P.-S., Bourke, A., Fresia, B. 2011. A multi-sensor logger for rock cores. *In Proceedings of the Geological Association of Canada – Mineralogical Association of Canada, Annual Meeting, Ottawa, Ontario, Vol.34*, pp. A188.

Santi, P. M. 2006. Field methods for characterizing weak rock for engineering. *Environmental & Engineering Geoscience*. **XII**(1): 1 –11.

Steger, C. 1998. An unbiased detector of curvilinear structures. *IEEE Transactions on Pattern Analysis and Machine Intelligence*. **20**(2): 113 – 125.

Terzaghi, K. 1946. Rock defects and loads on tunnel supports. *In Rock tunneling with steel supports, Vol. 1*. Commercial Shearing and Stamping Company, Youngstown, Ohio. pp. 17 – 99.

Smith, D.L., Samson, C., Herd, R., Christie, I., Sink, J.-E., Deslauriers, A., and Ernst, R. 2006. Measuring the bulk density of meteorites non-destructively using 3D laser imaging. *Journal of Geophysical Research*. **111**: E10002.

Sturzenegger, M., and Stead, D. 2009. Close-range terrestrial digital photogrammetry and terrestrial laser scanning for discontinuity characterization on rock cuts. *Engineering Geology*. **106**: 163 – 182.

Umili, G., Ferrero, A., Einstein, H.H. 2013. A new method for automatic discontinuity traces sampling on rock mass 3D model. *Computers & Geosciences*. **51**: 182 – 192.

¹Name changed to Olson, L.

²Formerly named Dixon, L.

Appendix I: 3-D Core Plot MATLAB Code

```
% Program: 3D Core Plot V.5 (final version)
% Description: CB configuration. Plots image for core single selection
% Author: Laura Olson
% Date: 2013/02/28

% Run first
clear
% tic/toc records the processing time
tic
% Prompts user to select file
[FileName_Data,PathName,FilterIndex] =
uigetfile({'*.asc;*.txt';'*.*'}, 'Select Scan Input File');
    %input_scan_data = dlmread(FileName_Data, '', 0, 0);
    S = [PathName FileName_Data];
    % Import data from the desired file
    newData1 = importdata(S);
    % Create new variables in the base workspace from those fields
    vars = fieldnames(newData1);
    for i = 1:length(vars)
        assignin('base', vars{i}, newData1.(vars{i}));
    end
    input_scan_size = size(data, 1);
% Extracts xyz columns from file
x=data(:,1);
y=data(:,2);
z=data(:,3);
miny=min(y);
mid=median(x);
%plots 10% of data for faster processing
figure
scatter3(x(1:10:end),y(1:10:end),z(1:10:end),10,z(1:10:end)), view(2);
colormap(jet);
toc
pause on
fprintf('\n')
fprintf('Program paused for plot viewing. Press any key to resume.')
fprintf('\n')
pause off
%Prompt for instructions
Message{1} = 'Select the four corners of the core.';
Message{2} = 'Left click each corner with mouse.';
Message{3} = 'CLICK ORDER IS IMPORTANT: top right, bottom right, bottom
left, top left';
Title = 'Box Selection Instructions';
q = msgbox(Message,Title,'help','modal');
uiwait(q)
%Record click positions
[x_box,y_box] = ginput(4);
box_coords = [x_box y_box];
save('input_data.mat', 'data');
save('box_coords.mat', 'box_coords');
```

Appendix II: Single Core Plot MATLAB code

```
% Program: Single Core Plot V.4 (final version)
% Description: CB configuration. Plots single core image
% Author: Laura Olson
% Date: 2013/02/28

% Run second
clear
% tic/toc records the processing time
tic
load input_data.mat
input_scan_data = data;
input_scan_size = size(input_scan_data, 1);
%loads selection coordinates
load box_coords.mat
input_coord_data = box_coords;
% Need to reference the points
x_NE = input_coord_data (1,1);
y_NE = input_coord_data (1,2);
x_SE = input_coord_data (2,1);
y_SE = input_coord_data (2,2);
x_SW = input_coord_data (3,1);
y_SW = input_coord_data (3,2);
x_NW = input_coord_data (4,1);
y_NW = input_coord_data (4,2);
% Finds image data within selection coordinates
x=data(:,1);
y=data(:,2);
z=data(:,3);
INDX = find(x>x_NW & x<x_NE & y>y_SW & y<y_NW);
xcore_data = x(INDX);
ycore_data = y(INDX);
zcore_data = z(INDX);
core_data = [xcore_data ycore_data zcore_data];
toc
% Plots xyz on a 3D smooth surface
miny=min(ycore_data);
mid=median(xcore_data);
figure
tri=delaunay(xcore_data,ycore_data);
h=trisurf(tri,xcore_data,ycore_data,zcore_data);
axis vis3d
l = light('Position',[-50 -15 29]);
set(gca,'CameraPosition',[mid miny 0],'DataAspectRatio',[1 1 1])
lighting phong
shading interp
colorbar EastOutside
xlabel('x-axis (mm)')
ylabel('y-axis (mm)')
zlabel('z-axis (mm)')
save('core_box.mat', 'core_data');
```

Appendix III: Core Profile Line MATLAB Code

```
% Program: Core Profile Line V.5 (final version)
% Description: CB configuration. Extracts and displays core profile
% Author: Laura Olson
% Date: 2013/01/18

% Run third
% tic/toc records the processing time
tic
input_scan_data = core_data;
input_scan_size = size(core_data,1);
%Profile line half thickness(mm)
lineThickness = 0.5;
%Finds center profile line
x=core_data(:,1);
y=core_data(:,2);
z=core_data(:,3);
minx=min(x);
maxx=max(x);
midy=median(y);
input_line_data = [minx midy 0
                  maxx midy 0];
% Need to reference the points (width of center line)
x_E = (input_line_data (2,1));
y_NE = (input_line_data (2,2)) + lineThickness;
y_SE = (input_line_data (2,2)) - lineThickness;
x_W = (input_line_data (1,1));
y_SW = (input_line_data (1,2)) - lineThickness;
y_NW = (input_line_data (1,2)) + lineThickness;
% Finds image data within profile coordinates
INDX = find(x>x_NW & x<x_NE & y>y_SW & y<y_NW);
xline_data = x(INDX);
yline_data = y(INDX);
zline_data = z(INDX);
toc
% Core profile plot
figure
plot(xline_data,zline_data, '.');
xlabel('x-axis (mm)')
ylabel('z-axis (mm)')
title('Core Profile')
```

Appendix IV: Fracture Detector MATLAB Code

```
% Program: Fracture Detector v.11 (final version)
% Description: CB configuration. Detects and counts fractures
% Author: Laura Olson
% Date: 2013/06/23

% Run fourth
% tic/toc records the processing time
tic
x = xline_data;
y = yline_data;
z = zline_data;
% Enter core diameter in mm
coreDiameter = 34.6;
% Sorts z with respect to x
xz = [x(:),z(:)];
xz_sort = sortrows(xz,1);
x_sort = xz_sort(:,1);
z_sort = xz_sort(:,2);
Dtrnd_z = detrend(z_sort);
% Bins the data
binMax = max(x_sort);
binMin = min(x_sort);
Nbins = round(length(x_sort)*0.1);
binLimits = linspace(binMin, binMax, Nbins);
[~, binSort] = histc(x_sort, binLimits);
binSort = ceil(linspace(min(binSort),max(binSort),length(binSort)));
binRangezrow = zeros(1,length(binLimits));
for i = 1:Nbins
    IDbinEntries=(binSort==i);
    zbinEntries=Dtrnd_z(IDbinEntries);
    binRangezrow(i)=abs(max(zbinEntries)-min(zbinEntries));
end
binLimits = linspace(binMin, binMax, Nbins);
[~, binSort] = histc(x_sort, binLimits);
binSort = ceil(linspace(min(binSort),max(binSort),length(binSort)));
binMedxrow = zeros(1,length(binLimits));
for i = 1:Nbins
    IDbinEntries = (binSort==i);
    xbinEntries = x_sort(IDbinEntries);
    binMedxrow(i) = median(xbinEntries);
end
binRangez = binRangezrow';
binMedx = binMedxrow';
%Calculates the difference between the core and the mean(z_sort)
mean_line = ones(length(binRangezrow),1).*mean(binRangezrow);
BFM1 = (binRangezrow - mean_line)';
BFM = (BFM1>mean(BFM1));
%Normalizes the difference to a number between 0 and 1
BFMnrm =abs(BFM.*BFM1)./max(BFM1);
BFMnormalized = BFMnrm;
```

```

% Threshold selection
BFM_threshold = coreDiameter;
BFM_threshold1 = std(BFMnormalized)*3;
BFM_threshold2 = var(BFMnormalized);
if abs(max(z)-min(z))> coreDiameter*0.2;
    BFM_threshold = BFM_threshold2;
else BFM_threshold = BFM_threshold1;
end
% Finds the fracture edges
BFM = BFMnormalized>BFM_threshold;
frac_edgeV = padarray(BFM',1,0);
frac_edgeVDFE = diff(frac_edgeV);
startIndexONES = find(frac_edgeVDFE==1);
endIndexONES = find(frac_edgeVDFE==-1);
countOnes = (endIndexONES - startIndexONES);
fractures = find(countOnes);
numFractures = length(fractures);
toc
% Displays number of fractures
Message = num2str(numFractures);
Title = 'Number of Fractures';
q = msgbox(Message,Title,'help');
% Fracture detection plot with threshold
threshold_line = ones(length(binMedxrow),1).*BFM_threshold;
figure
bar(binMedxrow,(BFMnormalized>BFM_threshold).*BFMnormalized);
hold on;
plot(binMedxrow,threshold_line);
hold off;
toc

```

Appendix V: RQD MATLAB Code

```
% Program: RQD V.3 (final version)
% Description: CB configuration. Calculates the RQD
% Author: Laura Olson
% Date: 2013/02/19

% Run fifth
tic % tic/toc records the processing time
% Finds and measures intact core lengths
B = BFM;
B(1)=1;
intact_edgeV = padarray(B',1,1, 'post');
intact_edgeVDFF = diff(intact_edgeV);
startIndexZRS = find(intact_edgeVDFF < 0);
endIndexZRS = find(intact_edgeVDFF > 0)-1;
countZRS = (endIndexZRS-startIndexZRS)+1;
startx = binMedx(startIndexZRS);
endx = binMedx(endIndexZRS);
xLgth = abs(endx - startx)+1;
xLgth_threshold = 100;
RQDxindex = abs(xLgth)>=xLgth_threshold;
% RQD calculation
RQDxLgth = RQDxindex.*xLgth;
NLgths = (sum(RQDxLgth))*100;
coreRN = abs(max(x) - min(x));
RQD_percent = floor(NLgths/coreRN);
RQD=RQD_percent;
% Qualitative RQD
if RQD<25;
    RQD_description = 'very poor';
end
if RQD>=25;
    RQD_description = 'poor';
end
if RQD>=50;
    RQD_description = 'fair';
end
if RQD>=75;
    RQD_description = 'good';
end
if RQD>=90;
    RQD_description = 'excellent';
end
% RQD percentage and description messages
Message1 = num2str(RQD_percent);
Title = 'RQD %';
q1 = msgbox(Message1,Title,'help');
Message2 = num2str(RQD_description);
Title = 'RQD description';
q2 = msgbox(Message2,Title,'help');
toc
```

Appendix VI: Distance-Based Image MATAB Code

```
% Program: Distance-based image V.2 (final version)
% Description: CB or TT configuration. Converts point cloud data to
grey-level data. For use with the MATLAB image processing toolbox or
fracture characterization
% Author: Laura Olson
% Date: 2012/11/15

% Run first
% tic/toc records the processing time
tic
%Extracts xyz column vectors from point cloud file
x = core_data(:,1);
y = core_data(:,2);
z = core_data(:,3);
% Finds the size of the image area in mm
range_x = round(max(x) - min(x))*10;
range_y = round(max(y) - min(y))*10;
% Creates a uniformly spaced x and y points
xlin = linspace(min(x), max(x),range_x);
ylin = linspace(min(y), max(y),range_y);
[X,Y] = meshgrid(xlin,ylin);
% Interpolates values at uniformly spaced points
f = TriScatteredInterp(x,y,z, 'natural');
Z = f(X,Y);
%Converts the matrix Z to a distance-based grey-level image
I = mat2gray(Z);
%Displays grey-level image
figure
imshow(I);
toc
```

Appendix VII: Fracture Trace MATLAB Code

```
% Program: Fracture trace V.7 (final version)
% Description: TT configuration. Extracts the fracture trace along
multiple parallel profiles
% Author: Laura Olson
% Date: 2013/04/01

% Run second
% tic/toc records the processing time
tic
% Removes the edges of the core
[NUMrows,NUMcolumns] = size(I);
startROWy = 1+floor(NUMrows/10);
endROWy = NUMrows-floor(NUMrows/10);
yCOORDS = (startROWy:1:endROWy);
medy = median(NUMrows);
startROWx = 2;
endROWx = NUMcolumns-1;
xCOORDS = (startROWx:1:endROWx);
% Determines the number of profiles
numPROFILES = length(yCOORDS);
lgthPROFILES = length(xCOORDS);
x_profiles = repmat(xCOORDS,numPROFILES,1);
y_profiles = repmat(yCOORDS,lgthPROFILES,1);
z_profiles = I(yCOORDS,startROWx:endROWx);
numPROFILES = 1+numPROFILES;
medVECTOR = ones(1,numPROFILES).*medy;
% Profile data
x = x_profiles';
y = y_profiles;
z = z_profiles';
% Converts edges from white to black
z2=z;
z2(z2==1)=0;
figure
plot3(x,y,z2);
% Creates threshold matrix
STDrow = std(z2,[],1)';
STDrow_matrix = repmat(STDrow,1,size(z,1))';
z2(z2<=STDrow_matrix)=1;
z2(z2~=1)=0;
% Detects fracture trace
frac_edge = padarray(z2,1,0);
frac_edgeVDFF = diff(frac_edge,1,2);
frac_edgeVDFF = frac_edgeVDFF';
[Sionesy, Sionesx] = find(frac_edgeVDFF~=0);
numFRAC = round(length(Sionesx)/numPROFILES);
fracturesy = Sionesy(Sionesy~=1);
fracturesINDX = find(fracturesy);
fracturesx = Sionesx(fracturesINDX);
% Plots fracture trace
```

```
figure
scatter(fracturesx,fracturesy);
toc
```

Appendix VIII: Fracture Characterization MATLAB Code

```
% Program: Fracture characterization V.14 (final version)
% Description: TT configuration. Distinguishes natural fractures from
mechanical breaks
% Author: Laura Olson
% Date: 2013/04/16

% Run third
% tic/toc records the processing time
tic
% Distinguishes curved traces from linear traces
MEDIANx=fracturesx(round(mean(find(fracturesy==median(fracturesy)))));
INITIALx=fracturesx(1);
FINALx=fracturesx(end);
% Curved traces = 0
if MEDIANx > INITIALx && FINALx;
    fracture_shape=0;
elseif MEDIANx < INITIALx && FINALx;
    fracture_shape=0;
end
% Linear traces = 1
if MEDIANx > INITIALx && MEDIANx < FINALx;
    fracture_shape=1;
end
% Best fit line
p = polyfit(fracturesx,fracturesy,1);
r = polyval(p,fracturesx);
% Best fit line plot
figure
plot(fracturesx,fracturesy,'o');
hold on;
plot(fracturesx,r,'-');
hold off
% Best fit line residuals
residuals = r-fracturesy;
std_residuals = std(residuals)*2;
residuals = abs(residuals);
% Plot of residuals
figure
stem(fracturesx, residuals);
hold on;
figure
scatter(fracturesx,fracturesy);
hold on;
plot(fracturesx,fracturesy);
hold off;
plot(fracturesx, ones(length(fracturesx))*std_residuals);
hold off
% Percentage of residual greater than 2 standard deviations
A = mean(residuals);
```

```

AA=residuals(find(residuals>=std_residuals));
meanAA=mean(AA);
stdAA=std(AA);
AAA=(length(AA)/length(fracturesx))*100;
frac1=AAA;
% If more than 34.1% of the residuals are greater than 2 standard
% deviations, then fracture trace is mechanical
if AAA>34.1;
    frac1 = 0; % 0 = mechanical
end
% If less than 34.1% of the residuals are greater than 2 standard
% deviations, then fracture trace is natural
if AAA<=34.1;
    frac1 = 1; % 1 = natural
end
% Finds the angle of the trace
dx1 = diff(flipud(fracturesx));
dy1 = diff(flipud(fracturesy));
k1 = length(dx1);
dx11 = fracturesx(1)-fracturesx(end);
dy11 = fracturesy(1)-fracturesy(end);
main_angle1 = atan2(dy11,dx11);
main_angle1d = atan2d(dy11,dx11);
% Finds the angle of the trace points
for i= 1:k1
    angle1(i,:) = atan2(dy1(i,:),dx1(i,:));
    angle1d(i,:) = atan2d(dy1(i,:),dx1(i,:));
end
% If the trace angle is high = mechanical
% If the trace angle is low to moderate = natural
MA=mode(abs(angle1d));
if MA >=0 && MA <75 || MA <=180 && MA > 105;
    angle = 1; %natural
else angle = 0; %mechanical
end
% Histogram plot of angles (rose diagram)
figure
rose(angle1);
% Percent of bin entries inside the largest bin
H = hist(angle1);
Hpercent = max(H)/sum(H)*100;
% If less than 68.2 percent of angles are inside the largest bin =
% mechanical
frac2=Hpercent;
if Hpercent<=68.2;
    frac2 = 0;
end
% If more than 68.2 percent of angles are inside the largest bin =
% natural
if Hpercent >68.2;
    frac2 = 1;
end
% Sum of fracture characteristics

```

```

NorM = sum(vertcat(angle,frac1,frac2));
% Fracture characterization
Fracture_type = 100;
if NorM == 3;
    Fracture_type = 'natural';
end

if NorM ==0;
    Fracture_type = 'mechanical';
end

if NorM == 2;
    Fracture_type = 'ambiguous-natural';
end
    if NorM == 1;
        Fracture_type = 'ambiguous-mechanical';
    end
if fracture_shape == 0;
    Fracture_type = 'curved natural';
end
Message1 = num2str(Fracture_type);
Title = 'Fracture type';
q = msgbox(Message1,Title,'help');
toc

```